UNIVERSITY OF OTTAWA

DOCTORAL THESIS

Photoelectron spectroscopy using a synthetically chiral laser pulse

Author:
Zack DUBE

Supervisor:
Dr. André STAUDTE

A thesis submitted in fulfillment of the requirements
for the degree of Doctor of Philosophy

in the

Joint Attosecond Lab
Department of Physics

Declaration of Authorship

I, Zack DUBE, declare that this thesis titled, "Photoelectron spectroscopy using a synthetically chiral laser pulse" and the work presented in it are my own. I confirm that:

- This work was done wholly or mainly while in candidature for a research degree at this University.
- Where any part of this thesis has previously been submitted for a degree or any other qualification at this University or any other institution, this has been clearly stated.
- Where I have consulted the published work of others, this is always clearly attributed.
- Where I have quoted from the work of others, the source is always given. With the exception of such quotations, this thesis is entirely my own work.
- I have acknowledged all main sources of help.
- Where the thesis is based on work done by myself jointly with others, I have made clear exactly what was done by others and what I have contributed myself.

Signed:

Date:

List of Publications

Unpublished

- Y. Mi, E. Wang, Z. Dube, T. Wang, A. Y. Naumov, D. M. Villeneuve, P. B. Corkum, and A. Staudte, "Observation of a new pathway of H_3^+ formation" (in review)
- Z. Dube, G. P. Katsoulis, T. Wang, Y. Mi, A. Y. Naumov, D. M. Villeneuve, P. B. Corkum. A. Emmanouilidou, and A. Staudte, "Photoelectron scpectroscopy with synthetically chiral laser pulses" (in preparation)
- T. Wang, Z. Dube, N. Haram, F. Mousavi, Y. Mi, A. Y. Naumov, D. M. Villeneuve, P. B. Corkum, and A. Staudte, "Light-induced dissociation dynamics of Br_2" (in preparation)

Published

- M. Kübel, Z. Dube, A. Y. Naumov, M. Spanner, G. G. Paulus, M. F. Kling, D.M. Villeneuve, P. B. Corkum, and A. Staudte, "Streak camera for strong-field ionization", Physical Review Letter, 119 (2017)
- M. Kübel, Z. Dube, A. Y. Naumov, D.M. Villeneuve, P. B. Corkum, and A. Staudte, "Spatiotemporal imaging of valence electron motion", Nature Communications, 10 (2019)
- M. Kübel, G. P. Katsoulis, Z. Dube, A. Y. Naumov, D.M. Villeneuve, P. B. Corkum, A. Staudte, and A. Emmanouilidou "Streaking strong-field double ionization", Physical Review A, 100 (2019)
- M. Kübel, M. Spanner, Z. Dube, A. Y. Naumov, S. Chelkowski, A. D. Bandrauk, M. J. Vrakking, P. B. Corkum, D.M. Villeneuve, and A. Staudte, "Probing multiphoton light-induced molecular potentials", Nature Communications, 11 (2020)
- A. Korobenko, K. Johnston, M. Kubullek, L. Arissian, Z. Dube, T. Wang, M. Kübel, A. Y. Naumov, D. M. Villeneuve, M. F. Kling, P. B. Corkum, A. Staudte, and B. Bergues, "Femtosecond streaking in ambient air", Optica 7, 1372 (2020)

- Y. Mi, P. Peng, N. Camus, X. Sun, P. Fross, D. Martinez, Z. Dube, P. B. Corkum, D. M. Villeneuve, A. Staudte, R. Moshammer, and T. Pfeifer, "Clocking enhanced ionization of hydrogen molecules with rotational wave packets, Physical Review Letters, 125 (2020)
- T. Wang, Z. Dube, Y. Mi, G. Vampa, D. M. Villeneuve, P. B. Corkum, X. Liu, and A. Staudte, "Disentangling interferences in the photoelectron momentum distribution from strong-field ionization", Physical Review A, 106 (2022)
- G. P. Katsoulis, Z. Dube, P. B. Corkum, A. Staudte, and A. Emmanouilidou, "Momentum scalar triple product as a measure of chirality in electron ionization dynamics of strongly-driven atoms", Physical Review A, 106 (2022)

UNIVERSITY OF OTTAWA

Abstract

Faculty of Science
Department of Physics

Doctor of Philosophy

Photoelectron spectroscopy using a synthetically chiral laser pulse

by Zack DUBE

Chiral molecules are composed of the same constituent atoms, but are inherently different due to being mirror images of each other. The physical properties of such molecules are nearly identical, but the biochemical interactions can differ wildly, which has extreme implications in the pharmaceutical industry. It is for this reason that it is important to be able to characterize and study individual enantiomers, and develop physical methods to do so.

Optical techniques have evolved over the past two decades of scientific work which have been shown to be able to distinguish one enantiomer from another. These techniques tend to involve the use of circularly polarized light to induce a forward/backward asymmetry along the axis of light's propagation. The resulting sensitivity difference between enantiomers is typically on the order of a few percent.

Recently, a novel optical pulse scheme has been developed whose electric field is fully three-dimensional and inherently chiral. This field was computationally used to demonstrate that the signal difference between enantiomers can reach upwards of 100% sensitivity through the generation of high harmonics.

Presented in this thesis are the results of an experimental measurement performed using just such a novel pulse scheme. A cold target recoil ion momentum spectroscopy machine is used to detect the photoelectron spectra from the ionization of each enantiomer of propylene oxide. A comprehensive discussion on the practical realization of the novel pulse scheme is presented, and the circular dichroism due to the novel field is shown. Also discussed are fragmentation of propylene oxide, three dimensional chiral signals found in the data, and a new measure to define the magnitude of chirality in a photoelectron distribution. Finally, measurements pertaining to the ionic yield of each enantiomer under varying handedness of light are shown. These results are the first experimental realization of optical measurements using synthetically designed chirality.

Acknowledgements

The journey to submitting this thesis has been long and full of perils. I would like to take this opportunity to offer my thanks and gratitude to everyone who has helped me overcome the road.

To the COLTRIMS team over the years, who have participated in the oral tradition in preserving and passing on experimental knowledge. Matthias Kübel, Xiaoyan Ding, Yonghao Mi, Tian Wang, Nida Haram and Fatemeh Mousavi, thank you for helping teach me the magic, and occasionally allowing me to pass it on.

To the general JASLab and uOttawa crew. There are unfortunately too many of you to thank individually, but your friendship and cheer have kept me in good spirits throughout my tenure here.

To the technical team who have kept the laser running, Andrei Naumov, Dave Crane and Ryan Kroeker (and for the trips to Pataterie Hulloise for poutine).

To the theorists who have gone on the chiral photoelectron journey with me, George Katsoulis and Agapi Emmanouilidou.

To all my friends and family who have supported me along the way, for listening to my complaints, sharing my joy, and helping me pick myself up when I've fallen down.

To my partner Abbie Bray, for shining a light on the darkness that was the past three years. I can't begin to properly thank you for all the things that you do, so I will simply say that my life is so much better for having you in it.

And finally, to the people who have supervised and advised me throughout this degree, Paul Corkum, David Villeneuve and above all, André Staudte. This degree would not have been possible without André's guidance, support, and friendship: thank you for helping sculpt me into the scientist I am today.

Contents

List of Figures

List of Tables

Chapter 1

Introduction

"If you wish to bake an apple pie from scratch, you must first invent the universe."

Carl Sagan

It is the goal of this thesis to present the findings of an ultrafast optical experiment probing the response in chiral molecules due to a novel chiral field. So, in the words of the great Carl Sagan, we must first invent the ideas of ultrafast optics and chirality, which will be performed in this Chapter.

The first successful demonstration of the laser in 1960 by Theodore Maiman [1] based on the ideas of Charles Townes and Arthur Schawlow [2] was the first step in an optical revolution that would go on to change the world. The laser has become ubiquitous in life as we know it; computers, communications, and medicine are but a small sampling of areas that would not have evolved as they have without the influence of laser light.

What makes the laser so special? The answer is beautiful in its simplicity: laser radiation is both directed and coherent. A typical light source such as the sun or a light bulb emits photons of a random colour, in a random direction at a random time. This is illustrated in Figure 1.1.

This picture, of course, oversimplifies the laser. Indeed, a laser can also emit photons of multiple wavelengths, and when these are combined coherently, can be used to generate a pulsed laser output. When several frequencies around the same wavelength are combined with random phases, seen in Figure 1.2a, the sum behaves erratically. However, if the phases of each wavelength are matched such that all frequencies peak at the same time, the sum shows a large peak at that time, and lower amplitude everywhere else, shown in Figure 1.2b.

This was demonstrated using only five frequencies, but the pulsed lasers used in our lab, centred on 800 nm, typically have bandwidths on the order of 100 nm. When the frequency spectrum becomes expanded in that way, the peaks become extremely high in field, and narrow in time. Typical numbers for our laser output are electric fields

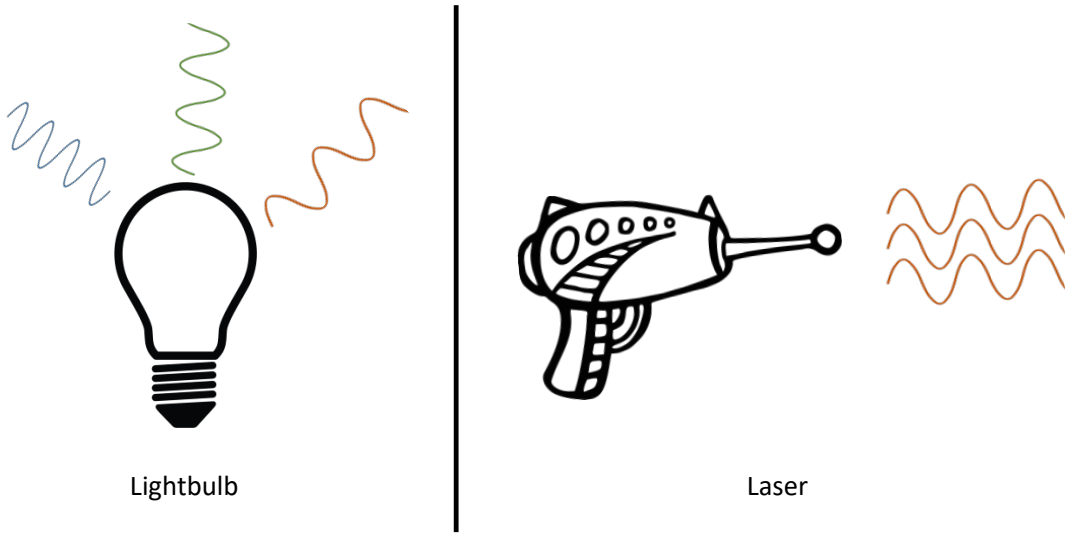

FIGURE 1.1: Laser coherence in demonstration: a lightbulb radiates photons of different colours in many disparate directions and varying times, an incoherent process. A laser emits photons in the same direction, released at the same time, which is coherent.

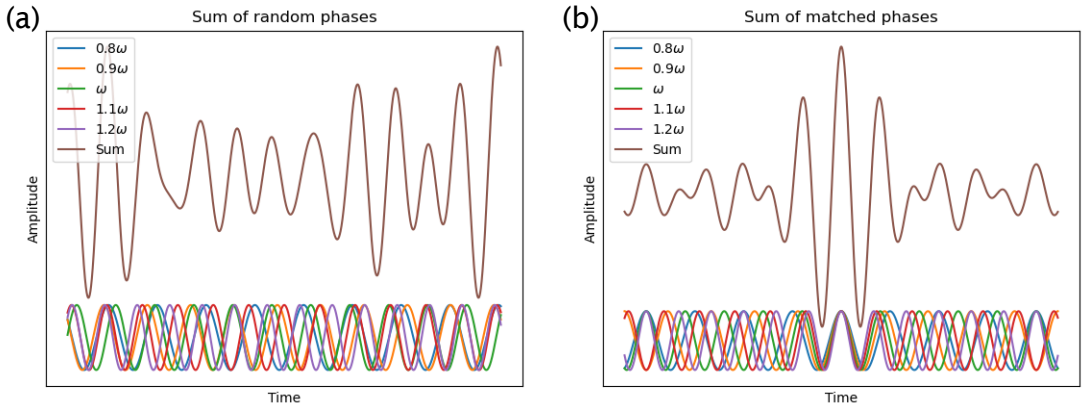

FIGURE 1.2: The addition of five sine waves with slightly varying frequencies. Panel (a) shows the result with arbitrary phase between them, and panel (b) if all waves peak at time 0. The sum is offset for emphasis.

on the order 3×10^{10} V/m and time scales of 25 fs. In general, the bandwidth/pulse duration relation for a Gaussian pulse shape is given by:

$$\Delta\tau = \frac{0.441}{\Delta\nu}, \tag{1.1}$$

where $\Delta\tau$ is the pulse duration and $\Delta\nu$ is the spectral width. This formula applies only to Gaussian pulse shapes, and is so-called "transform limited", which means that this is the lowest possible pulse duration for such a bandwidth.

A field of light with this strength and time scale is broadly useful, with many applications such as laser machining (see for example [3], who claim "after the age of steam and the age of electricity we have entered the age of photons now") or to drive nuclear fusion reactions (such as in [4]). Scientifically, the advantage of such fields is inherently clear: they reach and surpass the same natural time scales and potentials of atoms, molecules and electrons, allowing us to probe chemical reactions and dynamics on a previously unobtainable scale. A subject matter whose study has been unlocked by the continued development of ultrashort techniques is all-optical probing of chirality.

Chirality is a geometric property associated with three-dimensional bodies which dictates that objects may be made of the same constituent parts, but cannot be transformed via rotation or translation to superimpose. This is due to an inherent "handedness" of these objects, such as in Figure 1.3, meaning the objects can only be superimposed by a reflection operation. In chemistry, molecules which are chiral are called enantiomers, and are denoted by the notation R- and S- or (+) and (-) for "right" and "left" handed respectively. A solution of molecules of only a single handedness is "enantiopure", whereas an equal mix is "racemic". The physical properties of such molecules are typically nearly identical between different enantiomers, so one might ask, why does it matter?

The answer lies in biology; despite the nigh indistinguishable physical properties, enantiomers can interact wildly differently in biochemistry. An interesting question to ponder lies in our DNA, which spirals in an almost exclusively right-handed fashion (a recent proposal [5] suggests that this was chosen mutagenically over time by interaction with cosmic rays.) But to me, the drug thalidomide is perhaps the most obvious and tragic example of the dangers of ignoring chiral differences. Thalidomide (see Figure 1.4) was a drug marketed in the late 1950's to combat the effects of anxiety, trouble sleeping, and in particular, morning sickness in pregnant women. Thalidomide was dispensed in a racemic mixture, where the R- molecule had the desired effect, but the S- enantiomer could cause death or severe birth defects in the unborn children. In fact, thalidomide can even convert between enantiomers *in vivo* [6]. The drug was soon pulled from pharmacy shelves, but not before affecting upwards of 10,000 lives.

This tragedy underscores the importance of fully studying chiral molecules to be

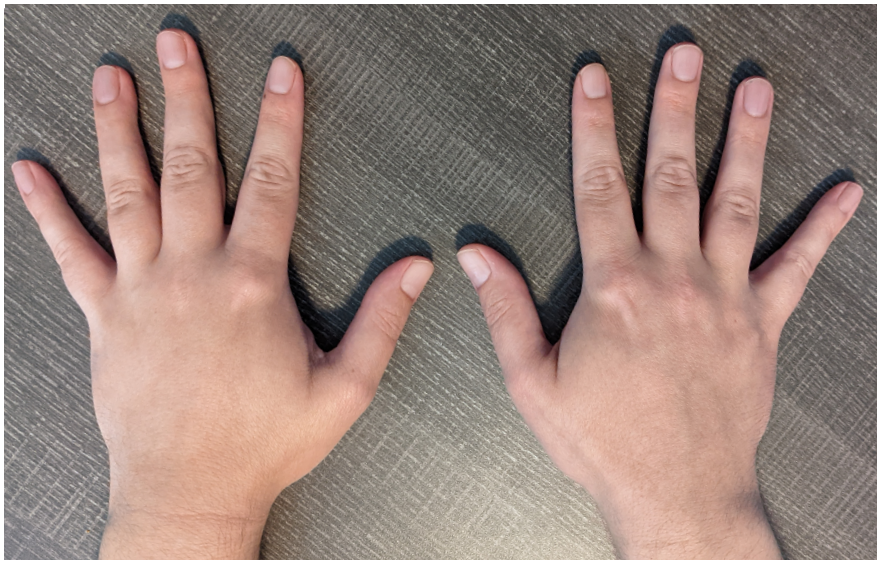

FIGURE 1.3: A picture of the author's modelesque hands. Despite his extensive knowledge of their backs, he is sadly incapable of superimposing them due to their chirality.

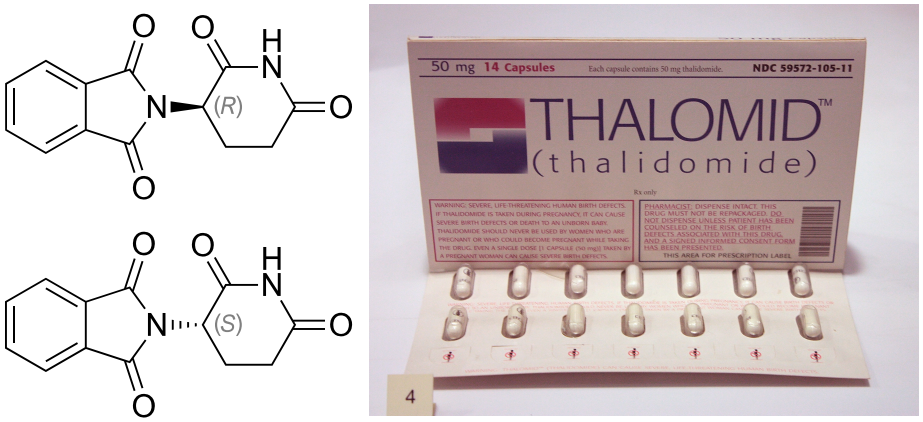

FIGURE 1.4: The molecular structure of R- and S-Thalidomide, as well as the packaged drug. Images taken from Wikipedia [7].

used in pharmaceuticals; in general, more than one third of all synthetic drugs are chiral and marketed in racemic mixtures [8]. Typically, it is very difficult to characterize the differences between enantiomers from a physical perspective, but over the past 20 years, new optical techniques have been developed and improved to do just this. Circularly polarized light is an example of such a technique, where the response from clockwise and counterclockwise polarization is different. It is the goal of this thesis to study and continue to improve similar tools, using ultrafast optical methods to distinguish between and perhaps even selectively create enantiomers.

This thesis will be organized as follows:

- Chapter 2 will focus on the theory and background required to understand the fundamentals of strong field physics. I begin by discussing ionization using ultrashort pulses, after which a brief demonstration of experiments allowed by a COLd Target Recoil Ion Momentum Spectroscopy (COLTRIMS) apparatus is shown. This is followed by an overview of previous chiral work in ultrafast science.

- Chapter 3 covers the experimental knowledge needed to perform the investigations detailed in this work. The Joint Attosecond Laboratory (JASLab) laser system is shown, followed by a detailed review of the COLTRIMS machine used to record data. Finally, a thorough explanation of the optical setup I used is presented, as well as a discourse of the trials and tribulations required to achieve such a novel setup.

- Chapter 4 reveals the results of my work. Direct comparisons between the ionization of each enantiomer of propylene oxide and its fragments are presented, and a three-dimensional chiral signal is shown. An attempt to characterize the degree of inherent chirality of the measurement is discussed. Last, the effect of chiral pulses on yield of ionization is investigated.

- Chapter 5 provides a summary of the work discussed in this thesis, discusses a future outlook for similar chiral concepts, and presents some concluding remarks.

- Appendices A and B provide discussions of two other papers that I have contributed to, but were not the primary focus of my thesis topic. Appendix A will look at imaging the character of an ionic spin orbit wavepacket, and Appendix B measuring light-induced conical intersections in H_2.

- Appendix C will deliver a brief tutorial intended for new users on the computer system used in our measurements. Topics covered include using the Cobold data acquisition software, and instructions for using the delay stage.

Chapter 2

Theory and Background

"I refuse to answer that question on the grounds that I don't know the answer."

Douglas Adams

In this chapter, I will introduce the theory behind strong field ionization, then discuss a background of measuring various photoionization phenomena. Next, an overview of chiral discrimination techniques will be presented, after which a new type of chiral light field, upon which the experiments in this thesis are based, is explained.

2.1 Strong Field Ionization

Electrons are a treasure trove of information, which when measured, unlock boundless secrets regarding the mechanics and processes of atomic and molecular physics. In turn, this can unlock the deepest secrets to understanding the matter around us. In order to collect this information, electrons must be liberated from their parent atom or molecule by surpassing the binding potential, given in Equation 2.1. For a very simple approximation of the electrostatic binding potential $V(r)$ of the outermost electron of an unperturbed, neutral atom of number Z, we may use a Coulomb potential:

$$V(r) = -\frac{Zq_e^2}{4\pi\epsilon_0}\frac{1}{|r|}\,. \tag{2.1}$$

Applying a strong field, such as the one discussed in Chapter 1 with electric fields on the order of 3×10^{10} V/m and time scales of 25 fs, allows us to surpass this potential by confining the energy of the field into a short, controlled burst. This leads to a regime of physics well beyond the linear domain of single photon absorption described by Einstein's photoelectric model in 1905.

In this section, we review the methods of strong field ionization via which the binding potential can be surpassed, and some of the consequences of doing so. The generation of such a field will be discussed in Chapter 3. The main factor which influences the ionization process is the intensity, or energy per unit area and time of the laser light given in W/cm^2. This means that increasing the flux of photons, or decreasing the duration of laser pulse or area it's focused into will all increase the intensity experienced by the atom. We may define two regimes based on the laser intensity, called multiphoton ionization and tunnelling ionization.

2.1.1 Multiphoton Ionization

At lower field intensities, typically $< 10^{13}$ W/cm^2 for 800 nm, ionization largely occurs due to the absorption of many photons, whose combined energy allows an electron to surpass the binding potential. In general, the rate of ionization with n photons, β_n, obeys a power law:

$$\beta_n = \sigma_n I^n \,, \tag{2.2}$$

where σ_n is a generalized n-photon ionization cross section, and I is the intensity. A visual representation of this process can be seen in Figure 2.1. As an example, we typically use 800 nm light, whose photon energy is slightly higher than 1.5 eV, so to surpass the binding energy of atomic hydrogen (13.6 eV), it would take the absorption of 10 photons.

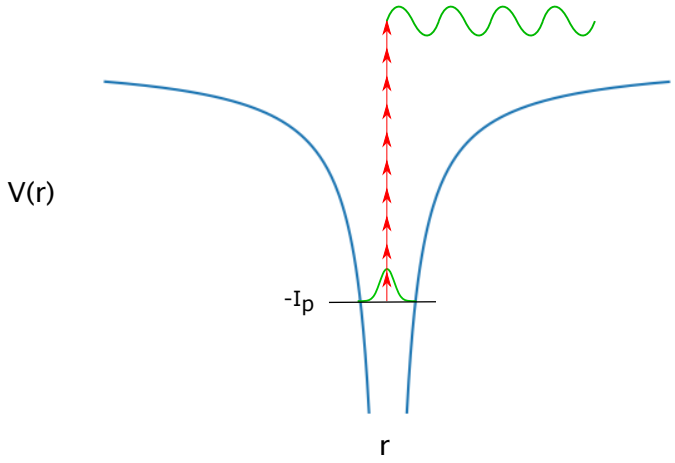

FIGURE 2.1: An electron is ionized via a multiphoton process. Many photons, indicated by the red arrows, whose sum energy are higher than the ionization potential are absorbed, ejecting the initially bound electron wavepacket into the continuum.

Ordinarily, one would expect that an electron that is already ionized would not be able to absorb further photons due to the conservation of angular momentum. However, if the electron is still local to the parent ion and coupled to the Coulomb field, the absorption of further photons occurs. This is easily detectable in experimental measurements, and demonstrates a pattern of peaks or rings of increasing energy (first measured by Agostini in 1979 [9]), named Above Threshold Ionization (ATI); for detailed information, see a 2006 review [10]. The spacing between successive rings corresponds to the photon energy absorbed. An experimental example can be seen in Figure 2.2, where electron momentum from ionization of Br_2 is plotted. Clear ATI rings, indicated by arrows, can be seen as momentum (energy) increases.

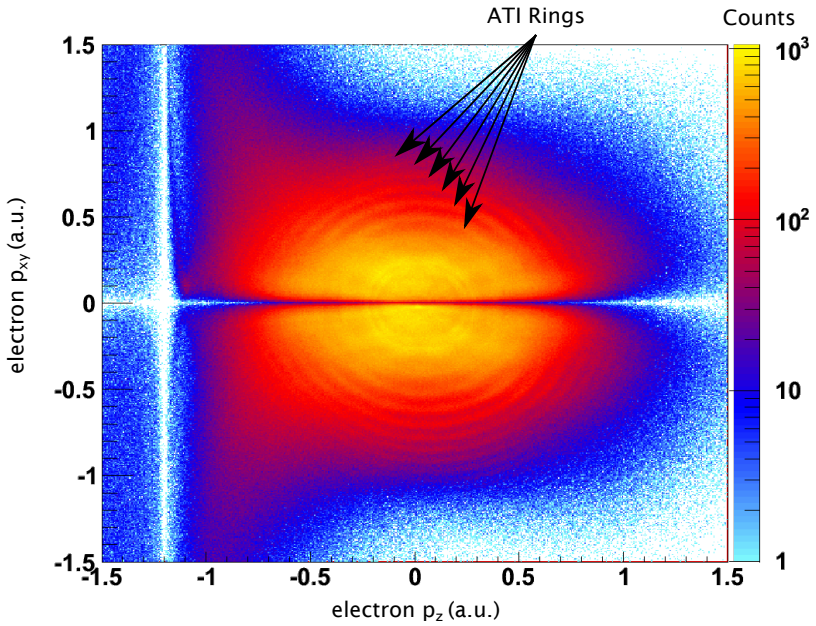

FIGURE 2.2: Experimental photoelectron spectrum from ionization of Br_2. Arrows indicate ATI rings, caused by absorbing successively higher numbers of photons. Data is unpublished, and taken by the author.

2.1.2 Tunnel Ionization

At higher intensities, the oscillating electric field $E(t)$ is strong enough to cause a relevant distortion to the binding potential. In this case, the total potential V_{tot} becomes:

$$V_{tot}(r,t) = -\frac{Zq_e^2}{4\pi\epsilon_0}\frac{1}{|r|} - q_e r E(t)\,. \tag{2.3}$$

This distortion is shown in Figure 2.3, and yields a time dependent barrier through which an electron can tunnel (as in elementary quantum mechanics).

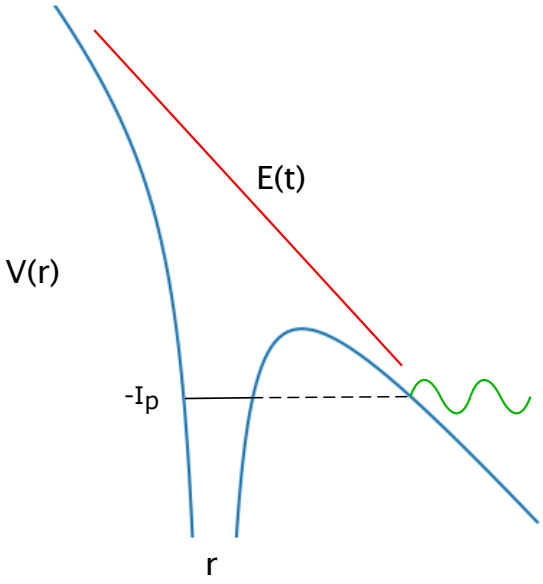

FIGURE 2.3: An electron experiences tunnel ionization. An external electric field distorts the Coulomb potential of the parent ion, allowing the electron to tunnel into the continuum.

If the intensity of the field is sufficient, the barrier can even be completely suppressed, leading to a freely escaping wavepacket in a process named over barrier ionization.

2.1.3 The Keldysh Parameter

For a quantitative analysis of the method of ionization, Keldysh [11] defined the parameter γ in 1965:

$$\gamma = \sqrt{\frac{I_p}{2U_p}}\,, \tag{2.4}$$

where I_p is the ionization potential of the system and U_p is the ponderomotive potential, given by:

$$U_p = \frac{q_e^2 E^2}{4 m_e \omega^2}\,, \tag{2.5}$$

with E the electric field amplitude, and ω the frequency of field. Physically, the ponderomotive potential represents the average energy of the quivering motion of a free electron in an electric field.

The Keldysh parameter helps analytically identify the two regimes. When $\gamma \gg 1$, multiphoton ionization is the primary mechanism, and when $\gamma \ll 1$, tunnelling ionization dominates. When $\gamma \approx 1$, the two mechanisms have been shown [12] to operate in

harmony - the tunnelling model still makes accurate predictions, while ATI peaks are still visible.

2.1.4 ADK Theory

One of the most commonly used theoretical developments in strong field physics was published by Ammosov, Delone and Krainov in 1986 [13], and is now colloquially referred to as "ADK Theory" or the "ADK formula". This model, which predicts tunnel ionization probability under oscillating electric fields, was derived from tunnelling theory for a hydrogen atom, but is generalized to be applicable for more complex atoms, as well as those in arbitrary quantum states. The ADK formula for linearly polarized light, in their own formalism, is as follows:

$$\omega_{ADK} = \sqrt{\frac{3n^{*3}E}{\pi Z^3}} \frac{ED^2}{8\pi Z} \exp\left(-\frac{2Z^3}{3n^{*3}E}\right), \tag{2.6}$$

where Z is atomic number (or charge of the atomic core), E is the applied electric field, n^* is an effective principle quantum number given by

$$n^* = \frac{Z}{\sqrt{2I_p}}, \tag{2.7}$$

and D is defined as

$$D \equiv \left(\frac{4eZ^3}{En^{*4}}\right)^{n^*}. \tag{2.8}$$

This framework was further extended [14] to give the ionization rate of electrons with a given momentum, both in the directions parallel $p_\parallel$ and perpendicular $p_\perp$ to the applied linearly polarized laser field:

$$\omega_{ADK}(p_\parallel, p_\perp) = \omega(0) \exp\left[-\frac{p_\parallel^2 \omega^2 (2I_p)^{3/2}}{3F^3} - \frac{p_\perp^2 (2I_p)^{1/2}}{F}\right]. \tag{2.9}$$

Similarly, in 2002 the capability of the model was advanced to account for molecules by Tong, Zhao and Lin [15], known as the Molecular-ADK, although this will not be discussed in depth in this thesis.

The ADK model has been broadly used to great success by many theorists to predict and support experimental results. Some examples include Zhao, and later Pavičić predicting angular dependence of ionization of molecules [16, 17], Brabec analyzing tunnel ionization in large systems [18], and Emmanouilidou identifying mechanisms in nonsequential double ionization [19] (NSDI, which will be discussed in Section 2.2.2).

2.2 Photoionization Phenomena in COLTRIMS

The apparatus used in our measurements, a COLTRIMS (COLd Target Recoil Ion Momentum Spectroscopy) system, described in detail in Chapter 3, is an extremely versatile instrument that can be used to detect a wide variety of post-photoionization molecular phenomena. It is valuable to review a select set of these measurements in order to get a sense of the capabilities of a COLTRIMS apparatus. We break this section into three parts: processes which involve the elastic scattering of electrons, processes which involve the inelastic scattering of electrons, and dissociation pathways of H_2^+.

2.2.1 Elastic Scattering of Electrons

Depending on timing and the driving field, after an electron has been ionized, there is a chance that it returns to the parent ion. The subsequent scattering in the molecular potential yields a rich variety of physics, much of which can be detected or used in a COLTRIMS system. Here I review some of the mechanics and measurements that have occurred as a consequence of an electron's journey home. This particular section will cover elastic scattering processes.

Laser Induced Electron Diffraction

In 2008, Meckel *et al* [20] published an experiment that makes use of an ionized electronic wavepacket in two different processes. First, part of the wavepacket escapes directly to the detector, providing information on the ionizing orbital filtered by tunnelling. Second, the remaining portion is driven back to the parent ion, and elastically scatters, causing diffraction through the molecule. This so called laser induced electron diffraction encodes information about the nuclear structure of the molecule. An cartoon of these processes is shown in Figure 2.4

In order to resolve the electronic structure of the targets, O_2 and N_2, the molecules were aligned, which was achieved using a pump-probe pulse setup. The pump pulse, polarized along the y-axis, excites a rotational wavepacket, causing the molecules to oscillate between alignment along the y-axis, and an anti-aligned character confined to the xz-plane. The probe pulse, polarized along z, then arrives a fixed time later, controlled using a delay stage, selectively ionizing at peak alignment or anti-alignment.

Presented in Figure 2.5 are the full 3D electron momentum spectra of O_2 and N_2 measured using COLTRIMS. A normalized difference between the aligned and anti-aligned cases has been applied, where the value in each pixel is given by:

$$N_{ND} = \frac{N_a}{N_{a,tot}} - \frac{N_{aa}}{N_{aa,tot}}, \tag{2.10}$$

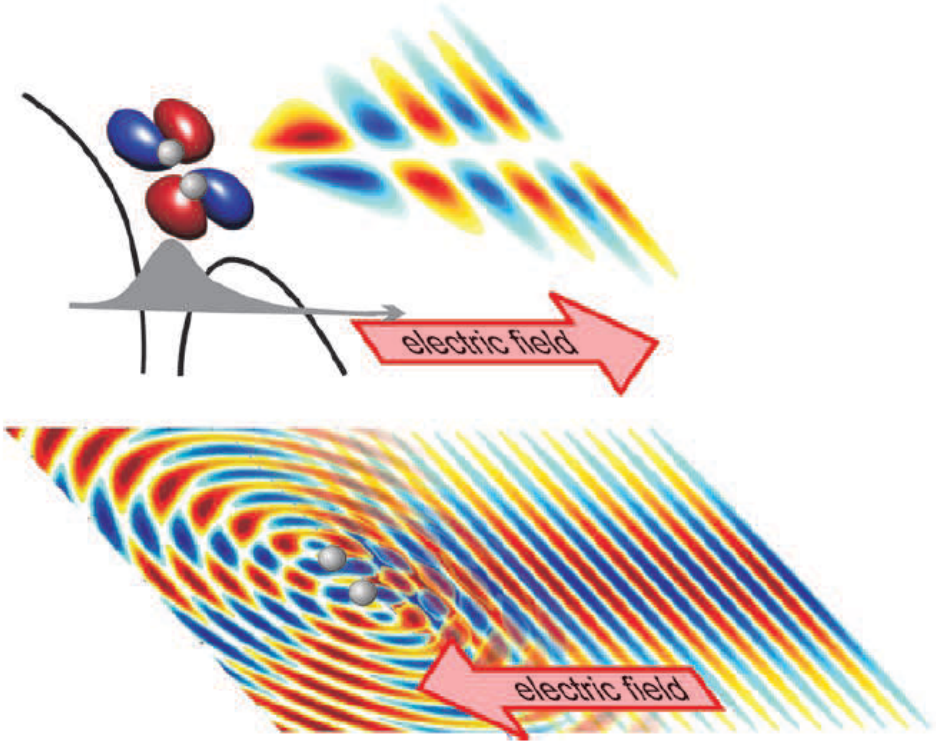

FIGURE 2.4: In the top image, part of the ionized electron wavepacket escapes directly to the detector. This portion of the wavepacket yields information regarding the molecule's highest occupied molecular orbital. The other part of the wavepacket is returned to its parent ion by the electric field, and diffracts through the molecule, shown in the bottom half. Taken from [20].

with N_a and N_{aa} the number of counts in that pixel in the aligned and anti-aligned case respectively, and $N_{a,tot}$ and $N_{aa,tot}$ the total number of counts in the distribution.

Electrons from Figure 2.5 with momenta in the range $\sqrt{p_x^2 + p_y^2} < 0.5$ and $|p_z| < 1.5$ show clear signs of the structure of the highest occupied molecular orbital (HOMO). In particular, it is striking to observe that the patterns in the p_{xy} plane retain the symmetry of the HOMOs, shown just above the plot. Meckel *et al* performed simulations using the wave functions of the molecules and classical propagation to verify these results.

The source of electrons with higher momentum ($\sqrt{p_x^2 + p_y^2} > 0.5$ and $|p_z| > 1.5$) is predominantly elastic scattering, and carries information regarding diffraction from the molecule. Meckel *et al* analyzed the probability of scattering at a given angle by removing the influence of the laser field on the electrons, again showing excellent agreement with their calculation.

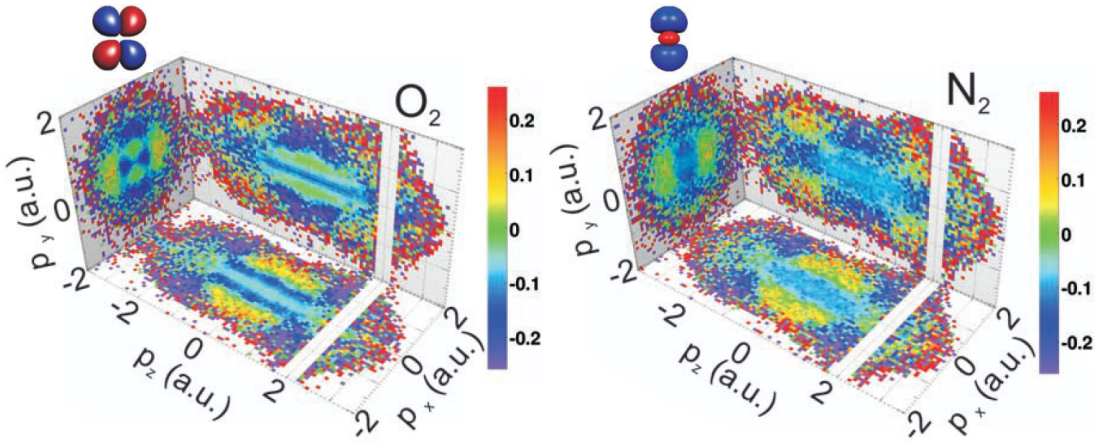

FIGURE 2.5: Full 3D electron momentum spectra of ionization from O_2 and N_2. Data shown are normalized differences between when the molecule is aligned along the y-axis and at anti-aligned character for each molecule. The HOMO is presented just above the plots. Taken and adapted from [20].

Photoelectron Holography

Later, in 2014, Meckel *et al* [21] performed a very similar experiment, which focused instead on electron holography rather than electron diffraction (although photoelectron holography was first discussed in 2011 [22]). The concept is simple: in order to obtain holographic information, a reference wave, direct from a source, must interfere with a signal wave, which scatters off a target and encodes structural information. In photoelectron holography, the reference wave corresponds to electron wavepackets which are directly ionized from a molecule. The signal wave is made up by electrons which return to the parent ion and subsequently scatter in the parent ion's potential. These interfere when they have the same final momentum.

In the case of Meckel *et al*, they investigated the holographic signal as a function of the angle of alignment of N_2. Again, a pump-probe setup is used to achieve this, where the pump pulse is passed through a half-wave plate in order to align the molecule to the desired angle, and the probe pulse performs the ionization.

Shown in Figure 2.6 is the data recovered for molecular alignment perpendicular to the probe, at 45° to the probe, and parallel to the probe. Similar to the experiment discussed in Section 2.2.1, normalized differences have been applied to the data, but this time each alignment is compared with a distribution composed of the sum of all alignments from 0° to 180° in 2° steps. A simulation which solves the 2D time-dependent Schrödinger equation is shown in the same figure, contrasting the experimental data.

What Meckel *et al* went on to conclude is that the obvious shift of the fringes as alignment angle changes is due to the ionization step, not the scattering. When the molecule is at an angle to the polarization of the ionizing field, the wavepacket is emitted with

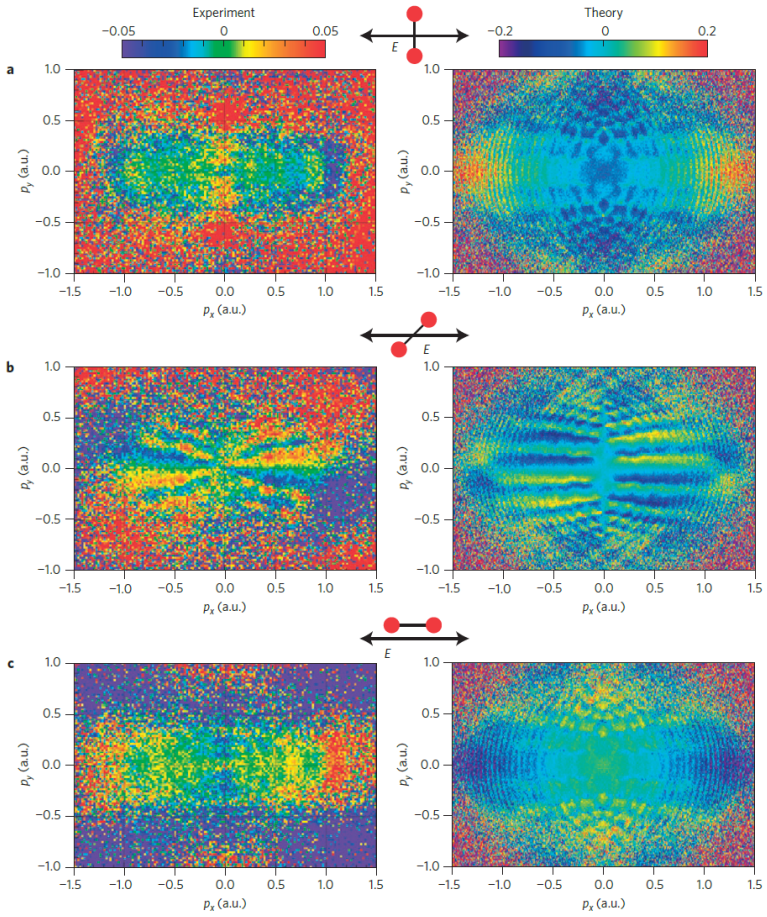

FIGURE 2.6: Electron momenta in the plane perpendicular to the ionizing field. Three different measurements are presented, at varying alignments of N_2 with respect to the field: perpendicular in (a), 45° in (b) and parallel in (c). Data is shown with normalized differences, where the sum of all alignments from 0° to 180° in 2° steps is the reference. Taken from [21].

a phase structure that is offset from the molecular centre. This structure is preserved during travel through the continuum, and ultimately causes the shift.

Photoelectron holography has continued to be a rich topic offering interesting insights into strong field phenomena. For more information, consider perusing the theses of Maxwell from 2018 [23] or Bray in 2022 [24].

2.2.2 Inelastic Scattering of Electrons

When the electron returns to the parent ion, there are also processes that make use of its energy; this section will cover inelastic scattering processes.

Nonsequential Double Ionization

First recorded by L'Huillier *et al* in 1982 [25], the probability of double ionization as a function of intensity has a curious "knee" structure, as shown in Figure 2.7. The probability of ionization, several orders of magnitude higher than was expected given available theory at the time, is due to the correlation of the ionization events, and is thus deemed nonsequential double ionization (NSDI). In an NSDI process, the first electron ionized is driven back to its parent ion by the laser field (as is described shortly in Section 2.2.2), where the so-called rescattering can cause impact ionization.

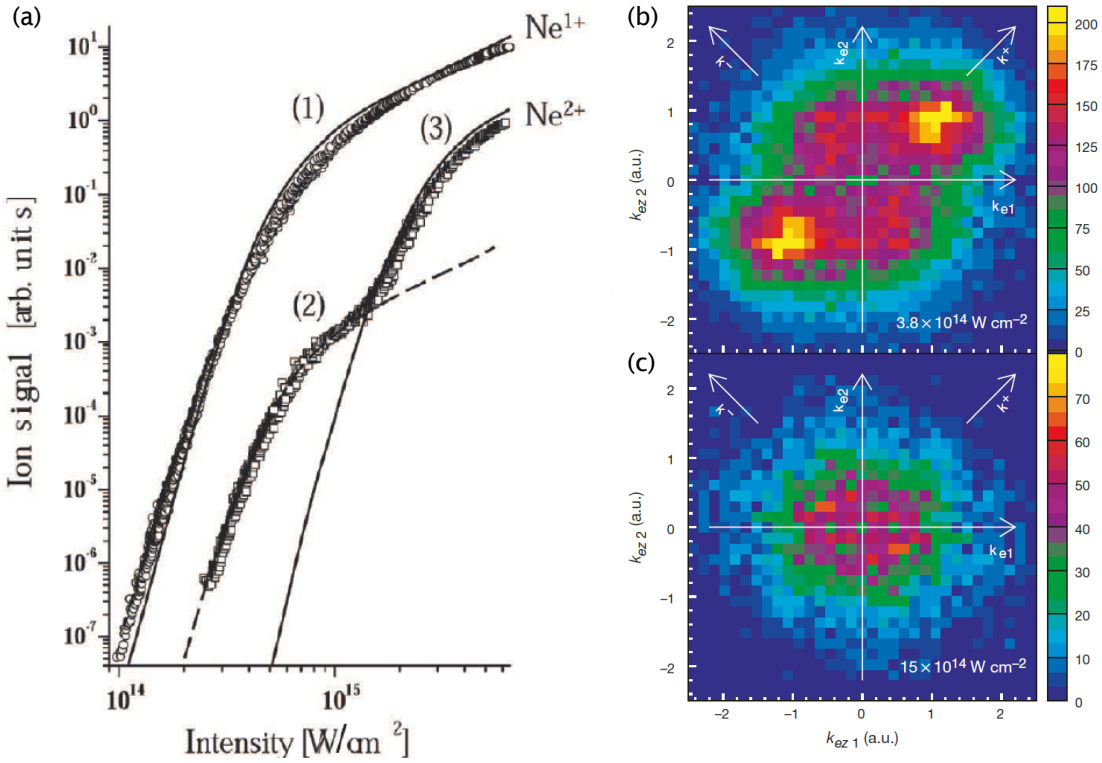

FIGURE 2.7: Shown in panel (a) is the ionization probability as a function of intensity for Ne^{+} and Ne^{2+}. A "knee" structure is observed between curves (2) and (3). Electron correlation for lower (b) and higher (c) intensity. The correlation shown in (b) corresponds to NSDI, while the lack of correlation seen in (c) is typical of sequential ionization. Taken from [26] and [27].

A beautiful confirmation of this model was shown by Weber *et al* in 2000 [27], as seen in panels (b) and (c) of Figure 2.7. In this work, a COLTRIMS is used to measure the momenta of both the first and second ionized electrons, which is then compared in a correlation spectrum. The momentum of the first electron along the polarization direction is presented on the x-axis, whereas the y-axis shows the momentum of the

second electron. At lower light intensities in (b), we can see that the electrons are significantly more likely to be emitted in the same direction along the polarization direction. At higher intensities, shown in (c), when the ionization events are sequential (independent), no correlation is observed.

There has since been considerable work studying NSDI; for further summary, the thesis of Kübel in 2014 [28], or the work of Bergues [29] are highly educational.

High Harmonic Generation

There is another consequence of electrons returning to their parent ion, whose history and study is extremely influential in ultrafast science; this is of course, high harmonic generation (HHG). To truly discuss high harmonic generation and its applications would take a textbook (for example see Chang [30]), but a simple summary of the main principles here will suffice. Note that COLTRIMS apparati have been designed and built to use high harmonics as a table-top high energy light source. These systems are impressive technical achievements, and I highly recommend perusing [31–33], e.g., for more details. Keep a lookout for the emergence of a new system in Ottawa!

I posit that any student in the JASlab group submitting a thesis that has not described the three step model of HHG (alternatively called the simple person's model), pioneered by Kulander [34] and Corkum [35], has failed in a requisite portion of their duties. The three step model is diagrammatically shown in Figure 2.8. First, an electron wavepacket is tunnel ionized when an external oscillating electric field distorts the binding potential, as discussed in Section 2.1.2. Next, the wavepacket travels in the continuum, and is accelerated by the electric field. As the field follows its time evolution, the sign of the vector potential changes, and begins to accelerate the wavepacket back to its parent ion. Finally, the electron recombines with the ion, and releases the energy it gains during its trajectory in the form of light.

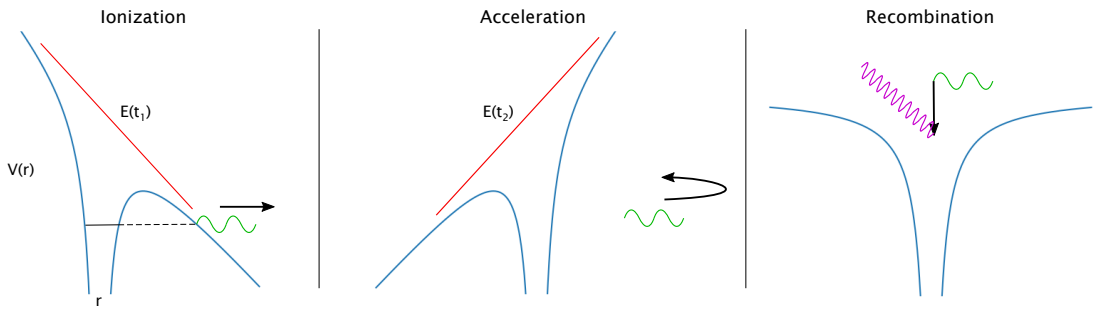

FIGURE 2.8: The three step model. A wavepacket is tunnel ionized by an external oscillating electric field, then accelerated through the continuum by said field. Eventually, the field changes sign and accelerates the wavepacket back to the ion, upon which point the electron recombines and releases its energy as light.

Mathematically, this can be described as follows. For an external field polarized in x, and with amplitude E and driving frequency ω, the equation of motion of a free classical electron is given by:

$$\frac{d^2x}{dt^2} = -\frac{q_e}{m_e} E\cos(\omega t)\,. \tag{2.11}$$

Then if the electron is freed at time t', the velocity $v(t)$ and position $x(t)$ are

$$v(t) = -\frac{q_e}{m_e\omega} E\left(\sin(\omega t) - \sin(\omega t')\right)\,, \tag{2.12}$$

and

$$x(t) = -\frac{q_e}{m_e\omega^2} E\left[\left(\cos(\omega t) - \cos(\omega t')\right) + \omega\sin(\omega t')(t-t')\right]\,. \tag{2.13}$$

Similarly, the kinetic energy gained by the electron, corresponding to a photon emission with frequency ω_H is then:

$$\hbar\omega_H = \frac{1}{2}m_e v(t)^2 = \frac{q_e^2}{4m_e}E^2\left(\sin(\omega t) - \sin(\omega t')\right)^2 = 2U_p\left(\sin(\omega t) - \sin(\omega t')\right)^2\,. \tag{2.14}$$

To retrieve the recombination energy, we seek to find the time such that $x(t) = 0$, which gives the following condition:

$$0 = \left[\left(\cos(\omega t) - \cos(\omega t')\right) + \omega\sin(\omega t')(t-t')\right]\,. \tag{2.15}$$

This equation cannot be solved analytically, but numerically it can be found that the maximum kinetic energy gained is $3.17U_p$.

If the pulse driving the generation of harmonics is longer than one cycle, there will be multiple opportunities to generate harmonics per pulse. This leads to interference in the spectrum, typically causing odd integer multiples of the driving frequency to be enhanced, and even ones to be suppressed due to the destructive interference between consecutive half cycles of the field. It is possible to achieve high intensity even harmonics in several ways however. These techniques involve breaking the inherent symmetry of the system, such as by using asymmetric laser fields [36], non-homonuclear molecules such as in [37] or in Section 2.3.4 with chiral molecules, and moving to solid media [38].

One of the exciting features of high harmonic generation is that it can be used to probe the structure of molecules. As an example of this utility, we will look at tomographic imaging of molecular orbitals Itatani *et al* performed in 2004 [39]. In this work, N_2 is aligned with a pump pulse (as described in Section 2.2.1), and a probe pulse generates harmonics by ionizing from the HOMO. The polarization of the probe pulse with

respect to the alignment of the molecule is varied from 0° to 90° at intervals of 5°, and the intensity of each harmonic order is measured, as shown in Figure 2.9 a.

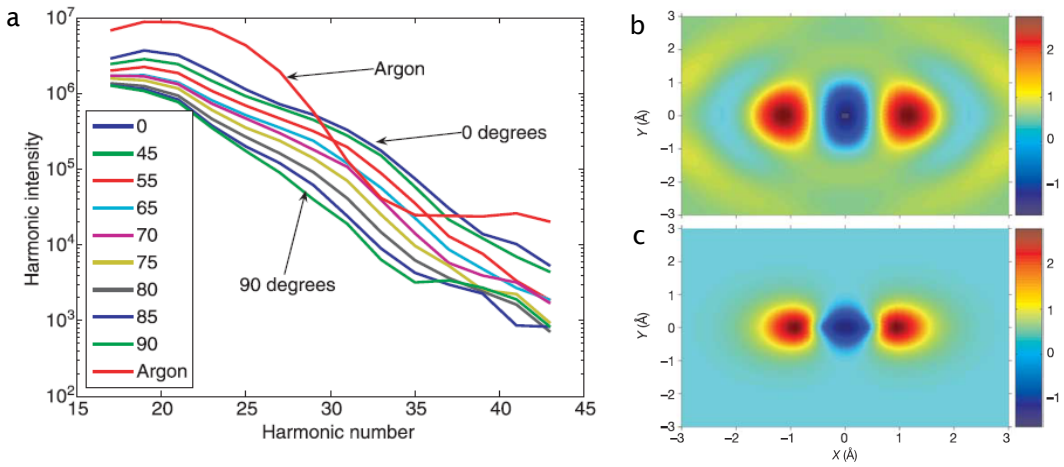

FIGURE 2.9: High harmonic spectra measured from N_2 as the angle of probe polarization is varied between 0° and 90°, shown in (a). The reconstructed HOMO and the a calculation of the N_2 $2p\sigma_g$ orbital are presented in (b) and (c) respectively. Taken and adapted from [39].

The molecular orbital is then reconstructed by considering the electron's recollision. After its trip through the continuum, the wavepacket of the electron is a plane wave which will overlap with the bound-state wavefunction. The addition of the two induces a dipole, which oscillates as the electron propagates, and emits the high harmonic radiation. Measuring the harmonic spectrum in amplitude, phase and polarization is a direct experimental determination of the Fourier components of the spatial HOMO. Figure 2.9b shows a reconstruction of the HOMO using the measured harmonics, and 2.9c the shape of the N_2 $2p\sigma_g$ orbital from performing an *ab initio* calculation.

Indeed, the technique of imaging molecules using high harmonic spectroscopy has been wildly successful over the past two decades. For a summary of some of these results, such as imaging electron hole or nuclear dynamics, see [40]. We will further see in Section 2.3.4 that harmonic generation is an extremely valuable technique to measure signal differences between chiral enantiomers.

2.2.3 Dissociation Pathways of H_2^+

Another interesting topic that comes to mind is the rich dissociation dynamics that are accessible after ionizing the simplest of all molecules, H_2. Despite its low complexity compared to other targets, there are still papers coming out about H_2 to this day - not so elementary. Two of the papers I have contributed to over the course of my thesis cover subject matter relating to the ionization of H_2 [41, 42]. The first will be discussed standalone in Appendix B.

The main factors that control the pathway of dissociation of H_2^+ are the frequency, pulse duration, and intensity of the laser field causing the ionization [43]. In fact, one is able to perform a basic estimation of the intensity of the ionizing beam simply by looking at the energy distribution of H^+ ions, as shown in Figure 2.10 [44]. A time of flight of approximately 740 ns corresponds to an H^+ ion with no momentum along the time of flight direction. As the time of flight of a detected ion increases (or decreases), the momentum of the ion away (or towards) the detector increases in energy, ultimately creating three distinct peaks. Each of these three peaks (labelled in the bottom left panel as bond softening, above threshold dissociation, and charge resonance enhanced ionization) corresponds to a different mechanism of dissociation.

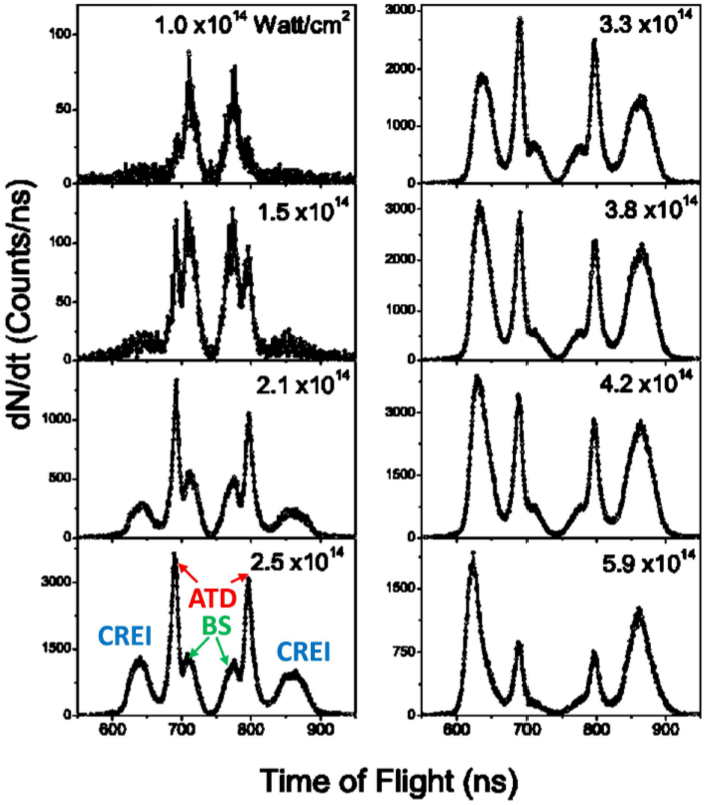

FIGURE 2.10: Time of flight of H^+ ions with varying intensity. The mechanism of dissociation, labelled as the peaks in the bottom left panel as bond softening, above threshold dissociation, and charge resonance enhanced ionization, depends strongly on the intensity of the ionizing field. Taken from [43], and adapted from [44].

Accessing these mechanisms depends strongly on the intensity of the ionizing field. Bond softening is a single photon process, above threshold dissociation is a 3(+) photon process, and charge resonance enhanced ionization is a multiphoton process typically thought of in a tunnelling picture; recall, the rate of ionization of a process with n photons scales with I^n. These three processes will be discussed in more detail below.

Bond Softening and Above Threshold Dissociation

First measured by Zariyev *et al* in 1990 [45], bond softening is the least energetic dissociation branch of H_2^+. It is convenient to discuss these dissociations in the Floquet picture, in which the ionizing light field dresses the molecular states. This overview will only be a brief summary: I point the reader to [46] for a more detailed review.

Shown in Figure 2.11 is a diagram of the first two ionic states, dressed in the Floquet picture. The ground state has σ_g character, while the first excited state has σ_u character. These dressed states are described by the notation $|g, n\rangle$, where g represents the symmetry (g for gerade, or even, and u for ungerade, or odd), and n corresponds to the number of photons dressing the state. A negative photon number corresponds to absorption, while positive is emission.

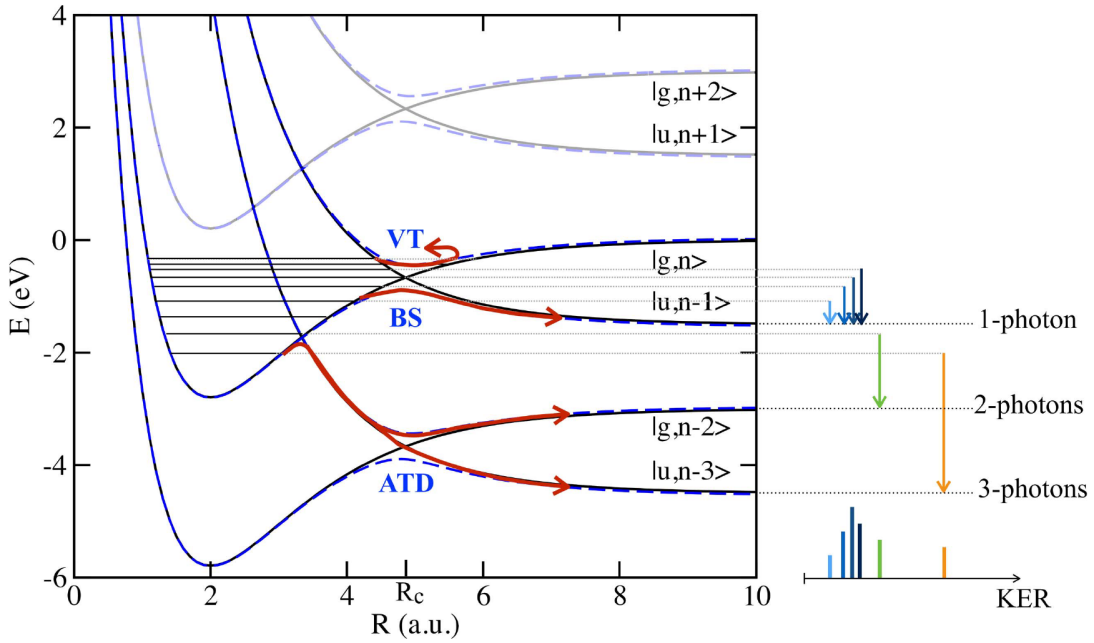

FIGURE 2.11: Potential energy curves of H_2^+ in the Floquet picture, dressed by n photons of 800 nm light. Black curves are diabatic, and the adiabatic dressed potentials are shown in blue. Red arrows denote difference mechanisms. A one-photon absorption from vibrational states in the ground ionic state describes bond softening dissociation (BS) and its counterpart without breakup, vibrational trapping (VT). Higher numbers of photons absorbed can lead to above threshold dissociation (ATD). Pathways in which 1-3 photons are absorbed are shown on the right, along with their kinetic energy release (KER). Taken from [43].

The diabatic potential energy surfaces of the ground and excited state cross at R_c. In the Floquet picture, the two adiabatic dressed states instead yield an avoided crossing at this point. The lower state now only has a small barrier before dissociation, and the higher the field intensity, the lower this barrier becomes.

With the field present, the vibrational states of the initial wavepacket are projected onto resonances induced by the field (see [47] for further details). This leads to the dynamics we are interested in describing: bond softening occurs when higher vibrational states couple with the lower dressed state, indicated by the BS arrow in Fig 2.11. These wavepackets no longer experience a potential well, and are able to escape, causing the molecule to dissociate. Similarly, if instead the resonances couple to the above state, there is a well indicated by the arrow labelled as vibrational trapping (VT), and the molecule is stable. This is alternatively referred to as bond hardening (see [48]).

Above threshold dissociation (ATD) is a more energetic process than bond softening, and was originally shown experimentally by Giusti-Suzor *et al*, and later Bucksbaum *et al* in 1990 [49, 50]. It is also described conveniently in the Floquet picture, and is included in Figure 2.11. The coupling in this case is from lower vibrational states in the $|g, n\rangle$ state to $|u, n-3\rangle$ after the absorption of 3 photons, or to $|g, n-2\rangle$ after reemitting one. An additional mechanism to access higher-order ATD, as seen in [51], is through the absorption of energies of an electron in the recollision process, as discussed in 2.2.2.

Charge Resonance Enhanced Ionization

First published at almost identical times by Seideman *et al* and Zuo *et al* in 1995 [52, 53], charge resonance enhanced ionization (CREI), or alternatively just enhanced ionization, is a consequence of an already dissociating H_2^+. As the internuclear distance between atoms increases, the Stark effect begins to increase the energy difference between the highest occupied molecular orbital (HOMO), labelled $1\sigma_-$, which gets downshifted, and the lowest unoccupied molecular orbital (LUMO), labelled $1\sigma_+$, which gets upshifted. This effect is seen in Figure 2.12: as R increases in panels (a), (b), and (c), the energy gap between $1\sigma_-$ and $1\sigma_+$ increases as well. Panel (d) shows that at intermediate internuclear separations, the ionization is enhanced considerably.

These HOMO and LUMO states are equivalent to localization by the laser on one proton or the other, effectively equal to $1s$ atomic orbitals. This explains the shape of the potentials in Figure 2.12(a)-(c). The twin peak structure of the ionization rate in panel (d) is due to two effects. At approximately 6-8 a.u., the localization effect causes the rate to increase sharply, and at approximately 10 a.u., the wavepacket becomes higher energy than its binding potential, freeing it.

Coulomb Explosion

Coulomb explosion, the most energetic dissociation, is also the easiest to describe. As laser intensity is increased, the probability of ionization increases non-linearly. At high enough intensities, it becomes not only possible, but likely for *both* H atoms to be ionized by the field. What remains in this case is two protons, which will repel each other

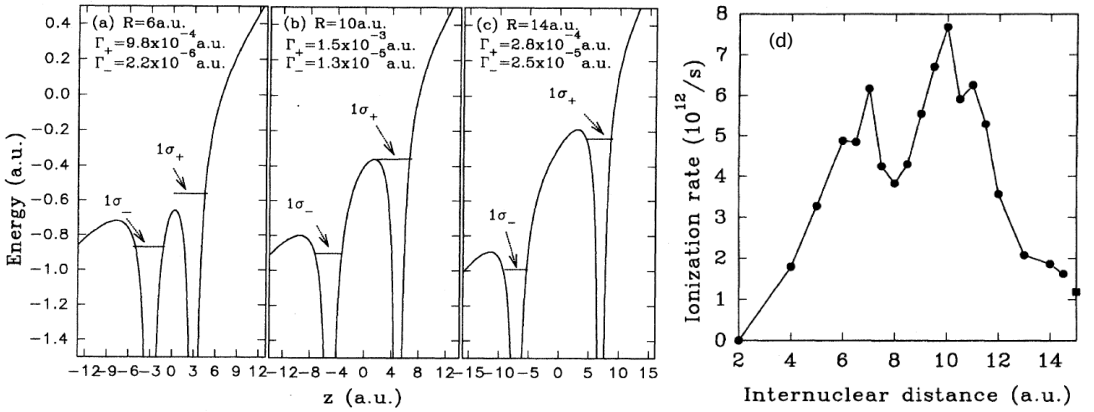

FIGURE 2.12: Potential energy surface of dissociating H_2^+. Panels (a)-(c) show the difference in energy of the HOMO and LUMO as the hydrogen atoms spread apart in the z-direction. Panel (d) shows the ionization rate as the internuclear distance increase. Taken from [53].

violently via the Coulomb force. It is worth noting that this process is inherently different from those previously discussed, as dissociation begins occurring instantaneously after ionization.

The instantaneous nature of this process is a huge boon if leveraged properly in a pump-probe setup, or even in theoretical methods, potentially "freezing" any nuclear dynamics occurring at the time of explosion. Examples of such results include Chelkowski *et al* imaging vibrational wave functions in 1999 [54], and Légaré *et al* measuring the dynamics of diatomic and triatomic molecules in 2005 [55].

2.3 Chiral Discrimination with Light

Interestingly, it is actually quite easy to observe the handedness of an enantiopure mixture using only a rudimentary knowledge of the polarization of light. This is due to a property of chiral materials called optical activity or optical rotation: the polarization of light passing through a chiral medium will be rotated. One can construct a simple polarimeter consisting of a light source followed by a linear polarizer and perpendicular (or rotatable) linear analyzer. As we know from rudimentary optics, if the polarizer and analyzer have perpendicular orientations, no light will pass through. If a chiral medium such as a simple fructose or dextrose solution is placed between the polarizer and analyzer, the polarization of the light is rotated due to optical activity, and the light successfully passes through the analyzer. The analyzer may be rotated to determine the exact angle of optical activity due to the chiral medium. Left-handed molecules will rotate the light counterclockwise, and right-handed molecules clockwise. The response is indifferent to the orientation of the molecules in the solution, since rotating a chiral

object cannot change its inherent chirality, and indeed the effect of the optical activity. In the same vein, one can also use x-ray crystallography to determine the exact configuration of a material [56]. However, these results are on the *bulk* level, whereas we are interested in obtaining a similar response from individual single molecules.

In this section, a thorough background of chiral experimentation in ultrafast optics will be presented. The holy grail of any such work would be an optical technique that yields a potent signal difference between left- and right-handed enantiomers on the single molecule level, or alternatively a way to influence the ionization yield of one enantiomer or another.

This section is broken into different experimental techniques used to study chiral molecules: we start with a direct molecular reconstruction with a Coulomb explosion imaging technique, a uniquely effective strategy for just one particular chiral molecule. Next, we look into methods which detect circular dichroism in photoelectron distributions, abbreviated PECD, in both single and multiple photon processes. The PECD signal is generally defined by $2\frac{I_S - I_R}{I_S + I_R}$, where I_S and I_R are the intensity of the observables from the S- and R-enantiomer respectively. We will see that no matter the technique, the overall PECD signal tends to be low. Finally, we will discuss chiral dichroism in high harmonic generation. This part will be split into two regimes: the first uses traditional elliptically and circularly polarized light schemes to measure chiral dichroism. The second uses novel techniques and multiple pulse schemes to induce a so-called synthetically chiral light, designed to elicit a massive dichroism signal in the harmonics.

2.3.1 Direct Molecular Reconstruction via Coulomb Explosion Imaging

One of the most beautiful experiments performed on chiral molecules was published in 2013 by Pitzer *et al* [57]. This work looked to exploit the simplicity of the smallest chiral molecule, bromochlorofluoromethane (CHBrClF), using Coulomb explosion imaging to separate ionization events relating to each enantiomer in a racemic mixture. A 40 fs pulse was used to ionize each of the 5 constituent atoms of CHBrClF, and a COLTRIMS was used to measure the momentum of each ion in coincidence from the resulting Coulomb explosion, effectively taking a snapshot of the positioning of the 5 atoms immediately upon ionization. An angle which uniquely defines the handedness of the enantiomer based on the momenta of the fluorine, chlorine and bromine atoms may be defined, given by the formula $\cos(\theta) = \vec{p_F} \cdot (\vec{p_{Cl}} \times \vec{p_{Br}})(|\vec{p_f}||\vec{p_{Cl}} \times \vec{p_{Br}}|)^{-1}$. The resulting measurement is shown in Figure 2.13; the negative values correspond to the S enantiomer, and the positive the R.

Indeed, a full reconstruction of each ion momentum may be shown, as in Figure 2.14. This picture is shown in the frame defined by the momentum of the carbon ion and the momentum sum of the bromine and chlorine ions, and is relative to the carbon atom. The left hand side shows the S enantiomer, and the right the R enantiomer.

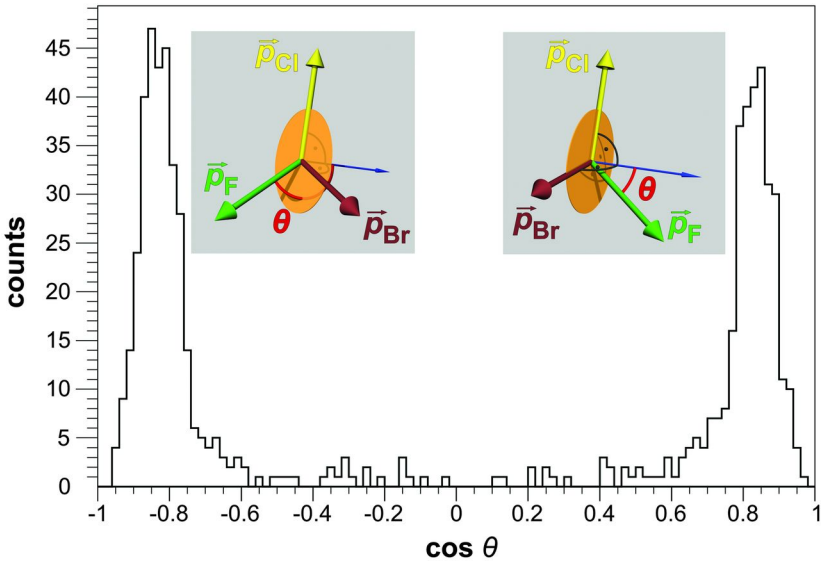

FIGURE 2.13: Histogram of the cosine of the chirality angle θ. The different enantiomers from the racemic mixture are clearly separated, with the S enantiomer at negative values and the R enantiomer at positive. Taken from [57].

Unfortunately, as pleasing as these results are, the same experiment generally cannot be performed using more complicated molecules. This is due to the experimental difficulty and analytical complexity of producing, detecting and identifying the ions/charged fragments from a complete Coulomb explosion in COLTRIMS.

2.3.2 Single Photon PECD

By visiting a facility such as a synchotron or free electron laser, one can generate coherent light with extreme intensity or photon energy. In doing so, one unlocks access to a new set of dynamics, such as single-photon ionization, or ionization of core electrons. These processes can prompt impressive PECD responses.

In 1976, Ritchie developed a novel theoretical analysis of a chiral phenomenon [58]. It was shown that the angular photoelectron cross section of single photon ionization of chiral molecules had an asymmetry depending on the handedness of light or molecule. If the handedness of the light or molecule was flipped, so did the sign of the asymmetry. This was the genesis of photoelectron circular dichroism.

Results showing this type of dichroism were first shown by Powis in 2000 [59], who simulated the ionization of lactic acid and glyceraldehyde. In order to analyze the results, Powis broke the angluar photoelectron distribution down into a sum of Legendre polynomials P_j, taking a second order approximation that for polarization p (circularly polarized light gives $p = \pm 1$ and linear $p = 0$), the angular distribution is given by:

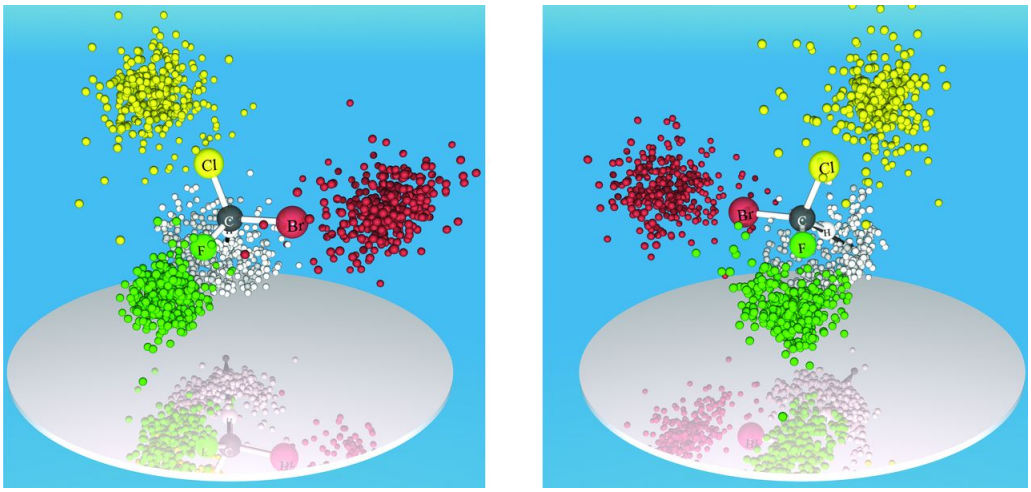

FIGURE 2.14: A full momentum reconstruction in the molecular frame defined by the momenta of the carbon ion and the sum of the bromine and chlorine ions. The S enantiomer is on the left, and the R enantiomer on the right. Taken from [57].

$$I_p(\theta) = [1 + b_1^p P_1(\cos\theta) + b_2^p P_2(\cos\theta)]\,, \tag{2.16}$$

where b_j^p represents the strength of each term. For circular dichroism in chiral molecules, we are thus interested in the $b_2^{\pm 1}$ coefficient, which corresponds to asymmetry due to circular polarization, and the $b_1^{\pm 1}$ term, which is only non-zero due to the chirality of the molecule. The coefficients for the ionization of the outermost valence orbitals of R-glyceraldehyde with left-handed light with varying electron energy are shown in Figure 2.15, where the HOMO is labelled 24, HOMO-1 is 23, and so on. The dashed line represents b_1^1 and the solid line b_2^1.

What may be gleaned from these results is that the b_1^1 term is higher at low electron energies, where interaction with the chiral molecular potential is more significant. When the electron energy increases, this term tends to 0 for all orbitals. The b_2^1 parameter shows opposite behaviour, where low electron energy yields a low coefficient, and approaches its limit of -1 at higher energies. While it is shown in these plots for only R-glyceraldehyde, it is worth noting that the b_1^1 term changes sign if either the handedness of the light or molecule changes, a hallmark of chiral observables. Breaking down the angular distribution of an observable into a decomposition of angular Legendre polynomials has since become a common analytical tool for PECD measurements.

The first such experiment (and indeed, the first PECD experiment) was performed by Böwering *et al* in 2001 [60]. They measured the forward-backward asymmetry of R- and S-bromocamphor by ionization using left- and right- handed circularly polarized light. A 16.2 eV photon energy was used, which allows for ionization from the HOMO, localized near the C-O double bond, or from an orbital localized at the Br atom. Two

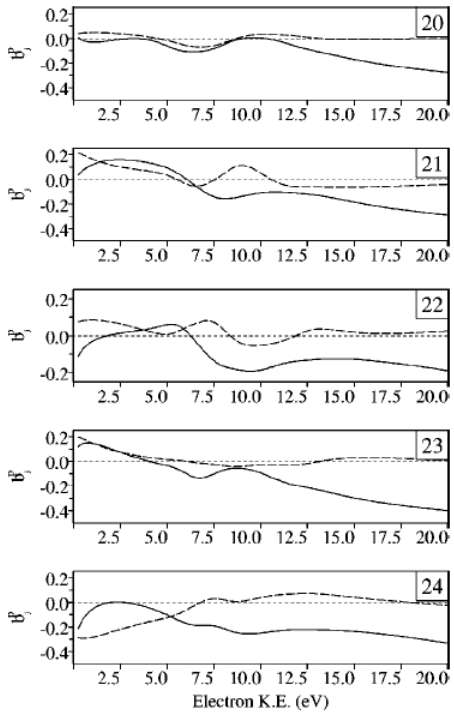

FIGURE 2.15: Photoelectron circular dichroism parameters b_2^1 (solid line) and b_1^1 (dashed line) for photoionization of the outermost valence orbitals of R-glyceraldehyde as electron energy varies. The HOMO is labelled 24, HOMO-1 is 23, and so on. Taken from [59].

electron detectors on a rotatable mount were placed at a 180° angle with respect to each other; measurements were performed at detector angles of 55°/125° and with both at 90°. Experimental results are shown in Figure 2.16.

The first panel shows a photoelectron spectrum as a function of binding energy, where the C-O and Br peaks are clearly visible. Asymmetry is shown in the second, where the σ^+ and σ^- refer to right- and left-handed polarized light respectively. The asymmetry is maximum at approximately 3% at the C-O peak, and opposite for different handedness, whereas the Br peak shows approximately zero asymmetry. The third panel shows the effect of varying detector position, indicating that 55° and 125° have equal but opposite forward-backward asymmetry, and both detectors at 90° yields no asymmetry, as is expected.

A more recent example is a large collaboration by Fehre *et al*, published in 2021 [61]. They used 550 eV photons to measure O 1s photoelectrons from propylene oxide in a COLTRIMS setup, with coincidence of the molecular fragmentation; if at least three fragments are measured, the molecular orientation in space can be determined, allowing theoretically for upwards of 100% PECD signal [62]. Using only data where the molecular orientation is clear, they compared the photoelectron emission distributions for S-propylene oxide under left- and right- handed circularly polarized light. The

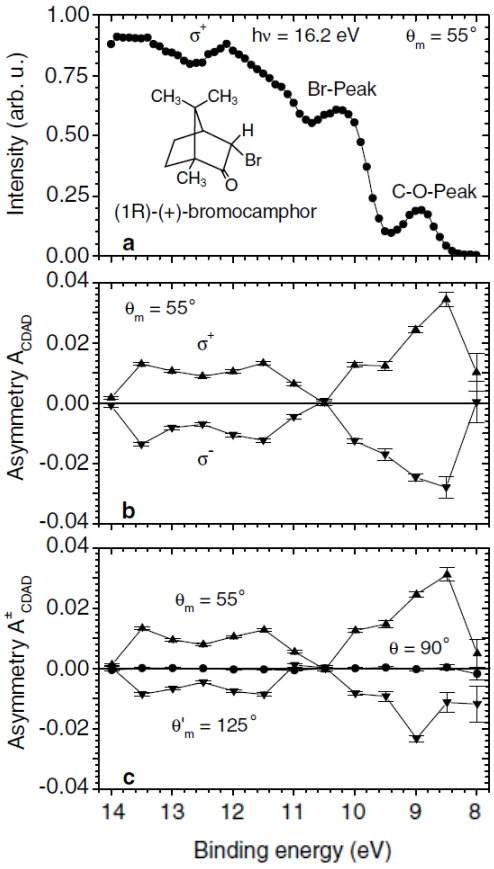

FIGURE 2.16: A photoelectron spectrum, (a), of R-bromocamphor from ionization by a right-handed circularly polarized 16.2 eV pulse. The C-O peak and Br peak are labelled. Panel (b) demonstrates the forward-backward asymmetry of right- and left-handed light, labelled σ^+ and σ^- respectively. The asymmetry of the detector pair at 55°/125° and with both at 90° is shown in (c). Taken from [60].

distribution from a single orientation is highlighted in Figure 2.17.

In this Figure, ϕ and θ represent the azimuthal and polar angles of photoelectron emission respectively. Shown in (a) and (e) are the experimental distributions from left- and right-handed circularly polarized light respectively, whereas (c) and (g) show the results of an *ab initio* calculation. Inset is the molecular orientation: (b),(d),(f) and (h) depict a three-dimensional visualization of the corresponding plots, with respect to the direction of propagation of light and molecular orientation. This method experimentally demonstrates a PECD signal of over 50%!

The two papers I have highlighted in this thesis are certainly not the only single photon PECD measurements that have been performed. I invite the reader to peruse some additional examples from the past two decades at their leisure [63–69].

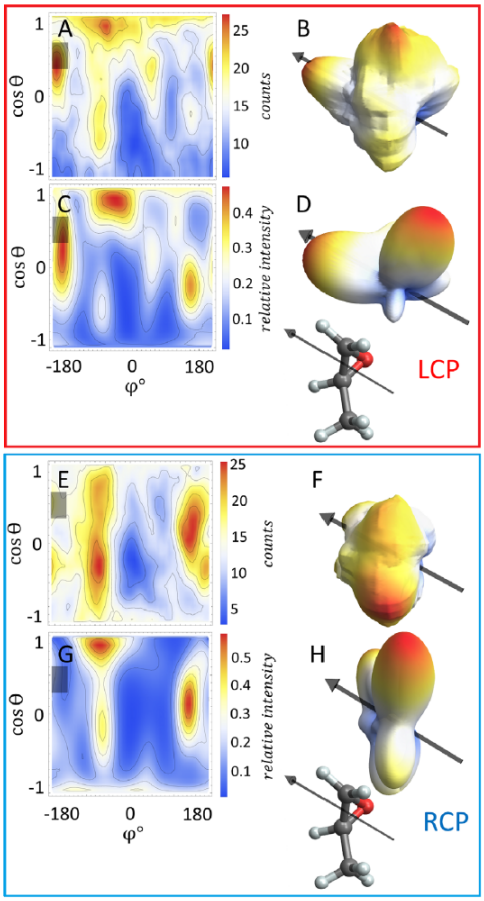

FIGURE 2.17: Experimental photoelectron distributions are shown in (a),(b),(e) and (f), whereas computed distributions are shown in (c),(d),(g) and (h). Data from left-handed polarized light is shown above, whereas right-handed below. The orientation of the molecule is inset. Taken from [61].

2.3.3 Multiphoton PECD

It is also possible to observe considerable PECD effects using multiphoton techniques. A nice experimental example using circularly polarized light was published by Lehmann *et al* in 2013 [70], when they studied the ionization of camphor. A velocity map imaging setup (VMI) was used to measure the 3D momentum spectrum of photoelectrons in coincidence with the parent ions. R- and S-camphor were ionized with left- and right-handed circularly polarized light, and the resulting scattering angle of the electrons with respect to the propagation of the light was measured, as shown in Figure 2.18.

In panels (a) and (b), we see that the angular distribution from left- and right-handed light is not equal. By breaking this down using a Legendre expansion, the sum of the odd terms show an oscillatory asymmetry in the difference between light handedness. The differing enantiomers show exactly opposite asymmetry, yielding a PECD value of

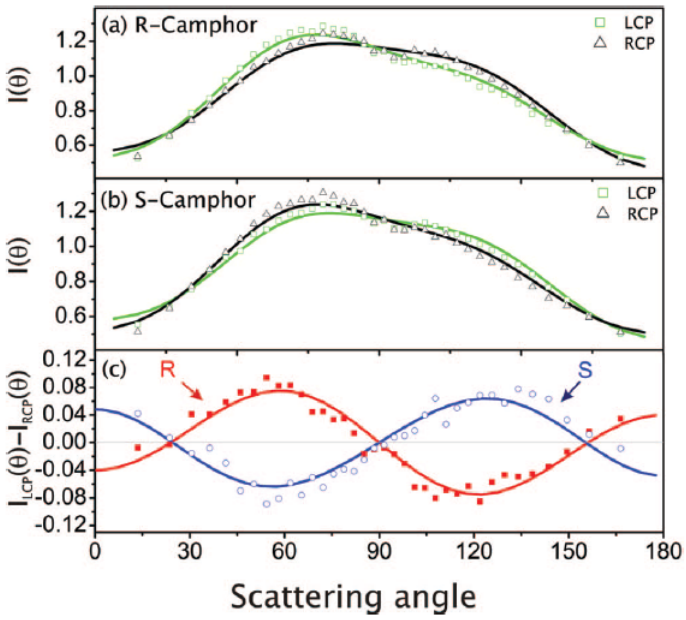

FIGURE 2.18: Photoelectron angular distribution from ionization of R- and S-camphor using left- and right-handed circularly polarized light shown in (a) and (b). Panel (c) isolates the chiral signal by Legendre expansion, comparing the distributions of differing handedness of light. Taken from [70].

almost 10%.

Another interesting method was developed in 2019 by Rozen *et al* [71]. Rather than employing circularly or elliptically polarized light, they thought to engineer a field whose instantaneous chirality can be controlled. This is the case for a combination of linear but orthogonal ω and 2ω pulses, whose relative phase changes the instantaneous chirality. Despite the net chirality being zero for such a field, the PECD response to all possible phase conditions was shown to be non-zero in a time-dependent Schrödinger equation simulation, due to the asymmetric ionization dynamics' interaction with the chiral potential of the molecule. Indeed, the experimental electron momenta from ionization of fenchone and camphor show the same up-down and forward-backward asymmetry discovered in the simulation, and are displayed in Figure 2.19.

A plot such as Figure 2.19 is typically obtained by directly comparing the handedness of pulse or molecule, whereas this field does not allow for this technique. Instead, the signal can be extracted by Fourier analysis of the data as the relative phase is changed. There are two modulations present: the first is at 4ω frequency and is due to the probability of ionization changing as the maximum field amplitude changes. By Fourier analyzing each pixel of the detector individually, a 2ω oscillation also appears, which is sensitive to the direction of rotation, and thus chiral sensitive. This is the signal shown in the plots, and gives a maximum overall PECD signal of 1%.

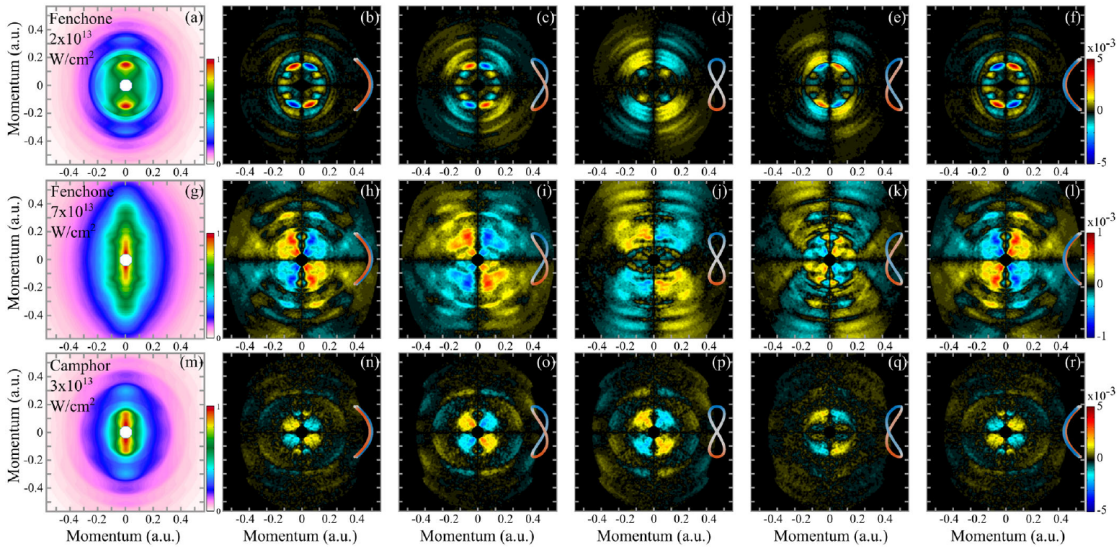

FIGURE 2.19: Electron momenta resulting from ionization of fenchone and camphor at varying intensity and relative ω-2ω phase. Taken from [71].

There is indeed a large body of other work using multiphoton processes to measure PECD. Some more examples that have similarly contributed to furthering the technique include [72–80].

2.3.4 Chirality in High Harmonic Generation

Elliptically and Circularly Polarized Schemes

An alternative method that has been proven to find optical differences between enantiomers is to probe them using high harmonic generation, whose fundamentals we have discussed in Section 2.2.2. This was first accomplished in 2015 by Cireasa *et al* [81].

In an achiral medium, using linearly polarized light is the most efficient method to generate high harmonics, as the greatest portion of the electronic wavepacket returns to the atom. As ellipticity is increased in the driving light, the wavepacket begins to drift further and further away, rapidly suppressing the yield of harmonics.

Cireasa *et al*, however, went on to show that this is not true in chiral molecules. The high harmonic yield as a function of ellipticity is not maximized for linearly polarized light. This is shown in Figure 2.20: a and b give the yield of each harmonic order as a function of ellipticity for the R- and S- enantiomer of chiral molecule propylene oxide, while c and d show the ellipticity that maximizes each harmonic for propylene oxide and fenchone respectively. Propylene oxide shows that a harmonic order of 41 is maximized at the highest value of ellipticity, while all harmonics of fenchone are maximized

at the same value of ellipticity, roughly 1-2%. The overall signal difference is on the order of 10%.

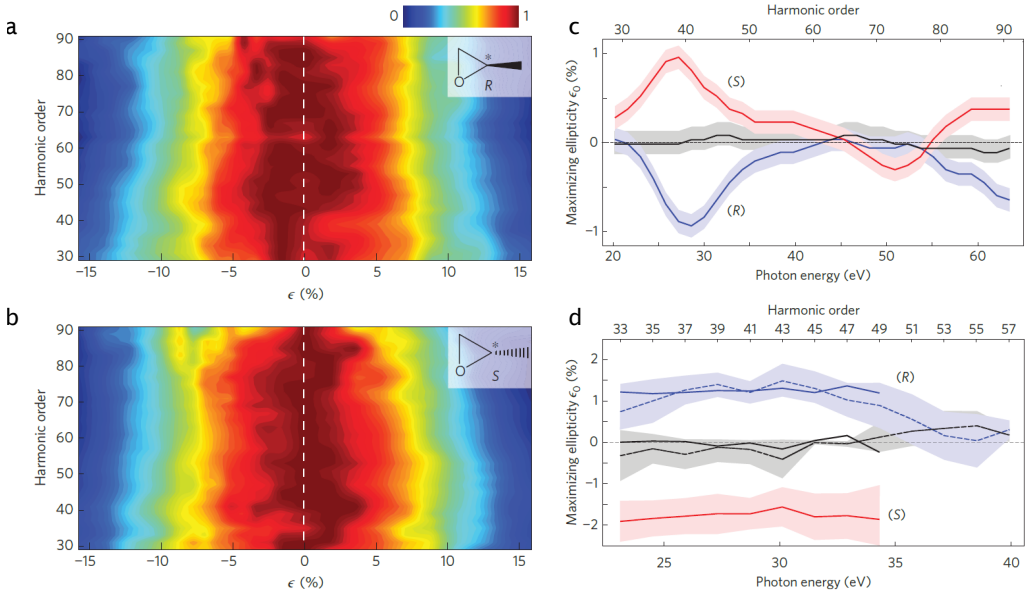

FIGURE 2.20: The high harmonic yield as a function of laser ellipticity for R- and S- propylene oxide is shown in (a) and (b) respectively. The ellipticity that maximizes this yield for each enantiomer of propylene oxide and fenchone is then exhibited in (c) and (d). Taken and adapted from [81].

The difference in harmonic efficiency demonstrated between enantiomers is due to magnetic field effects; Cireasa *et al* propose two different mechanisms. The first is that the Lorentz force acts on the electron during its trajectory, causing the motion to become chiral. The second explanation is that the magnetic field acts on the parent ion, and induces chiral sensitive transitions between states. The differing electronic structure of propylene oxide and fenchone explains their varied response in maximizing ellipticity of each harmonic.

A follow-up to this method was performed in 2018 by Harada *et al* [82], using circularly polarized high harmonic generation. In short, the fields that generate such harmonics are composed of two counter-rotating circularly polarized pulses at frequencies ω and 2ω, resulting in an overall field shaped like a trillium (see [83] ,for example, for more details). The symmetry in this situation is such that $3m$-order harmonics are suppressed, whereas $3m+1$ and $3m+2$-order harmonics are generated with the same handedness as ω and 2ω respectively.

Harada *et al* generated harmonics from S- and R-limonene, and measured the spectra by transferring the photon energy into photoelectrons in a krypton magnetic bottle spectrometer. Each harmonic then results in two peaks because of the spin-orbit splitting of the $^2P_{3/2}$ and $^2P_{1/2}$ states on the krypton ion. Additionally, harmonics from helium

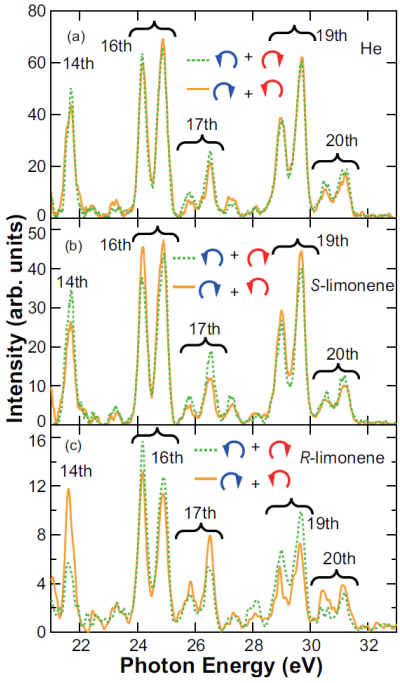

FIGURE 2.21: Circularly polarized harmonic spectrum of helium and S- and R-limonene generated by a counter-rotating two-colour field. Green and orange lines correspond to opposite handedness of driving field. Taken from [82].

were generated for comparison. The results of this measurement can be seen in Figure 2.21. The helium results show very little difference between harmonic intensity for opposite handedness, whereas dichroism can be seen in limonene. The 16th harmonic has lower yield for S-limonene in the green curve than the orange curve (corresponding to one handedness vs another), and the opposite behaviour is seen in the 17th harmonic. This pattern is reversed for R-limonene. This is consistent with S-limonene preferring to generate counterclockwise harmonics, whereas R-limonene clockwise.

Other such examples of high harmonics being used to evaluate circular dichroism include [84–86].

Synthetic Chirality

As seen in the previous sections, it is difficult for most optical methods of experimentation to distinguish between chiral enantiomers with great efficiency. This concept, however, has recently been challenged by a determined core of theorists, whose ideas revolve around novel pulse combinations which are synthetically chiral. This section will review some of these schemes, with particular attention paid to Ayuso *et al*'s 2019 paper [87], which is the inspiration for the experiment in this thesis.

Despite the successes of the previously listed literature, we note that circularly polarized light is actually a very poor chiral reagent. All optical interactions with the target take place under the dipole approximation, i.e. that the wavelength of the light is much larger in magnitude than the scale of the target itself. As such, any chiral interaction is due to the electric quadrupole or magnetic dipole terms, which are orders of magnitude lower than an electric dipole effect. This results in the relatively small overall difference in signal observed in most circular dichroism experiments. It is for this reason that Ayuso *et al* propose a novel pulse scheme which forgoes using circularly polarized light. The designed field traces a 3D, handed curve in time at all points in space, meaning that it is "locally" chiral on the scale of a molecule, and indeed the interaction will yield electric dipole effects.

The recipe to constructing such a field is in the combination of four pulses: two beams propagating in a non-collinear fashion, with each beam consisting of an ω and 2ω field, polarized orthogonally. In this system, the handedness of the field is controlled by the relative phase between ω and 2ω in each beam. When the two beams overlap, they form an interference grating in both ellipticity and field in z, which is the key to managing the system experimentally, ensuring the handedness is constant throughout all space. A practical prescription to generating this field setup is shown in Figure 2.22. In short, an 800 nm pulse propagates through a β-barium borate crystal to generate 400 nm light. Calcite, a birefringent material, is used to manage the dispersion in the system, and a thin rotatable fused silica window controls the relative phase in the orthogonal two-colour (OTC) pulse. The beams propagate in parallel, and are focused by a 5 cm focusing mirror, creating a 5° angle from the propagation axis. This will be described in considerably more detail in Chapter 3.

Specifically, the vectorial electric field in the focus is given by the equation

$$\vec{E}_0(x,y,z,t) = \begin{bmatrix} \big(\sin(\alpha)\sin(k\sin(\alpha)x + \delta_-^{\omega})\big)\cos(k\cos(\alpha)y - \omega t - \delta_+^{\omega}) \\ \big(\cos(\alpha)\cos(k\sin(\alpha)x + \delta_-^{\omega})\big)\cos(k\cos(\alpha)y - \omega t - \delta_+^{\omega}) \\ A\big(\cos(2k\sin(\alpha)x + 2\delta_-^{2\omega})\big)\cos(2k\cos(\alpha)y - 2\omega t - 2\delta_+^{2\omega}) \end{bmatrix}, \quad (2.17)$$

where α is the angle between the propagation vectors of the OTC pulses, A is the relative amplitude of the 2ω compared to ω, and $\delta_{\pm}^{m\omega}$ is given by

$$\delta_{\pm}^{m\omega} = \frac{\phi_2^{m\omega} \pm \phi_1^{m\omega}}{2}, \quad (2.18)$$

with ϕ referring to the phase of the pulse in OTC beam 1 or 2 and with $m\omega$ frequency. A Gaussian envelope for the field is applied when focused in space, as demonstrated in

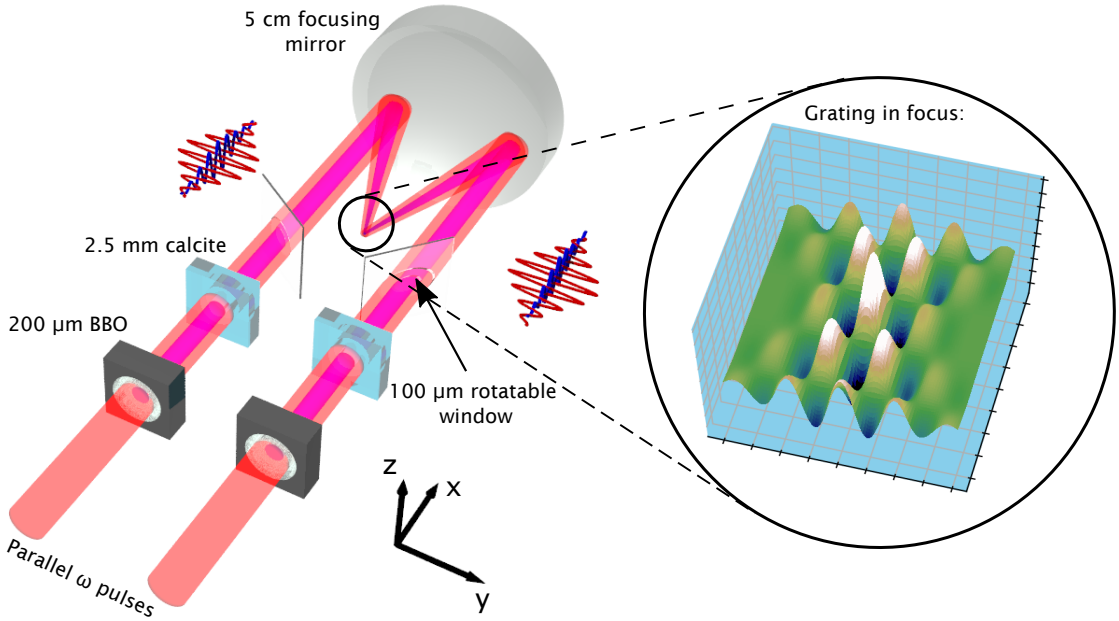

FIGURE 2.22: A schematic image that represents the overall pulse scheme in the experiment. Two 800 nm ω fields propagate in parallel, and generate 400 nm 2ω when passed through 200 μm β-barium borate. Dispersion between the pulses is controlled with 2.5 mm of calcite, and a 100 μm rotatable fused silica window chooses the relative phase in each arm. The beams are focused by a 5 cm focusing mirror, causing an interference grating when interfering at the focus.

Equation 4.1, and in time, giving the pulse a temporal shape, with a full-width at half maximum τ:

$$E(x,y,z,t) = E_0(x,y,z,t)\exp^{(\frac{t}{\tau})^2} \tag{2.19}$$

To control the handedness of the field across space in the focus, the phase of each constituent pulse must be chosen with precision. The condition for the handedness to remain constant is

$$\phi_1^{\omega-2\omega} - \phi_2^{\omega-2\omega} = (2n+1)\pi, n \in \mathbb{Z}\,, \tag{2.20}$$

where we define $\phi_{1,2}^{\omega-2\omega}$ as the relative phase difference between pulses in OTC beam 1 or 2. Three cases are highlighted in Figure 2.23, where the relative phases $\phi_{1,2}^{\omega-2\omega}$ are shown, as well as the interference gratings that are generated across the focus (in y) by such a pulse; black shows the ellipticity grating, while blue shows the z-field grating. The sign of each grating is shown as a $+$ or $-$ inset in the plot, and the red and green lines show where the signs flip. A schematic of each OTC field oscillating as it propagates is also shown.

Case 1 and Case 2 both satisfy Equation 2.20, and for each of these cases, we see that the ellipticity grating and z-field grating change sign at the same point in space. The field changes handedness when either flips sign, thus we see that the overall chirality is preserved across the focus. The nature of the chirality for each of these two cases is opposite in handedness. Case 3 does not satisfy 2.20, and we see that the ellipticity grating and z-field grating change sign out of phase. This causes the chirality to flip handedness every time either grating changes sign, and when perfectly out of phase, will be equal between left and right. We call these cases "globally chiral" and "globally achiral" respectively.

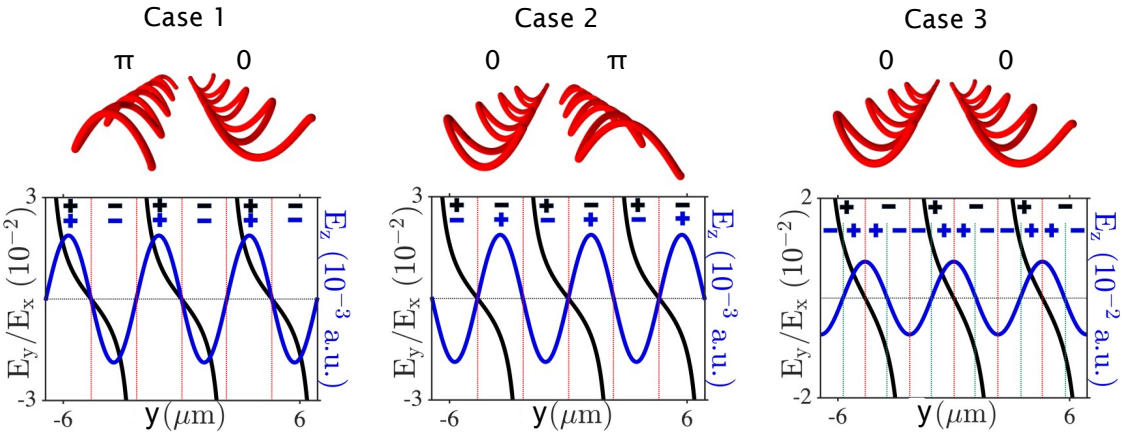

FIGURE 2.23: Three cases are presented with labelled phases and a schematic showing the OTC fields. The ellipticity grating and the z-field grating are plotted across the focus for each case, and the points where they change sign are marked by red and green lines. The sign of each grating is inset. Cases 1 and 2 are "globally chiral" and case 3 is "globally achiral".

Ayuso *et al* went on to use this field structure to computationally generate harmonic spectra from randomly oriented S- and R-propylene oxide, using a wavelength of 1.77 um, α of 5°, A at 0.1, and a globally chiral phase condition. In this scheme, the odd harmonics are polarized in the y-direction, and the even harmonics in the z-direction. The near-field results of this simulation are shown in Figure 2.24, where the intensity of varying harmonic numbers (with odd in blue, and even in red) are shown related to the position across the focus.

The S-propylene oxide spectrum shows little variation with respect to harmonic number, whereas in the R- spectrum, it is clear that the even harmonics disappear entirely at specific harmonic orders. There is no change to intensity across the focus. The suppression of even harmonics can be attributed to the imprinting of the chirality of the light onto the electron trajectory. Recombination with the chiral parent ion is enatiosensitive, and related to the 3D structure of the trajectory. These results show the maximum possible dichroism signal, 200%! Indeed, the harmonic order that demonstrates

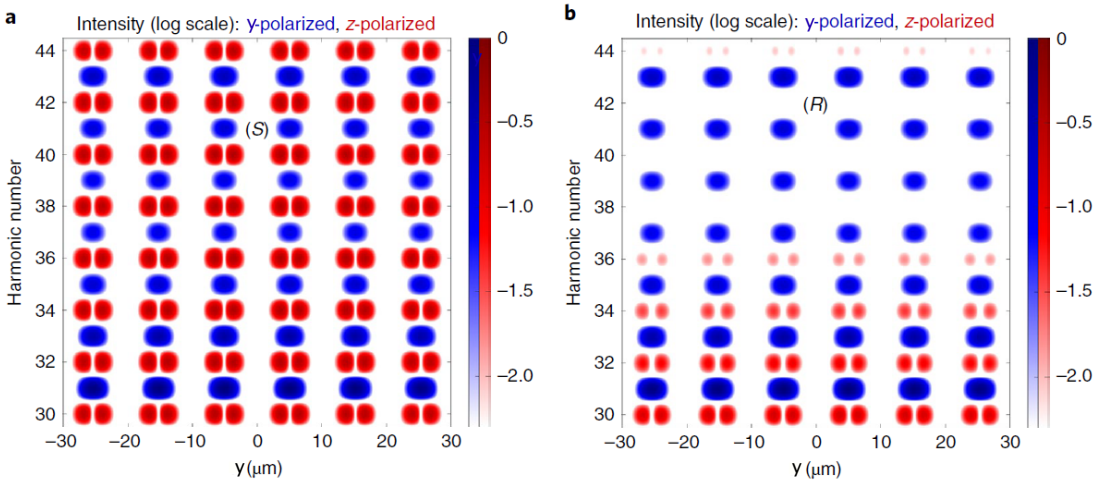

FIGURE 2.24: Near-field results of computational generation of high harmonics from S-propylene oxide, shown in (a), and R-propylene oxide, shown in (b). Odd harmonics are shown in blue, and polarized in the y-direction, whereas red harmonics are shown in red and polarized in the z-direction. Taken and adapted from [87].

this result can be tuned by varying the parameters of the simulation.

While Ayuso *et al* demonstrate striking results in the harmonic spectra, this thesis will instead seek to probe information gathered from photoelectrons in a COLTRIMS apparatus. Photoelectron spectroscopy is complementary to the picture shown by HHG. Recall the three-step model discussed in Section 2.2.2: ionization, propagation, recombination. Photoelectron spectroscopy may yield isolated insight into the effects due to the chiral field in the propagation step by looking at ionization of an achiral target. Furthermore, the contribution a chiral molecular potential on the ionization step may be probed by using a chiral target.

Indeed, it is worth noting that the body of work discussing chiral interaction from purely electric dipole effects is rapidly growing. These ideas would be well worth a look by budding experimentalists looking for thesis topics. The following publications are further illustrations of synthetically chiral schemes.

An idea proposed by Ayuso *et al* in 2021 [88] is reasonably simple in execution, enabled solely by the use of a single linearly polarized, intense and few-cycle pulse. The principle is that when tightly focused, with a beam waste on the order of 5 μm or less, the beam acquires a strong longitudinal component due to the tilt of the wavefront, and hence ellipticity in the propagation direction. This can be seen in (a) in Figure 2.25. The handedness of ellipticity is flipped on opposite sides of the beam axis because of the opposing signs of the longitudinal component, as demonstrated in (b).

Harmonics are then generated from a thin gas jet. For an isotropic molecule, harmonics would only be emitted in the polarization direction, but if the chosen molecule

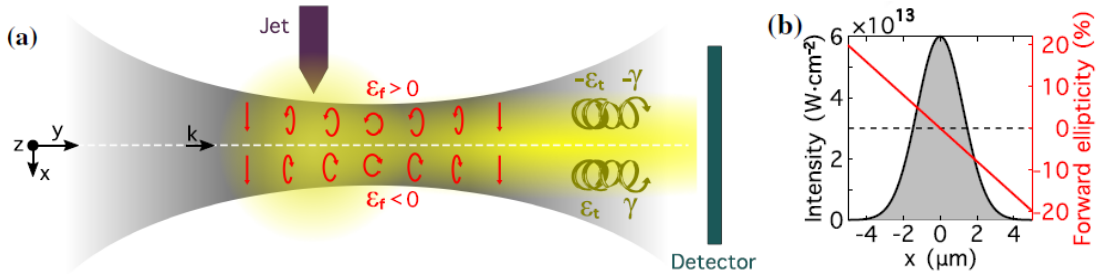

FIGURE 2.25: Forward ellipticity acquired by a tightly focused along the propagation direction, shown in (a). Panel (b) shows the intensity and ellipticity profile of the pulse transverse to the propagation direction. Taken and adapted from [88].

is chiral, harmonics will be emitted in both the x- and z-direction due to symmetry breaking of the molecule; the phase is opposite for media of opposite handedness, and thus so is emission in the z-direction. Ayuso *et al* calculate the harmonic spectra from L- and R-propylene oxide using time-dependent density functional theory, and the results are presented in Figure 2.26.

While the odd harmonics are brighter for this simulation, we see that in panels (b) and (c), it is the even harmonics which provide enantiosensitivity due to the symmetry breaking of the chiral molecules. The harmonic ellipticity is opposite in handedness for the L- and R- enantiomers. The polarization of the harmonics is also opposite, as seen

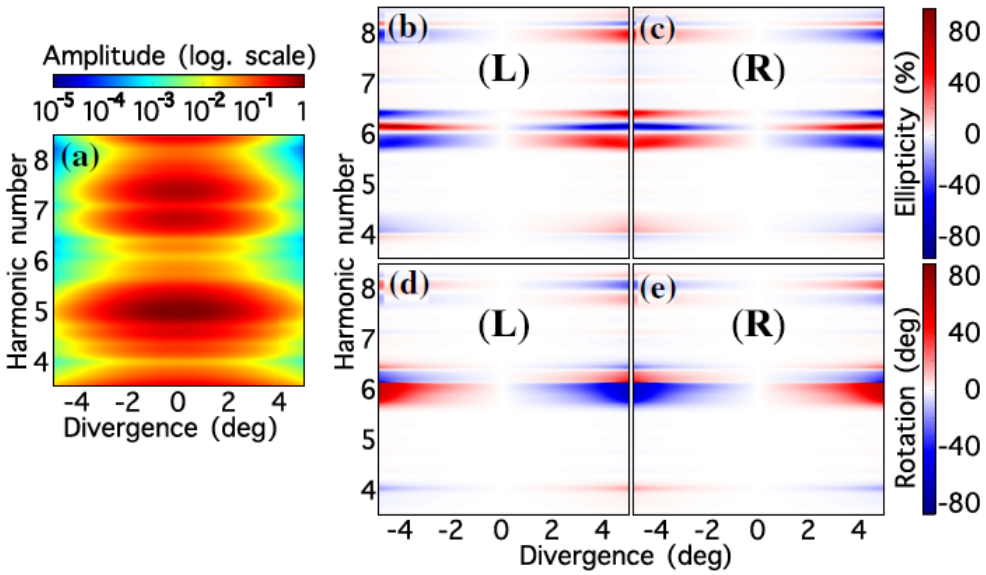

FIGURE 2.26: Presented in (a) is the overall intensity of the harmonic spectrum as divergence increases. Panels (b) and (c) show the ellipticity of the harmonics for left- and right handed molecules respectively, and (d) and (e) the rotation of polarization of the harmonics. Taken from [88].

in (d) and (e). These signals can again yield a maximal dichroism value of up to 200%. As the driving pulse is only a few cycles in time, Ayuso *et al* also show that there is a significant dependence on carrier envelope phase, which can be tuned to adjust the phase of the harmonics.

Yet another idea proposed by Ayuso *et al* in 2021 [89] is a creative take on Young's double slit experiment. The concept is outlined in Figure 2.27. If we place two chiral emitters with opposite handedness near each other, the emission can be broken into achiral (even) and enantiosensitive (odd) components, shown in (a). The total interference, due to the separation of the emitters, then shows a shift to either the right or left, based on the ordering of the molecules.

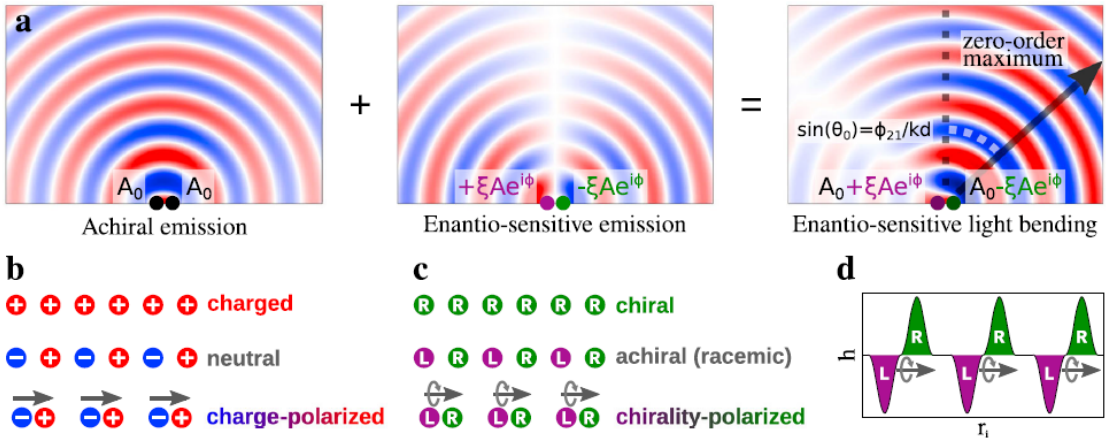

FIGURE 2.27: The interference pattern of a chiral emitters separated by a distance, broken into achiral and enantiosensitive emission. Panels (b),(c) and (d) demonstrate the of "polarization of chirality". Taken and adapted from [89].

They name this effect "polarization of chirality", and demonstrate an example in (b) and (c). Consider a row of alternating point charges. The system is neutral, but if they are placed such that the distribution is not uniform, a polarization develops, creating dipoles. The same idea holds with a distribution of chiral emitters. Equally distributed, the mixture is racemic, but when the positions are shifted, "dipoles of chirality" are created, giving the medium a "polarization of chirality".

In order to create such a distribution of chiral emitters, Aysuo *et al* propose using structured locally chiral light, taking advantage of the same scheme developed in [87] with a particular phase choice. They then quantify the interaction of this chirality-polarized field by calculating harmonic generation from a chiral medium. The results are shown in Figure 2.28.

Seen in plot (a), it is clear that the emission of harmonic 12 is bent away from normal, maximized around 1°, and that the angle of emission is opposite for different handed enantiomers. Indeed, we see that the in panel (b), the dichroism value peaks around

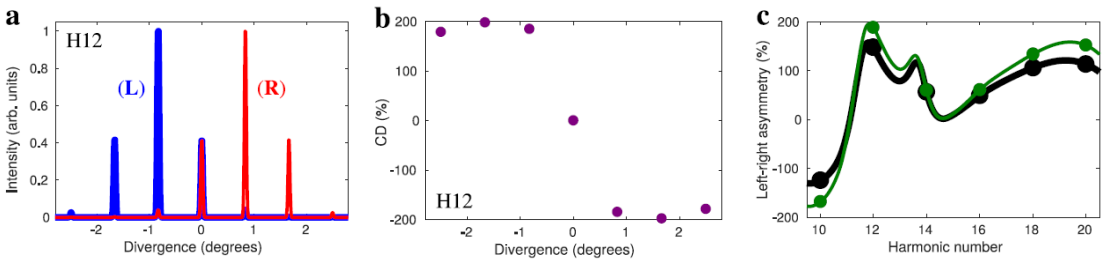

FIGURE 2.28: Harmonic generation from molecules in a "polarization of chirality" field. Shown in (a) is the divergence from normal of the twelfth harmonic, and (b) the dichroism value for each peak. Panel (c) gives the asymmetry value for even harmonics, where the black line takes the 0 divergence peak into account, and the green doesn't. Taken and adapted from [89].

the maximum, 200%. All even harmonics show at least some degree of asymmetry, as demonstrated in (c), where the green points don't include the central emission peak, and the black ones do.

Chapter 3

Experimental Technique

"Not much is known about alligators. They don't train well. And they're unwieldy and rowdy to work with in laboratories."

Diane Ackerman

This Chapter will focus on the experimental methods and techniques needed to run a novel synthetically chiral ultrafast experiment in a COLTRIMS machine. First, an overview of the laser system used in JASLab2 will be given. Then a detailed explanation of COLTRIMS will be provided. Finally, the optical setup and techniques used to generate a synthetically chiral pulse will be discussed. All experimental work detailed in Chapter 3 was performed by me.

3.1 Laser System

The laser used to perform the novel chiral experiments reported on in this thesis was a commercially built Coherent Legend system which outputs laser pulses centred at a wavelength of 800 nm, of approximately 25 fs duration, at a repetition rate of 10 KHz and pulse energy 1.5 mJ. It is seeded by a Coherent Micra Titanium:Sapphire oscillator which is then amplified in two stages. The first stage, Coherent Duo, employs both a regenerative amplifier and a single pass amplifier, while the second, Coherent Cryo, is a single pass amplifier where the crystal is both under vacuum and cooled cryogenically to 80K to avoid overheating.

After the output of the second stage is a beam splitter, which sends 20% of the power to the COLTRIMS system. This power is more than sufficient to perform measurements. The remaining 80% of the laser power goes into an optical parametric amplifier (OPA). If desired, the OPA can convert the frequency of the beam to a broad infrared range, in this case from approximately 2-4 μm with varying efficiency. The OPA is not used in the chiral experiment discussed in this thesis, but has been employed in previous COLTRIMS

works in our lab such as [90]. The beam then has several bounces on chirped mirrors, which are mirrors with dielectric coatings designed to reflect different wavelengths of light at different depths. These mirrors help to compensate for group delay dispersion, which causes the pulse to broaden in time as it propagates through the lab. The beam is then focused into a hollow core fibre, which is used as a spatial filter, removing undesirable inhomogeneities from the beam's spatial profile. Upon its exit from the fibre, the beam is then directed into the specific optical setup for this experiment. Figure 3.1 shows a diagram of the laser system and the general optical elements included after.

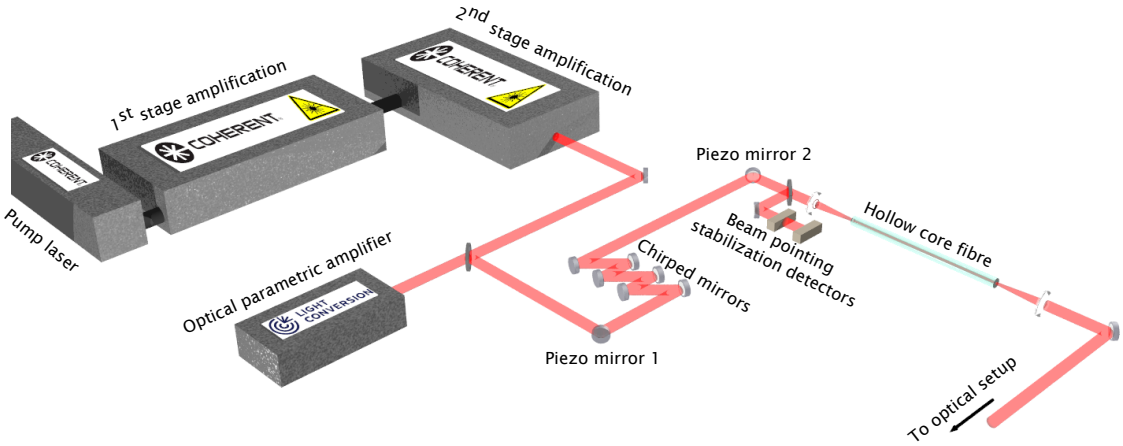

FIGURE 3.1: An approximately to scale schematic of the JASLab2 laser system. 800 nm centred light with a repition rate of 10 KHz, pulse energy of 1.5 mJ, and 25 fs duration is generated by a commercial Coherent Legend system. Of the output light, 20% is sent down-line to the COLTRIMS apparatus. The beam has several bounces on chirped mirrors, before being spatially filtered by a hollow core fibre.

The hollow core fibre requires very precise coupling alignment in order to have an acceptable output mode and power. Over the course of several days while a COLTRIMS experiment accumulates data, the everyday temperature and humidity fluctuations in the lab, and thus laser system, can cause enough of a pointing difference to disrupt this precise alignment. For this purpose, a pointing stabilization system and software are used to perform live corrections as the beam drifts. A small portion of the beam is sent to two stabilization detectors which measure both position and direction at two different locations in the beam path. When the beam is aligned properly with the hollow core fibre, the software is zeroed. As the beam drifts, the software detects that the pointing moves away from the zeroed alignment, and will adjust two mirrors setup earlier in the beam line that are equipped with piezo actuators. The system uses a learning algorithm to calibrate a 4x4 matrix in order to decide the necessary corrections. Figure 3.2 shows an example of the beam stabilization software.

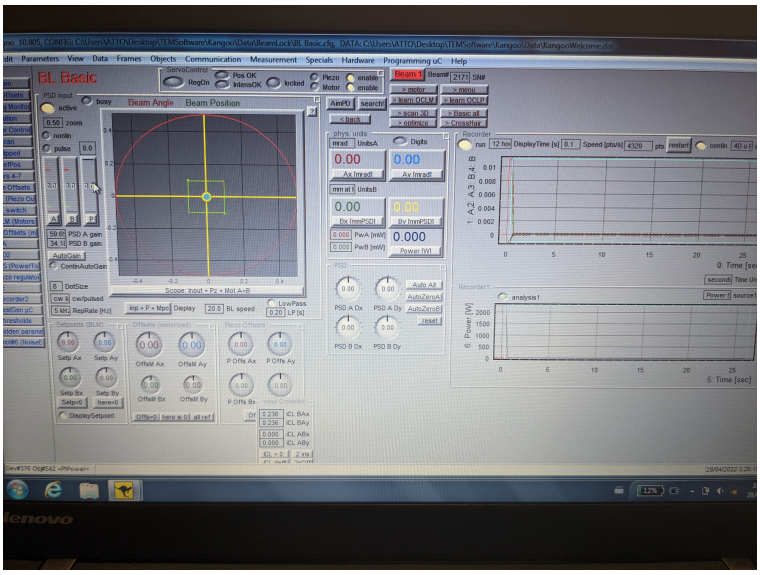

FIGURE 3.2: The 4D beam pointing stabilization software interface. The beam is stable when the circles in the top-left plot are centred on zero.

3.2 COLTRIMS

COLTRIMS stands for COLd Target Recoil Ion Momentum Spectroscopy, and is used to perform fully three-dimensional momentum measurements on ionization events. The electron(s) and ion(s) from such an event are detected in coincidence, so it is possible to completely map the momentum in a given process. A cartoon diagram of a COLTRIMS machine is shown in Figure 3.3.

Compressed gas from a cylinder expands through a 10 μm nozzle into a vacuum of 1×10^{-4} mbar with a stagnation pressure of 0.1-0.5 bar. The supersonic expansion of the gas cools the molecules and atoms down, and a skimmer of 0.3 mm is used to select the coldest part of the expansion. The jet then passes through a collimation chamber, further narrowing the jet with a 1 mm aperture and 350 μm piezoelectric slit. Next, the jet flies into the main COLTRIMS chamber, where it is ionized by an incoming short pulse, which is back-focused by a 5 cm parabolic mirror (the non-zero angle of reflection in Figure 3.3 is for illustrative purposes only). The remainder of the jet is finally pumped out in a jet dump.

The main chamber contains a stack of 11 cm square copper plates of 0.5 mm thickness, over which a constant voltage is applied. The plates are connected to one another through 100 kΩ resistors. The resulting electric field of about 10 V/cm accelerates charged particles, with ions and electrons travelling in opposite directions; the acceleration of the charged particles varies based on their mass, and thus this system acts as a spectrometer. Microchannel plates (MCPs) are placed at the top and bottom of the spectrometer, amplifying incident electrons and ions to macroscopic currents which can

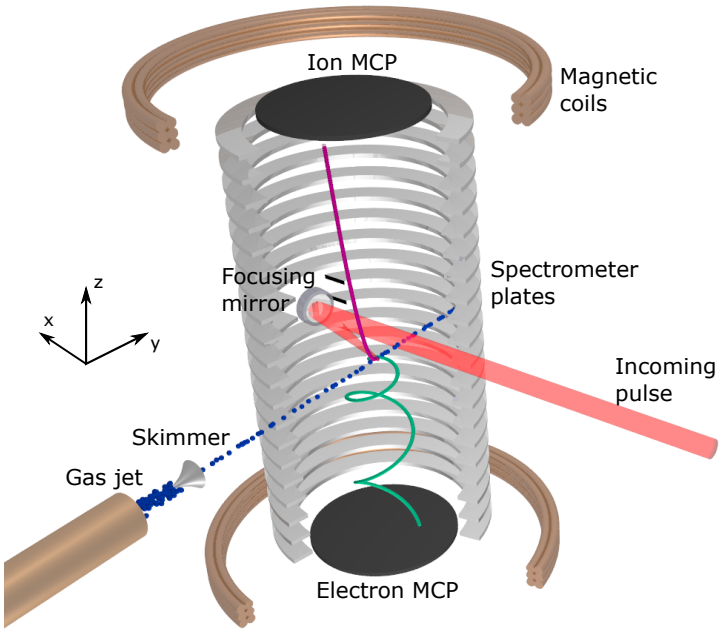

FIGURE 3.3: A schematic diagram of a COLTRIMS machine. Incoming light is focused onto a cold gas jet, causing ionization. Many spectrometer plates have a constant electric field placed over them, accelerating the electrons and ions towards michrochannel plates where their position is detected. Magnetic coils increase resolution of the electron detection by causing them to rotate on their trajectory.

be measured by delayline anodes underneath, detecting the position and timing of incident charged particles. A set of Helmholtz coils, with fifteen windings of copper wire housed outside the chamber with a diameter of 1.95 m have a current of approximately 85 A run through them, with a voltage of 7.5 V, creating a uniform magnetic field along the spectrometer direction of about 12 Gauss. This magnetic field is sufficient to cause the electrons to rotate along their trajectory, confining them in their x- and y-travel to be detected by the MCP, while the ions remain largely unaffected due to their much larger mass. For our setup, the maximum current setting is 200 A, yielding a magnetic field of approximately 28 Gauss. Figure 3.4 shows an in-depth view of COLTRIMS' design schematics.

A COLTRIMS machine is a very flexible instrument, and may be adapted to suit the purposes of the user, but at a significant cost of time and money. For example, it may be changed such that high harmonic light sources are used instead of a laser by adding additional differential pumping to avoid absorption of the high photon energy in air, as well as a spectrometer to measure the harmonic frequencies. A second example would be a system designed to observe high energy target particles, which would require higher electric fields in its spectrometer and larger MCPs to increase detection

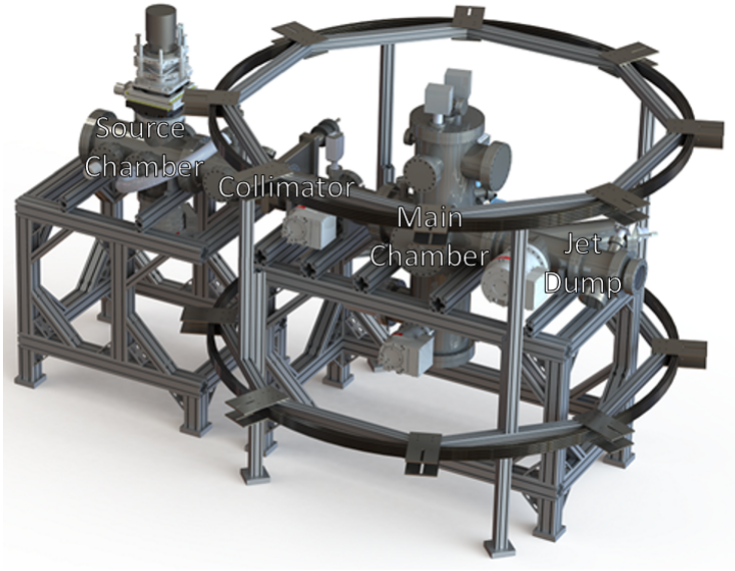

FIGURE 3.4: An in-depth and to-scale view of COLTRIMS. There are three main components to the COLTRIMS: the source chamber, which houses the jet apparatus, the collimator, in which the jet is reduced in temperature, and the main chamber, where the jet interacts with the laser and in which the detection equipment is placed. The remainder of the jet is pumped out in a jet dump.

efficiency.

3.2.1 Vacuum

When focused, the resulting electric field from the ultrashort laser pulse is strong enough to ionize just about anything in the focal volume. As such, it is extremely important for the pressure in the COLTRIMS main chamber to be as low as possible in order to distinguish ionization from the background versus that of the target in the jet. Under ideal conditions, the chamber can be pumped down to pressures on the order of 10^{-11} mbar, using several stages of pumping.

The first line of attack is a rotary vane roughing pump. The pump is divided into several chambers by blades, and the rotor is mounted eccentrically. As the vane rotates, the pump chambers alternatively increase in volume, causing suction from the COLTRIMS, then compress and expel the gas into the pump's outlet. When the pressure reaches 10^{-3} mbar, the turbo-molecular pumps are switched on. These pumps use spinning blades to knock ambient molecules into a pumping line. There are five such pumps on the COLTRIMS apparatus, two on the source chamber rating 200 and 500 L/s, one on the collimator at 200 L/s, and two on the main chamber at 200 and 500 L/s. These pumps can bring the chamber down to the order of 10^{-7} mbar in approximately one day.

If the pumps have not been running for some time, it is usually recommended to bake the COLTRIMS once the pumping systems are active again. Several heating pads are placed on the outside of the chamber, raising the temperature to about 80° C. The COLTRIMS is perennially coated in aluminum foil in order to provide insulation for this procedure. The heating of the chamber surface causes outgassing of particles on the internal walls of the system, decreasing the overall pressure. The chamber is usually baked for two to three days.

Passive pressure reducing techniques are the last step to relatively background-free measurements; the COLTRIMS main chamber uses a cryogenic pump. A solid mass of copper is connected to a helium compression system, which reduces the temperature of the mass down to as low as 20K. Incident gases are then frozen to the pump, removing them from the background of the chamber. Between this passive method and baking the COLTRIMS, the pressure drops down to the high 10^{-11} mbar range.

Finally, if desired, the COLTRIMS is equipped with a titanium sublimation pump. While this wasn't needed for the experiments detailed in this thesis, it is thusly possible to further reduce the pressure of the chamber. The system works by using a filament at high current and temperature to sublimate titanium, creating a thin coating on the walls of the chamber. This layer will adsorb residual gases, creating a solid product. The down side of using this pump is that its efficacy is reduced over time after sublimation as impurities are adsorbed.

3.2.2 Gas Jet

The thermal energy of free gas molecules is given as:

$$KE_t = \frac{3k_BT}{2}\,, \tag{3.1}$$

where k_B is Boltzmann's constant and T is the temperature. It follows that

$$\begin{aligned} \frac{mv_t^2}{2} &= \frac{3k_BT}{2}\,, \\ p_t &= \sqrt{3k_BTm}\,, \end{aligned} \tag{3.2}$$

with the thermal momentum p_t and the mass of the molecule m. As an example, this means in a room temperature setting, argon gas has an average thermal kinetic energy of approximately 38.7 meV, and 14.4 a.u. of momentum. A distribution spread of this magnitude would make measuring any small changes in ionic or electronic momentum completely unfeasible, so the thermal energy of any gas target must be managed.

One method to control this is via the use of a gas jet, which is a particularly convenient way to deliver the target anyway. When a gas under pressure is emitted through a thin nozzle into vacuum, it undergoes supersonic expansion, which has a structure

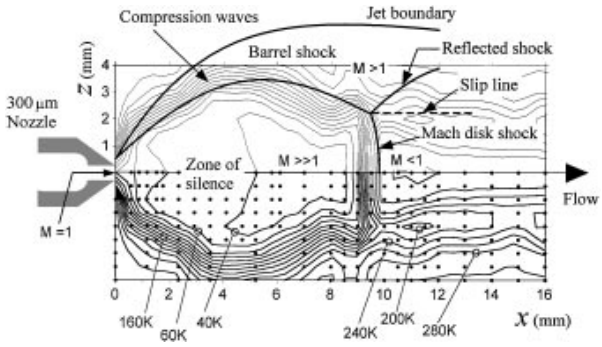

FIGURE 3.5: Raman mapping of isothermal lines from a gas jet. Molecules in the zone of silence have very low thermal kinetic energy. Taken from [91].

displayed in Figure 3.5 [91]. In short, there is a so-called zone of silence where the molecules are highly directed, with narrow velocity distributions and little rotation. This is filtered from thermally warmer regions via the use of a skimmer.

The COLTRIMS jet apparatus, designed by the author and shown in Figure 3.6, consists of a large copper arm attached to a coldfinger, which uses the same helium compressor as the cryogenic pump. The temperature is controlled by balancing the effect of the helium compressor with a heater attached to the copper arm, and is usually set to 100K in order to cool down the gas jet as a secondary means of reducing thermal momentum. If the temperature of the copper housing drops too low, the gas can freeze to the nozzle, ending any experimental usage until it is reheated. The gas' source is a pressurized Ar cylinder, set to 30 PSI for this experiment, and is forced through a 10 μm nozzle.

The whole jet mechanism is mounted on an XYZ translation stage, as seen in Figure 3.7. The three dimensional movement is necessary to maximize the signal, to "find the jet" so to speak. It is a challenge to align the system such that the gas output both travels through the skimmer and is seen by the focused laser pulse. If this position is not known, it typically involves several hours of work scanning through position space looking for the increased ionization that is a signal of the laser interacting with the gas jet. This alignment is sensitive to changes on the order of $\pm$ 100 μm. Additionally, as we have seen in Figure 3.6, the jet housing is rotatable, which changes the pointing of the molecular beam. This adds flexibility from a design standpoint, but required further trial and error to maximize the jet signal. A helpful tactic was to remove the jet from the chamber and drop methanol into the stream, causing it to become visible in short bursts and allowing us to determine if the nozzle was causing an angular offset in pointing.

The target in our chiral experiment is propylene oxide, which is a liquid at room temperature. This presents a difficulty for COLTRIMS, as liquid jets tend to either break

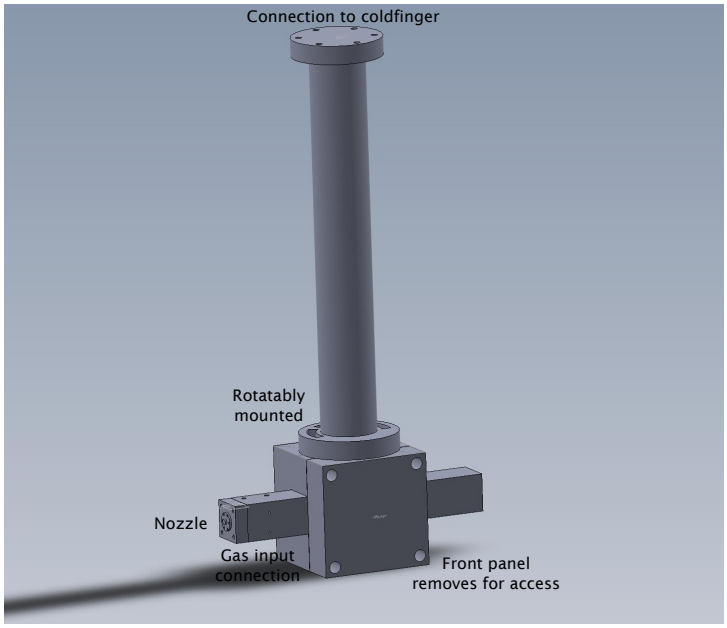

FIGURE 3.6: The jet apparatus in the COLTRIMS system, designed by me. A long coldfinger holds a rotationally adjustable housing for the jet. The front panel is removable for ease of access, and the jet can slide along its output axis as needed. All parts are made of copper.

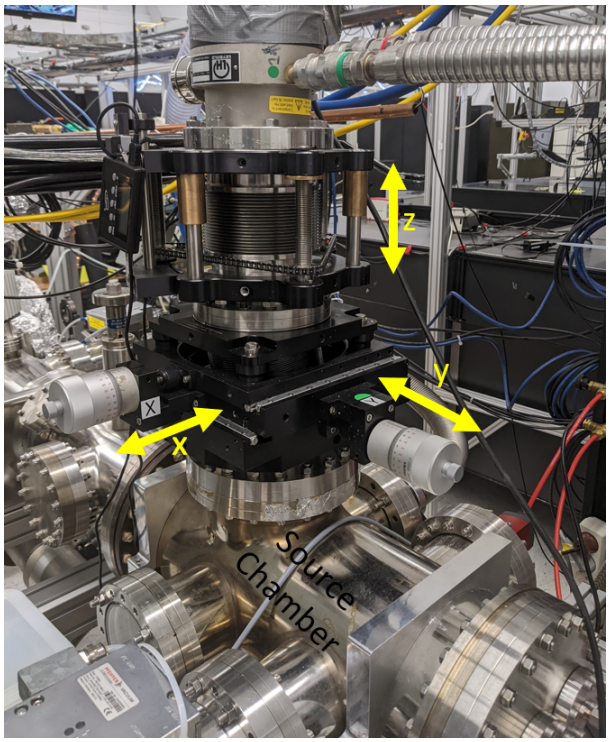

FIGURE 3.7: The COLTRIMS source chamber, labelled, and jet translation stage. The stage offers x, y and z translation shown with yellow arrows, needed to align the jet with the skimmer.

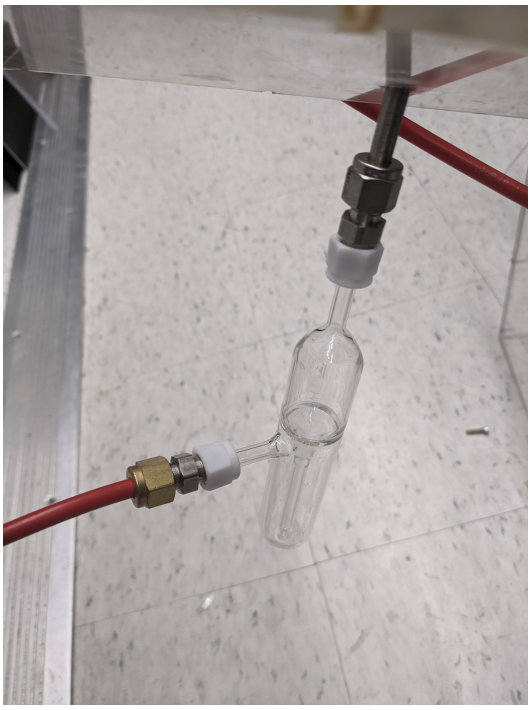

FIGURE 3.8: A liquid-gas bubbler, built by Michael Vandenhoff, the glass-blower at the National Research Council. Gas is forced down the capillary into a reservoir of the target liquid, whose vapour is carried on to the experiment through the output arm.

up or freeze upon expansion. Shown in Figure 3.8 is the solution to this problem, a bubbler attached to the usual gas line. Gas, argon in this case, is forced through the capillary into a reservoir of propylene oxide at the bottom of the bubbler, carrying some of the vapour with it as it travels further down the line. This is sufficient to see a significant density of propylene oxide in the experiment.

3.2.3 Signal Processing

COLTRIMS is a highly engineered machine that is capable of handling the acquisition of three-dimensional data from many thousands of electron and ion hits per second. As such, the signal processing requirements are complex, and will be discussed in this section.

To detect the ions and electrons produced in an experiment, two micro channel plates (MCPs) are employed on either end of the spectrometer, as seen in Figure 3.9. An MCP is essentially a thin glass disc with many small (10-25 μm diameter) channels, schematically shown in Figure 3.10. The surfaces on opposite sides of the MCP are placed at a potential difference of approximately 2 kV, with the back side as the anode, thus attracting electrons. When a charged particle strikes the inside of a channel, secondary electrons are produced and accelerated towards the back, causing a shower of

FIGURE 3.9: The design schematic of the COLTRIMS spectrometer. A constant voltage is applied across the metallic plates throughout the spectrometer, accelerating charged particles towards the MCPs on either end, where the signal detection begins.

electrons to be emitted from the channel. The larger the voltage placed over the MCP, the higher the electron gain becomes. However, if the voltage is too large, amplification noise becomes strong due to additional charged ions creating their own electron cascades.

Behind the MCPs are hexagonal delayline anodes, which supply the two-dimensional position of the electron shower caused by the MCP, seen in Figure 3.11. The three delayline layers are labelled u,v and w for both the ion and electron detector. When the wires are struck by electrons, a voltage pulse propagates along them in each direction. The time of arrival of each pulse is measured at the wire ends, and the position can be calculated as:

$$u = s_u(t_{u1} - t_{u2})\,, \tag{3.3}$$

where u is the position of the electron hit, t_{u1} and t_{u2} are the times of detection at each end of the wire respectively, and s_u is a scaling factor which is calibrated in the data analysis. In this formalism, 0 corresponds to the centre of the wire. This process can be visualized in Figure 3.12.

The position on the layer in u, v, and w can then be converted into x and y with any given pair of layers:

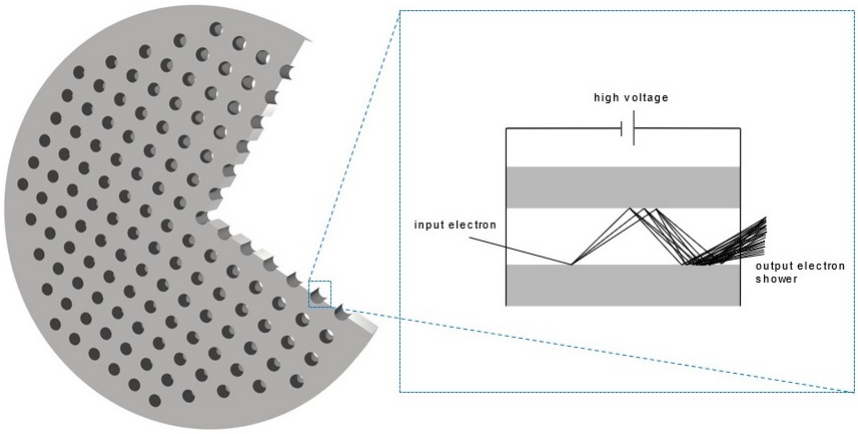

FIGURE 3.10: A cross section of an MCP. The front and back side of the MCP are placed at a large potential difference, accelerating electrons towards the back. When electrons strike the walls of a channel, secondary electrons are produced, causing the output to be an electron shower.

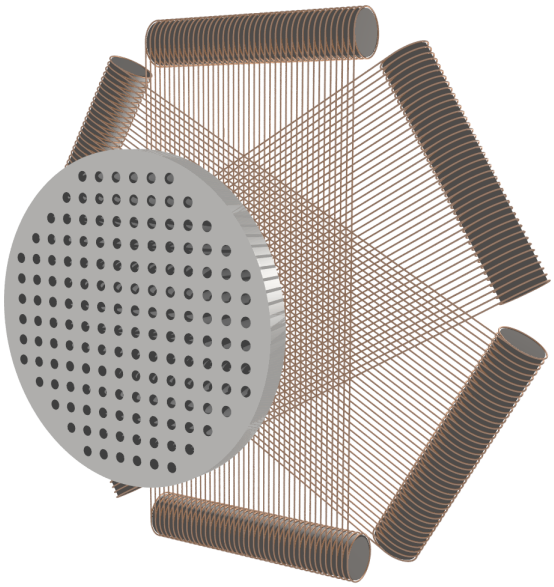

FIGURE 3.11: A schematic hexagonal delayline anode detector.

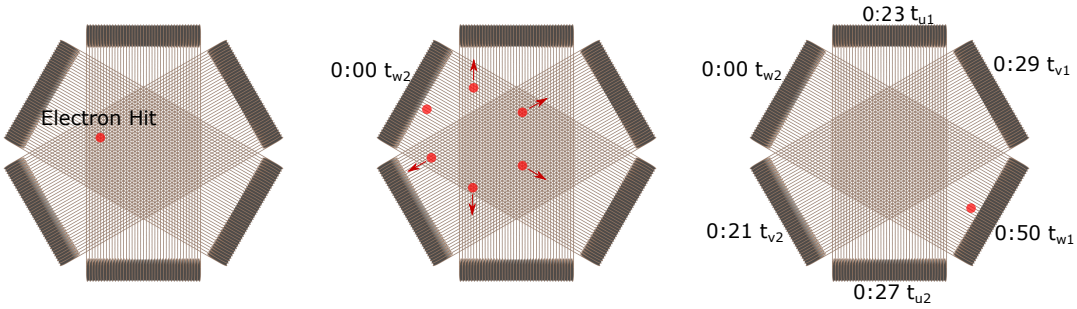

FIGURE 3.12: Position detection of the hexagonal delayline. In the left-most image, an electron shower hits the delay lines in the spot marked by the red circle. Next, in the centre image, pulses propagate towards the end of the wires. At time 0:00, the first electron pulse triggers the second clock on the w-layer. In the right-most image, the last pulse travelling along the wires gets measured by the first w-layer clock. The positional information is found by comparing timings between clocks of each layer.

$$x_{uv} = u\,, \tag{3.4}$$

$$y_{uv} = \frac{2v - u}{\sqrt{3}}\,, \tag{3.5}$$

$$x_{uw} = u\,, \tag{3.6}$$

$$y_{uw} = \frac{2w + u}{\sqrt{3}}\,, \tag{3.7}$$

$$x_{vw} = v - w\,, \tag{3.8}$$

$$y_{vw} = \frac{v + w}{\sqrt{3}}\,, \tag{3.9}$$

where the subscript on x and y denotes the layer pair. Note that these values are degenerate by design, an advantage of the hexagonal mesh. A rectangular system would suffice, but the degeneracy both reduces detector dead time between hits and helps resolve otherwise ambiguous positions.

All signals measured by COLTRIMS detectors are analogue voltage pulses. Since these pulses vary in amplitude due to the choice of applied voltage over the MCP, triggering based entirely on pulse height would lead to a large uncertainty. To combat this issue, the COLTRIMS uses constant fraction discrimination to trigger. The analogue signal is split somewhere between a 40:60 and to 20:80 ratio, and the larger fraction is delayed, while the smaller fraction is inverted. The signals are recombined, creating a pulse that first dips below zero and then crosses zero before rising to a positive voltage. The zero crossing occurs at a constant fraction of the original pulse peak. It is at this zero crossing that the constant fraction discriminator generates a logical NIM-pulse, which is later converted into a timing signal by a time to digital converter (TDC). While this is straightforward in principle, it requires a fair bit of circuitry, as demonstrated in Figure

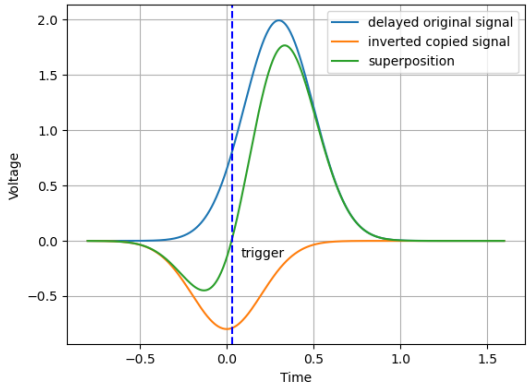

FIGURE 3.13: Three voltage pulses shown to demonstrate constant fraction discrimination. The blue pulse is the delayed original signal, and the orange the inverted copy. When superimposed, they give the green pulse, triggering the constant fraction discriminator at its zero crossing.

3.14.

The signals are then sent to a PC for collection. Two separate but synchronized TDC PCI buses handle the digitization of the data. The PC software that handles the recording and a live basic analysis of the data is called COBOLD, designed by RoentDek. Information regarding each hit is recorded into a list mode file (LMF) event by event. COBOLD is a versatile software in that it allows for considerable customization of what data is acquired and how it is managed post acquisition. A more in depth discussion of how to use COBOLD may be found in Appendix C. A summary of COLTRIMS signal processing may be found in Figure 3.15.

3.2.4 Calculation of Momentum

The coordinate system we use in COLTRIMS is as follows:

x: Along the propagation direction

y: Along the jet direction

z: Along the spectrometer direction

For both ions and electrons, x- and y-momentum is obtained by analyzing positional data collected from the MCPs, and z-momentum is obtained based on timing information. In general, Newton's equations are solved, where the total force on any charged particle can be given by the sum of the force from the electric and magnetic fields:

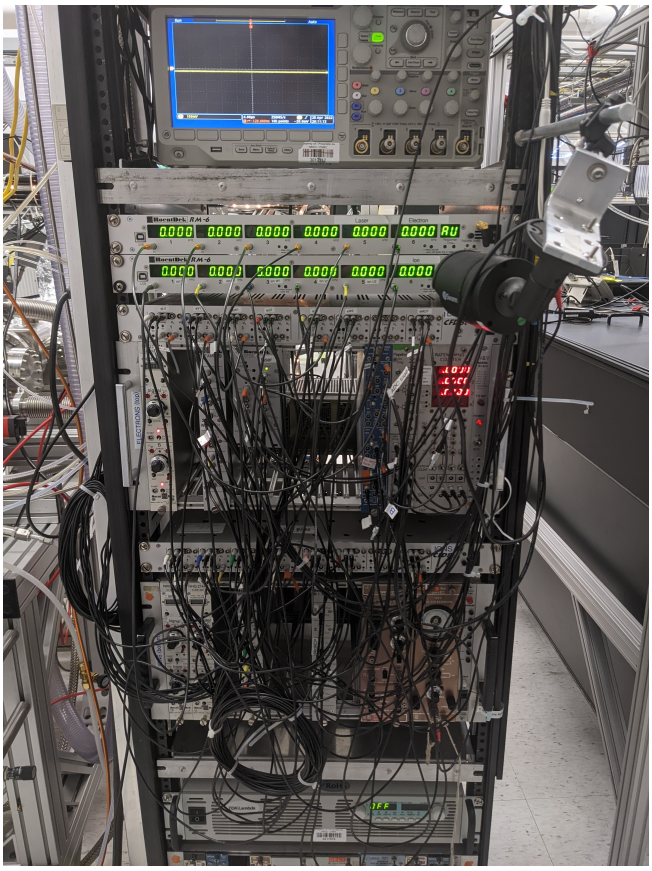

FIGURE 3.14: The real life view of the COLTRIMS signal processing cabinet. Upon careful observation, one can see that it's not actually composed of squid-ink spaghetti, but many logically placed NIM cables. The green values display the detection rates for each u,v, and w layer, as well as the laser frequency, and ion and electron rates overall. The horizontal box below is the electron detector delayline, and further below that the ion detector delayline. The spectrometer and MCP settings are controlled by vertical panels in the bottom left, and at the very bottom of the image is the current control for the Helmholtz coils.

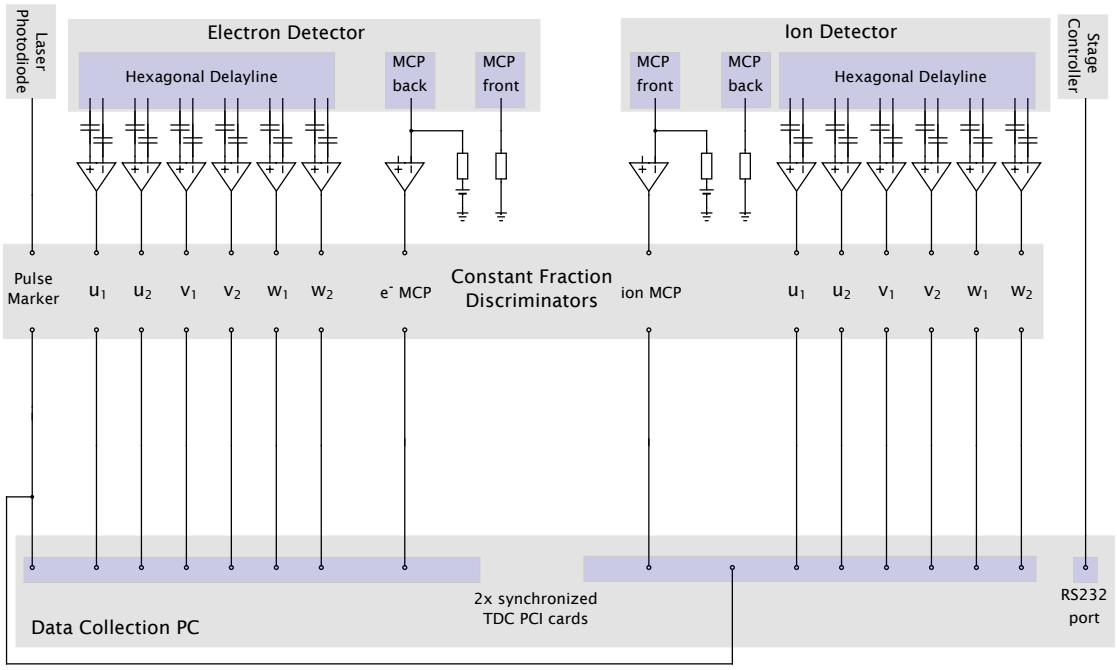

FIGURE 3.15: A summary of the COLTRIMS signal processing method. Analogue voltage signals are picked up on charged particle detectors, then travel through constant fraction discriminators to the data collection PC where they are read by TDC PCI cards. The pulse timing information from a laser photodiode follows a similar procedure. Delay stage data is collected via a direct connection to the PC.

$$\begin{aligned}\vec{F} &= \vec{F_E} + \vec{F_B} \\ &= q(\vec{E} + \vec{v} \times \vec{B}) \\ &= q \begin{pmatrix} E_x + v_y B_z - v_z B_y \\ E_y + v_z B_x - v_x B_z \\ E_z + v_x B_y - v_y B_x \end{pmatrix} ,\end{aligned} \tag{3.10}$$

then, since $\vec{E}$ and $\vec{B}$ are both only along the z-direction, this simplifies to:

$$\vec{F} = \begin{pmatrix} v_y B \\ -v_x B \\ E \end{pmatrix} . \tag{3.11}$$

Now what remains is to solve for $\vec{v}$, and get $\vec{p} = m\vec{v}$.

Positional Analysis

For ions, the force of the magnetic field is negligible. This means that there is no accelerations for ions in the x- or y-direction, so the momentum is directly related to the detected position on the MCP:

$$p_{x,i} = \frac{m_i x}{t} , \tag{3.12}$$

$$p_{y,i} = \frac{m_i y}{t} , \tag{3.13}$$

where m_i is the ionic mass and t is the time of flight. For electrons, it is a bit more complex. The magnetic field adds positionally dependent acceleration, so the differential equations to solve are:

$$\dot{v}_x = \frac{q_e}{m_e} B v_y , \tag{3.14}$$

and

$$\dot{v}_y = -\frac{q_e}{m_e} B v_x . \tag{3.15}$$

These equations yield the following solutions, where ω_r is the electron's rotational frequency in the magnetic field:

$$p_{x,e} = \frac{m_e \omega_r}{2} \left(x \cot \frac{\omega_r t}{2} - y \right) , \tag{3.16}$$

and

$$p_{y,e} = \frac{m_e \omega_r}{2}\left(y \cot\frac{\omega_r t}{2} + x\right). \tag{3.17}$$

Typical plots of raw data and the resulting electron momentum in x and y from the ionization of propylene oxide in the experiments detailed in this thesis can be seen in Figure 3.16.

Time of Flight Analysis

The time of flight (ToF) axis is the direction with the highest resolution of measurement in COLTRIMS. A photodiode is placed in the beam path which senses the arrival of the laser pulse, starting a clock which ends upon the detection of a hit on the MCPs. The additional times required for the light to travel between the photodiode and molecular interaction region, as well as for analogue signal processing, are calibrated and accounted for in the analysis.

For ions and electrons, the solution is effectively the same, and depends only on constants, the spectrometer length for ions and electrons respectively, $d_{i,spec}$ and $d_{e,spec}$, and time of flight:

$$p_{z,i} = m_i\left(\frac{q_i E t}{2} - \frac{d_{i,spec}}{t}\right), \tag{3.18}$$

$$p_{z,e} = m_e\left(\frac{q_e E t}{2} - \frac{d_{e,spec}}{t}\right). \tag{3.19}$$

It is worth noting that, while the machine in this experiment is not, many COLTRIMS systems are equipped with a "drift tube", which is a length of chamber before the MCPs in which no electric field is present. This complicates the equations of motion significantly, and as such, in our data analysis, p_z is solved from time of flight iteratively.

A great deal of information about any given COLTRIMS experiment can be gleaned simply by looking at a time of flight spectrum. Time of flight for any given ionic species scales with its mass and charge as $\sqrt{m/q}$. Identification of these species in a spectrum can be performed from the relative positions of the peaks. In the case of ambiguities, the shape of the peak can help determine the species. For example, H_2^+ and Deuterium$^+$ have the same $\sqrt{m/q}$, but Deuterium$^+$ will have a broader ToF spectrum due to being part of a molecular breakup, whereas H_2^+ will have a very narrow peak in momentum strictly due to the ionization. Examples of these spectra are shown in 3.17 for two different cases. The first is a a jet composed solely of argon gas, while the second is a jet of argon gas that has been bubbled through liquid phase propylene oxide.

As seen in both curves, the most prevalent ionization by far is from argon and propylene oxide. In the pure argon experiment, there are also peaks representing events where

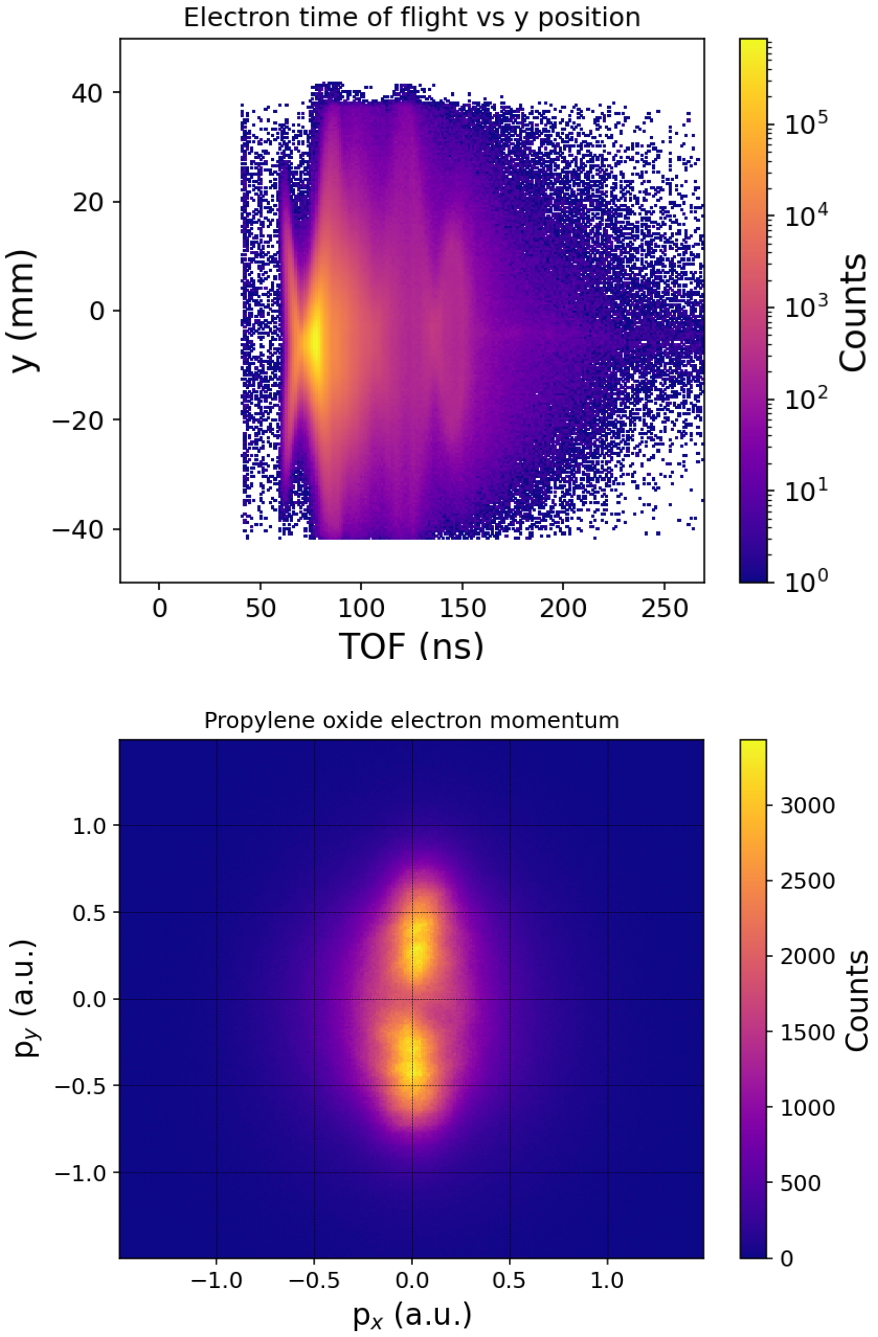

FIGURE 3.16: The raw time of flight and position spectrum (above) yields an example electron momentum distribution for propylene oxide in the x and y directions (below).

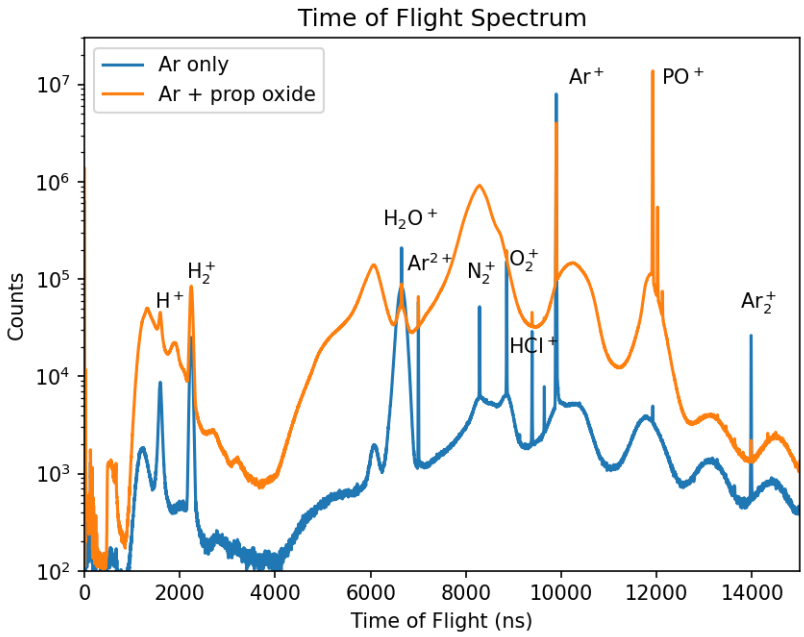

FIGURE 3.17: Typical time of flight spectra for an experiment with an argon jet only, and an argon jet bubbled through liquid phase propylene oxide. Interesting ion species are labelled.

argon is doubly ionized, as well as the argon dimer singly ionized. If desired, the experiment may be tuned to maximize these types of events, for example to study non-sequential double ionization, but that is not the case in this work. The propylene oxide experiment has broad peaks around 6000 and 8000 ns, which are due to fragmentation of propylene oxide. These fragments provide a host of information regarding the breakup of propylene oxide.

Many other ion species also have distinctive peaks. N_2^+ and O_2^+ show up at the beginning of the experiment as any remaining air in the gas line is pushed through the nozzle. As it is impossible to create a perfect vacuum in the COLTRIMS chamber, background gases such as water and H_2^+/H^+ are also seen. The signature of a background gas is a more diffuse peak compared to the narrow ones from gases in the jet. Small amounts of HCl^+ can sometimes be found in the jet, as hydrochloric acid is used to clean the nozzle when it gets clogged. The argon spectrum additionally shows a small peak of propylene oxide due to remnants from the previous experiment in the gas lines.

During the analysis process, time of flight is used to choose ion species of interest. For example, choosing a narrow window over the argon peak ensures that only ionization events from argon in the jet (with a relatively tiny amount of background) are shown in momenta spectra. This applies to both electron and ion information; only electrons which are measured in coincidence with these argon ions are added to the

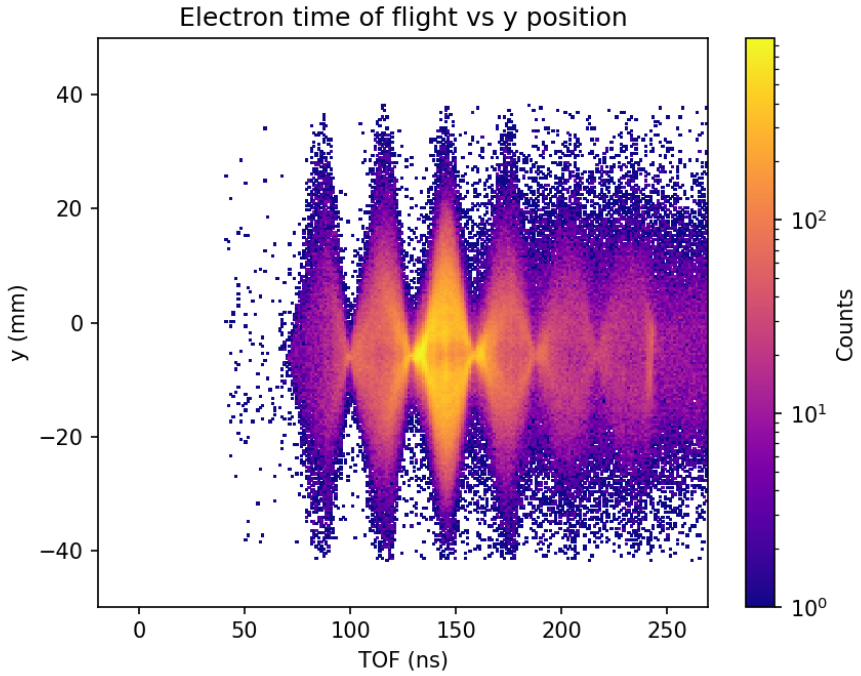

FIGURE 3.18: A demonstration of the rotation of electrons in the COLTRIMS' magnetic field, shown in a plot of electron time of flight versus position in y. Once per cycle, the positional information is lost due to the convergence to a node. This example data is taken using a smaller than usual electric field in order to exaggerate the cyclical structure.

respective spectra.

While the rotation of electrons in the magnetic field is crucial for containing the electrons on the detector, as well as increasing momentum resolution, it also comes with a downside. Once every rotation period, the electrons converge on a node, causing all momentum resolution in the x- and y-directions to become 0, and thus losing all momentum information. An example of a raw electron time of flight versus position spectrum is displayed in Fig 3.18; this data is taken using a very low spectrometer electric field, which causes the electrons to spread out in time and exaggerate the distribution of nodes.

This issue, however, is avoided with relative ease. Tuning the current passed through the Helmholtz coils, and thus the overall strength of the magnetic field, with a given spectrometer electric field strength allows the user to adjust the frequency and positioning of the nodes. All that is needed is to place the bulk of the electron distribution in between the nodes in time, as is properly demonstrated in the raw data spectrum in Fig 3.19.

In this thesis, the electron momentum in the z-direction will typically be presented

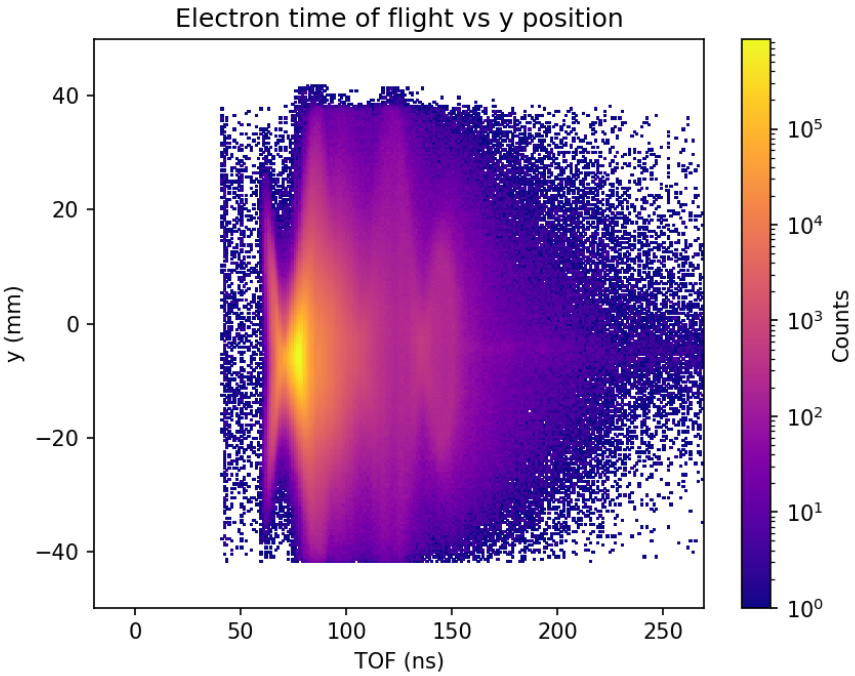

FIGURE 3.19: A typical plot of electron time of flight versus y position. The electrons are largely distributed outside of the node, meaning there is no ambiguity in the x or y momentum data.

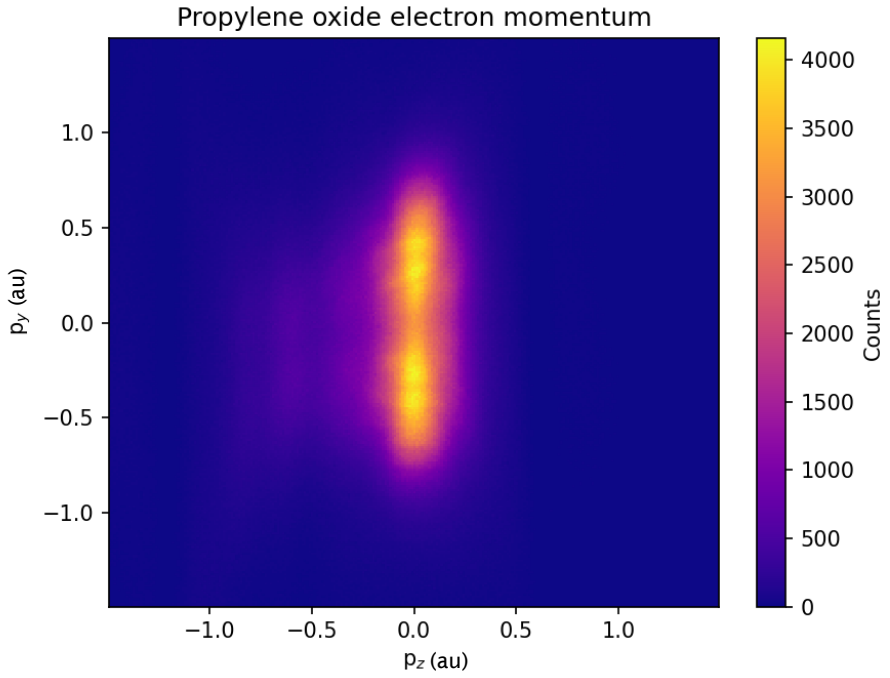

FIGURE 3.20: An example electron momentum distribution for propylene oxide in the y and z directions.

alongside the momentum in the y-direction, as shown for propylene oxide in the following example in Figure 3.20.

Necessary Calibrations

In order to complete the fairly involved data analysis process, the following quantities must be calibrated in order to output correct results. This is done in an iterative process, observing the quality of individual plots and adjusting values until they each satisfy the appropriate criteria. These calibrations typically must be performed once for a set of experiments.

- **Timesum offsets:** Requisite for properly calibrating positions using the delayline detector. These values can be found in the raw data by zeroing the peak in the one-dimensional timing plots.
- **Delayline scale factors:** The scale factor of the u layer is set to an arbitrary value. The analysis suite varies scale factors for the other two layers around this value, calculating positions using layers u and v, and u and w. The differences are plotted, and the minimum gives the ideal ratio of scale factors for the other two layers.

- **Third layer offsets:** The centre of the u and v layer determine the origin of the detector. The w layer is not exactly centred at this point. This is calibrated using the analysis suite.

- **Spectrometer field:** Necessary for calculating both electron and ion momentum. This is known to an approximate level based on settings chosen in the lab, but can be further tuned by looking at momentum conservation in single ionization. This can be seen, for example, by plotting the one-dimensional value of $p_{e,z} + p_{i,z}$ which must be centred on 0 due to conservation of momentum.

- **Length of spectrometer:** Needed for momenta calculations in the z-direction. This value is approximately 10 cm for our COLTRIMS, in both the ion and electron direction. However, adjustments of up to 1 mm can be helpful if it is difficult to achieve nice momentum conservation with just changes to the spectrometer field alone.

- **Cyclotron period:** The time difference between successive nodes due to rotation of electrons in the magnetic field. This is necessary to compute electron momenta, and is easiest to calibrate by performing a separate brief experiment with a very low spectrometer field. In this case, the electron distribution spreads out over a large time period, and many nodes can be seen individually.

- **Time of flight offset:** For electrons, this value corresponds to the timing of the first node of rotation due to magnetic field . It can be computed by looking at the first visible node in the x_e vs t_e plot, and moving back (typically) one or two gyration periods. For ions, this can be computed from the relative timing of two different ionic species.

- **x and y-offsets:** Necessary to centre momenta distributions. For electrons, it is surprisingly easier to look at the position of nodes in x_e vs t_e and y_e vs t_e than using the x_e vs y_e plot directly. For ions, it must be calibrated for each ion species using its x_i vs y_i plot.

- **Detector angle:** Rotation of data to the lab frame. This is the same between experiments, and is straightforward to calibrate using a known momentum distribution (i.e. linearly polarized light along the jet axis.)

3.3 Optical Setup

In order to generate a synthetically chiral pulse, we need to fabricate an optical setup which can create and control two arms with orthogonally polarized 800 nm and 400 nm pulses. These two arms must propagate in a parallel but non-collinear fashion to

be focused into the same focal volume by the COLTRIMS mirror, but also satisfy the necessary angle between the two. A schematic view of the optical setup used in this experiment to achieve this is shown in Figure 3.21. First, the beam is passed through a 3:1 telescope, reducing its spot size from approximately 1 cm in diameter to 3.3 mm. The entrance window to the COLTRIMS main chamber is only 2cm in diameter, so in order to have two parallel beams separated by 1 cm, this reduction in size is necessary to avoid clipping the beams. Secondly, this increases the intensity concentration in the beam, meaning that more 400 nm light can be generated when using a nonlinear crystal. The beam is then split by a 50/50 beam splitter, creating the two arms of the experiment that will eventually travel in parallel. Each arm needs to have approximately the same path length so that they will arrive in the COLTRIMS at the same time; a delay stage is placed in one arm to ensure the ability to achieve this.

The beam goes through the same elements in each arm to create and manage 2ω. A 200 μm barium borate (BBO) crystal generates 400 nm light perpendicular in polarization to the fundamental 800 nm using second harmonic generation. Approximately 2.5 mm of calcite is placed in each path to handle dispersion between the two colours. Calcite is birefringent; the 2ω propagates through the crystal along the axis with lower refractive index, while the ω travels through the higher refractive index, causing the necessary 2ω to catch up in time. This value is fixed depending on the total thickness of calcite the beam propagates through. For this reason, a pair of fused silica wedges are placed in the beam path, which can slide in and out to slowly adjust the amount of glass in the path, and thus can fine tune dispersion. Additionally, a rotatable silica window is placed in each arm, which can fine tune the relative phase between ω and 2ω and will be discussed further in the Phase Control section. The real-life setup is presented in Figure 3.22.

3.3.1 Overlap

A significant challenge in this experiment arises from the need to use four individual pulses which must be overlapped in both space and time. This can be measured by observing the overall ionization rate, which will be constant (barring statistical fluctuation) unless overlap has been achieved, when the rate will peak.

The ω and 2ω pulses are collinear in each arm, which satisfies the spatial condition by default, but the two arms must be overlapped when focused by the parabolic mirror in the COLTRIMS main chamber. This is achieved when the two arms are travelling in parallel. In order to accomplish this, a physical target was made with the intended spacing of the beams ($\sim$ 0.9cm) marked on it. Then, the beam was adjusted in the near field (immediately after recombination) and far field ($\sim$ 5m down the table) so that the target is hit at each location. This is sufficient to roughly ensure parallelity, however further small tweaks to pointing were needed to attain overlap.

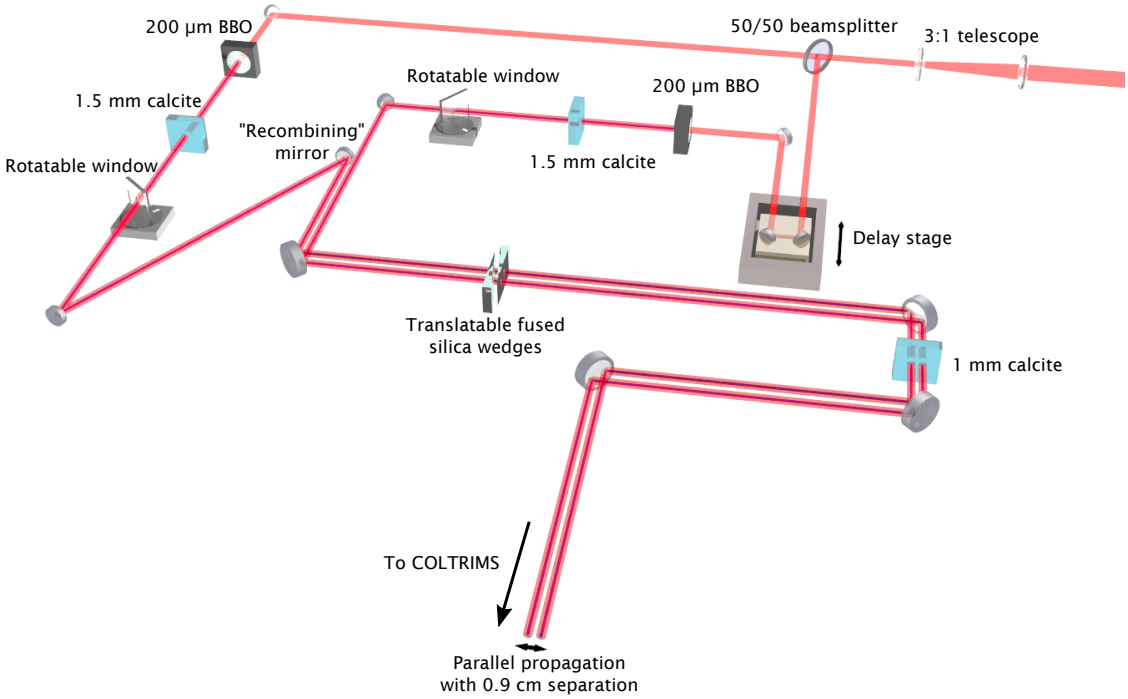

FIGURE 3.21: A schematic interpretation of the optical setup used in the experiment. An 800 nm ultrafast pulse is shrunk in a 3:1 telescope, and split into two arms. Each arm is propagated through a BBO crystal, generating 2ω centred at 400 nm. Both beams then travel through 2.5 mm total calcite thickness and two fused silica wedges to balance the dispersion, keeping the ω and 2ω pulses together in time.

Temporal overlap is managed in two ways. To control the timing of the ω pulses in each arm, a delay stage is installed in one of them, which will change the path length as desired until both arms match. Dispersion must also be managed in order to ensure temporal overlap of the ω and 2ω pulses in each arm. The index of refraction of a material for a given wavelength λ can be calculated using the Sellemeier equation:

$$n^2(\lambda) = 1 + \sum_i \frac{B_i \lambda^2}{\lambda^2 - C_i}, \tag{3.20}$$

where B_i and C_i are experimentally determined coefficients obtained in publicly available look-up tables. This equation was used to calculate the dispersion due to air, the COLTRIMS window, and a fused silica wedge pair, and subsequently to find the amount of calcite we would need to compensate for these effects. Overall, 2.5 mm of calcite is inserted in the beam path to help compensate for dispersion. We were able to fine tune this using the wedge pair, which has adjustable dispersion. Evidence that ω and 2ω are overlapped can be seen in the streaking of ionized electrons, which will be discussed further in the next section.

The biggest difficulty lies in the fact that both spatial and temporal overlap must be

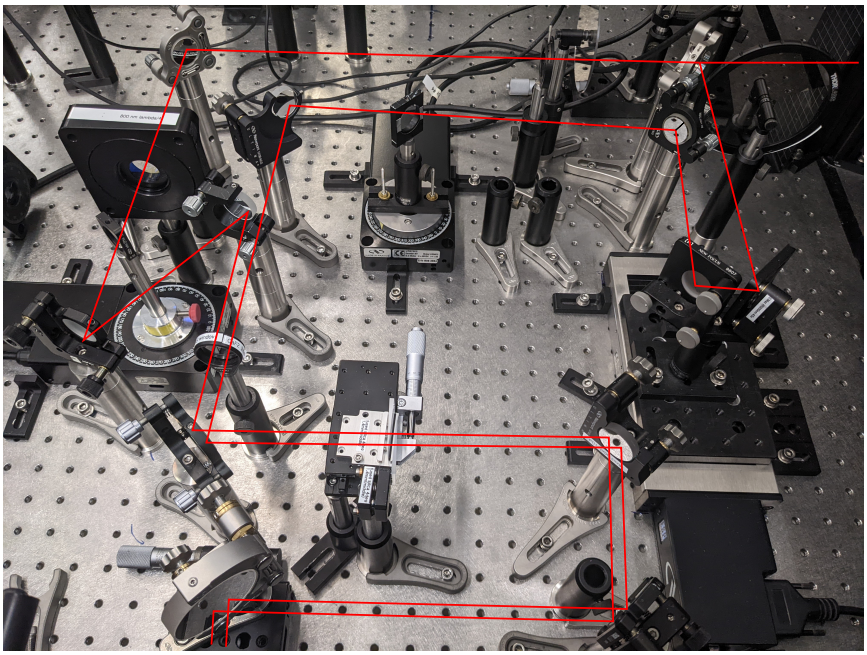

FIGURE 3.22: The real-life optical equipment needed to perform the experiment detailed in this thesis. The beam path is traced in red. For more information about the specific equipment, see Figure 3.21.

achieved at the same time to notice that either has happened at all. This unfortunately led to a trial and error approach of adjusting the direction of one arm very slightly, followed by an overnight scan of the delay stage to check if any peak in count rate can be seen. It was necessary to scan for a long period of time since the peak in ionization due to overlap is only slightly higher than the range of statistical fluctuation of the count rate. The peak becomes clear after the aggregation of a large amount of statistics. Eventually, after approximately a month of twiddling and scanning, a successful result was found, and is shown in Figure 3.23. The narrow peak in counts at 1.04 mm proves that overlap has been attained; the increase in intensity due to the combination of fields increases the ionization rate considerably.

3.3.2 ω-2ω Phase control

While the pulse scheme used in this experiment guarantees local chirality, it is crucial to measure and control the ω-2ω phase difference in each arm in order to set the handedness globally, ie that the handedness remains as desired across the focal plane. To control this phase, a thin $\sim$ 100 μm fused-silica window is placed on a rotational stage in each arm. By rotating the window, one can tune the dispersion finely enough to control the phase difference on a sub-wavelength scale. To measure and characterize this process, an optical streaking measurement can be performed, similar to the one devised

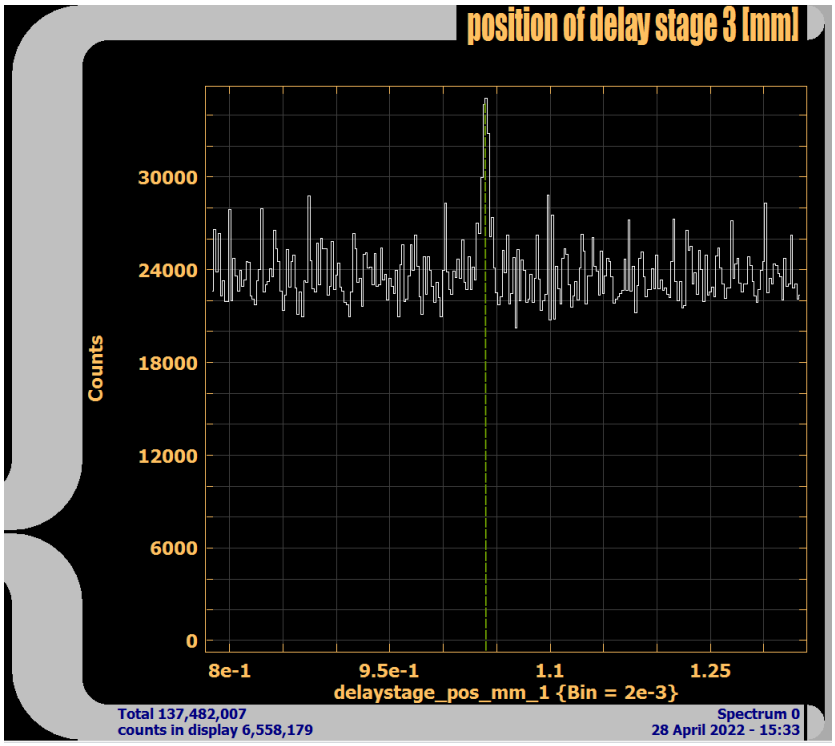

FIGURE 3.23: Proof of the overlap of the two horizontally polarized 800 nm pulses. The large peak at 1.04 mm is only seen when the pulses are overlapped in space and time, and only stands out from the background data when given sufficient collection time. This is due to short-term statistical fluctuation.

by Itatani *et al* in 2002 [92]. Each arm is sent into the COLTRIMS individually; ionization occurs primarily at the peak of the ω field, and the 2ω field contributes momentum along its polarization, in the z-direction. As the window is rotated, the momentum of ionized electrons shifts according to the timing of the 2ω pulse with respect to the peak of the ω pulse. A typical scan of rotation angle is seen in Figure 3.24. To reduce noise, each bin of 0.1° is averaged to a single value in p_z, and further averaged with its nearest neighbours. The result can be seen in Figure 3.25, where four key phase conditions are labelled.

The dotted lines in Figure 3.25 correspond to the following conditions, summarized in Table 3.1:

Case (a) At 43.1°, $p_z = 0$, with a negative derivative. Thus, at the maximum ω field, the 2ω vector potential is 0, and the electric field is at its minimum value.

Case (b) At 48.9°, $p_z =$ minimum. Thus, at the maximum ω field, the 2ω vector potential is at its minimum value, and the electric field is 0.

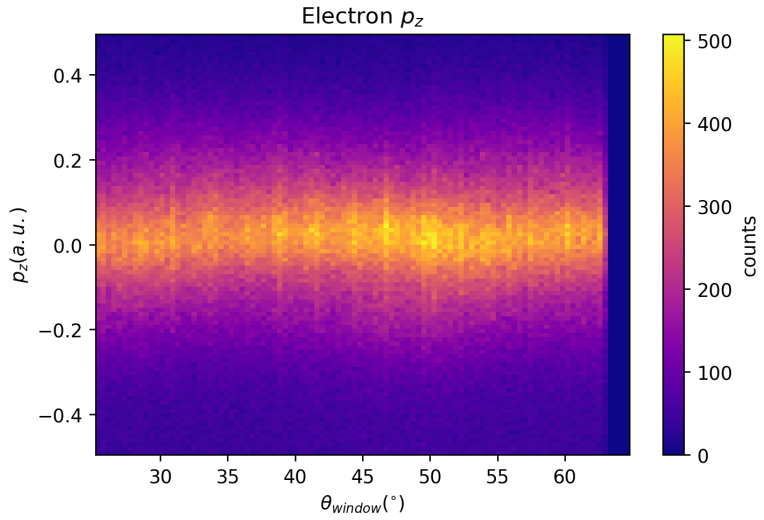

FIGURE 3.24: Raw data of the window angle versus the electron z momentum.

TABLE 3.1: Cases of OTC field shapes at four different phase conditions. The overall shape column represents the path the electric field traces as the pulse propagates forward in time.

Case	Angle (°)	Vector Potential	Electric Field	Overall Shape
a	43.1	0	minimum	
b	48.9	minimum	0	
c	54.7	0	maximum	
d	59.1	maximum	0	

Case (c) At 54.7°, $p_z = 0$, with a positive derivative. Thus, at the maximum ω field, the 2ω vector potential is 0, and the electric field is at its maximum value.

Case (d) At 59.1°, $p_z =$ maximum. Thus, at the maximum ω field, the 2ω vector potential is at its maximum value, and the electric field is 0.

The asymmetry seen around 35° is likely due to a fluctuation in laser intensity, causing the energy of the 2ω pulse to vary, and thus p_z. For this reason, the peak at this angle is not used.

By choosing the phase conditions for each arm, it is possible to control the global chirality, as shown in Figure 2.23. Matching case (a) in the left arm with (c) in the right, or (b) left with (d) right, yields a globally chiral field. Similarly, matching case (c) in

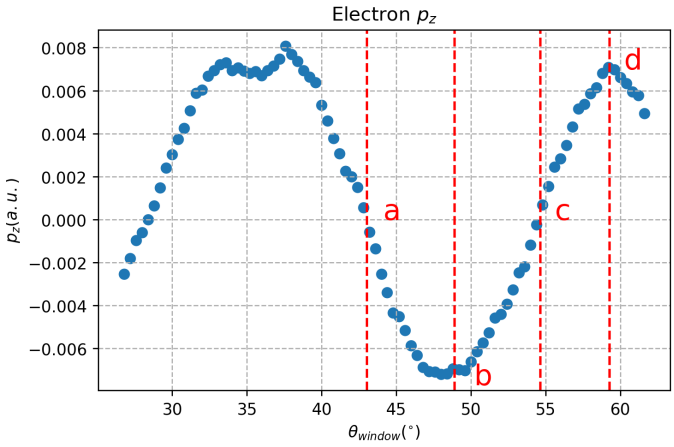

FIGURE 3.25: Averaged streaking data to make the oscillation of z momentum clear. Four examples are labelled a,b,c and d at 43.1°, 48.9°, 54.7°, and 59.1° respectively.

the left arm with (a) in the right, or (d) left with (b) right, will also yield a globally chiral field, but of the opposite handedness. Matching any case with itself will give a globally achiral field. The inherent difference between (a) and (b) is simply the shape of the vector potential and electric field. For the sake of simplicity, in our experiments, we only chose pulses of shape (b) and (d) to generate globally left-handed, right-handed and achiral fields.

Chapter 4

Results

"No one but a theorist believes their theory; everyone puts faith in a laboratory result but the experimenter themselves."

Albert Einstein

This chapter will present the results of our experiments with locally chiral light, or light with synthesized chirality. First, we will review simulations of the local and global distribution of the electric field over the macroscopic dimensions of an experimental laser focus. Then, we will show the inherent PECD resulting from the chirality of the laser field alone, using an achiral, i.e., atomic target. To this end, we will use argon gas. We will then examine the influence of a chiral target on the PECD in such a chiral field. A characterization of the overall degree of chirality will be presented subsequently. Finally, a look into the sensitivity of the yield of each propylene oxide enantiomer will be discussed. All analytical work in Chapter 4 was undertaken by me, apart from the simulations in Section 4.3 by Georgios Katsoulis from our work [93].

4.1 Field Calculations

In order to get a better sense of the complicated three dimensional field structure, we performed calculations to show the behaviour of the interference patterns in the focus. We map coordinate space across the focus using Equation 2.17 for the field, and then give the field a Gaussian envelope in space such that:

$$E(r,x) = E_0 \frac{w_0}{w(x)} \exp\left(\frac{-r^2}{w(x)^2}\right), \tag{4.1}$$

where the width of the beam as it propagates along x, $w(x)$, is given by:

$$w(x) = w_0 \sqrt{1 + \left(\frac{x}{x_R}\right)^2}, \tag{4.2}$$

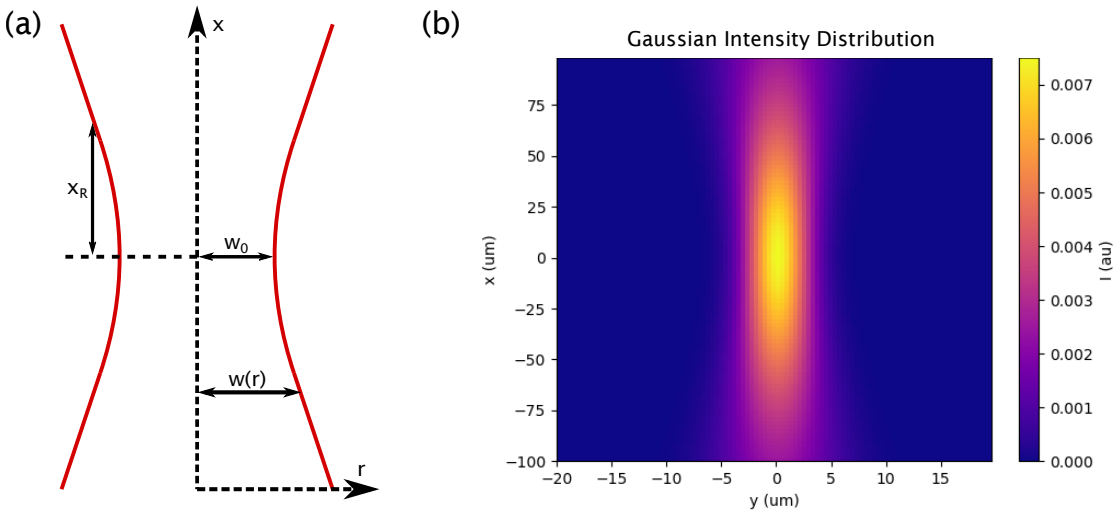

FIGURE 4.1: (a): A schematic representation of the focus of a beam with a Gaussian intensity profile propagating along x. (b): The calculated intensity distribution in the focal volume of such a beam. The intensity is given in atomic units.

with w_0 the beam waist, and x_R the Rayleigh range, defined as:

$$x_R = \frac{\pi w_0^2 n}{\lambda}, \tag{4.3}$$

where λ is the wavelength and n is the refractive index of the propagation medium. A calculation of a Gaussian profile with an intensity of 1×10^{14} W/cm^2 and wavelength of 800 nm is shown in Figure 4.1. The input beam size is 3 mm, and the focusing mirror has a focal length of 5 cm.

The results of the calculation when using the full four-pulse scheme are shown in Figure 4.2, where we look at both the intensity and field in z-direction. The phase conditions in these plots were chosen such that the relative phase between all pulses is 0, but a much larger phase space was investigated, making the movies which may be found here. The intensity grating shows that ionization will be due mostly to the large central peak; the movie, due to shifting the phase between ω in each arm, demonstrates that the variation of relative ω phase changes the location of intensity minima, but the central peak still dominates. The z-direction grating plot, and movie due to shifting the phase difference between ω and 2ω in one arm, confirm what we know about the phase conditions discussed in Chapter 3: there is a variation between positive and negative across the focus, and that changing the relative 2ω phase will shift this pattern. Note that choosing the relative 2ω phases determines the global handedness of the field, as it changes the position of the z-direction field grating with respect to the position of the ellipticity grating.

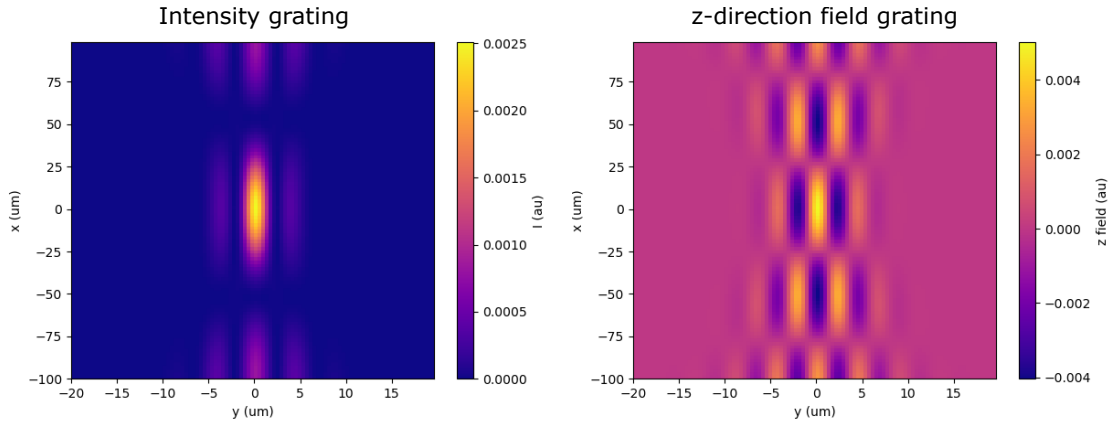

FIGURE 4.2: Calculation of the laser focus with synthesized chirality in the same geometry as in Figure 4.1. Two perpendicularly polarized two-colour (800 nm & 400 nm) Gaussian pulses are overlapped at an angle of 5°. Left: Intensity distribution. Right: Field distribution along the z-direction (400 nm). These interference gratings are as seen in Figure 2.22.

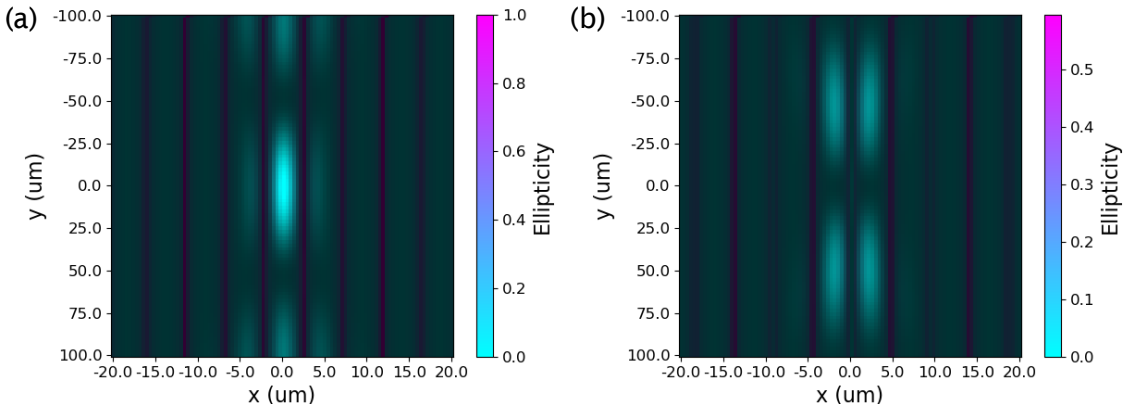

FIGURE 4.3: Calculation of the electric field in the focus, shown in the overall propagation direction x and jet direction y. The ellipticity of the field is indicated by the hue as shown on the colour map, and the intensity given by the shade of this hue. Plot (a) has relative ω phase of 0, and plot (b) has a relative ω phase of π.

As discussed in Section 2.3.4, the ellipticity in the xy plane is also an important feature of the field. Due to the interference between the two beams, the field E_y varies across the focus, making a grating. A plot detailing intensity with ellipticity is shown in Figure 4.3. The left side shows all relative phases chosen to be 0, and the right side has the relative ω phases π, and a movie with a variation of relative ω phases is found here. This Figure and movie once again confirm that the ellipticity varies as we expect across the focus, as seen in Figure 2.23. Adjusting the relative 2ω phase does not change the ellipticity grating in the xy plane. The addition of intensity to this plot also gives us new insight. Unfortunately, we see that the areas of highest intensity tend to have the lowest ellipticity, meaning the "strength" of the chirality of the field is low in the intense peak that elicits the most ionization.

While this weakness is inherently a property of our pulse scheme with strong field ionization, normalized differences (as seen in Section 2.2.1, for example) are a powerful technique for resolving small dissimilarities between distributions. Additionally, we note that it has been possible to see asymmetries in photoelectron spectra due to magnetic dipole effects in the past, such as in Smeenk et al in 2011 [94]. These magnetic dipole effects are much smaller than the electric dipole effects due to fields with the strongest chirality in our setup.

4.2 Experimental Results

We performed five separate photoionization experiments as follows: ionization of argon and S-propylene oxide with globally left-handed, right-handed, and achiral fields, and ionization of argon and R-propylene oxide with globally left- and right-handed fields. We attempted to keep experimental conditions as identical as possible throughout. Each 800 nm pulse was approximately 25 fs in duration, with 100 mW of power, corresponding to a focal intensity of 1×10^{14} W/cm^2. Each 400 nm pulse had approximately 6 mW of power, corresponding to a focal intensity of 2×10^{12} W/cm^2. Based on independent measurements of the 400 nm pulse using a transient grating FROG setup, the pulse duration was estimated to be around 40 fs [95]. The backing pressure of argon through the propylene oxide bubbler and nozzle was 30 PSI.

We present the resulting photoelectron spectra in two parts. As argon is an atom, and thus achiral, we can observe from its ionization the effects due to the shape of the chiral field. Then, we will look at the propylene oxide results to see if we can distinguish any effects due to the interaction of the chiral field with a chiral potential.

4.2.1 Field Based Effects

First, let's look at the raw results of the ionization of argon. The data are presented in two separate projections, in p_x vs p_y, which is the plane of the ω field, and in p_z vs p_y, which are the 2ω and major ω directions. Electron momentum plots from the ionization of argon are shown in Figures 4.4 and 4.5.

It is difficult to ascertain any significant differences between the spectra. As such, we turn to normalized differences. Recall, in such a plot, the value in a given pixel N_{ND} is given by

$$N_{ND} = \frac{N_1}{N_{1,tot}} - \frac{N_2}{N_{2,tot}}, \tag{4.4}$$

where N_1 and N_2 are the number of counts in that pixel in distribution 1 and 2, and $N_{1,tot}$ and $N_{2,tot}$ are the total number of counts in each spectrum. First, we present the normalized differences spectra between globally left/right, left/achiral and right/achiral fields in Figure 4.6. We focus on the data when S-propylene oxide was present.

Now we see that there are clear differences between the experiments. Looking at Figure 4.6, the ND spectrum for left and right fields in the p_x/p_y plane, we can see that ionization of argon yields more low momentum electrons when the field is left-handed, whereas higher momentum electrons along p_y tend to be produced from a right-handed field. Looking at the p_z/p_y plane, we see that the left-handed field produces more electrons with positive z-momentum, and a right-handed field yields more with negative z-momentum. The same pattern is produced when comparing left-handed with achiral fields in row (b), yet at about half the strength of signal. In the third row, a right-handed field is contrasted against an achiral one, and the distribution completely flips polarity, with a signal strength similar to (b). This pattern is qualitatively what we had hoped to see: left-right fields should be the largest difference, left-achiral should be about half the strength, and right-achiral should be an opposite sign but same magnitude distribution as left-achiral. The maximum PECD signal between left- and right-handed fields can be calculated using the formula discussed in Section 2.3, $2\frac{I_S - I_R}{I_S + I_R}$, where I_S and I_R are the intensity of the observables from the left- and right-handed fields respectively. This yields a maximum PECD of approximately 0.3% for a particular momentum value. Alternatively, integrating the total difference signal over all momenta gives a value of 13% for the differences between the left- and right-handed light, and approximately half that for each of the left-achiral light and right-achiral light.

Compared to other experiments shown in Section 2.3, whose PECD results tended to range between 1-10%, the value for a given momentum is comparatively low, but the overall signal difference between left- and right-handed fields is comparable. Ayuso *et al* originally proposed measuring the harmonic spectrum [87], where they see a large

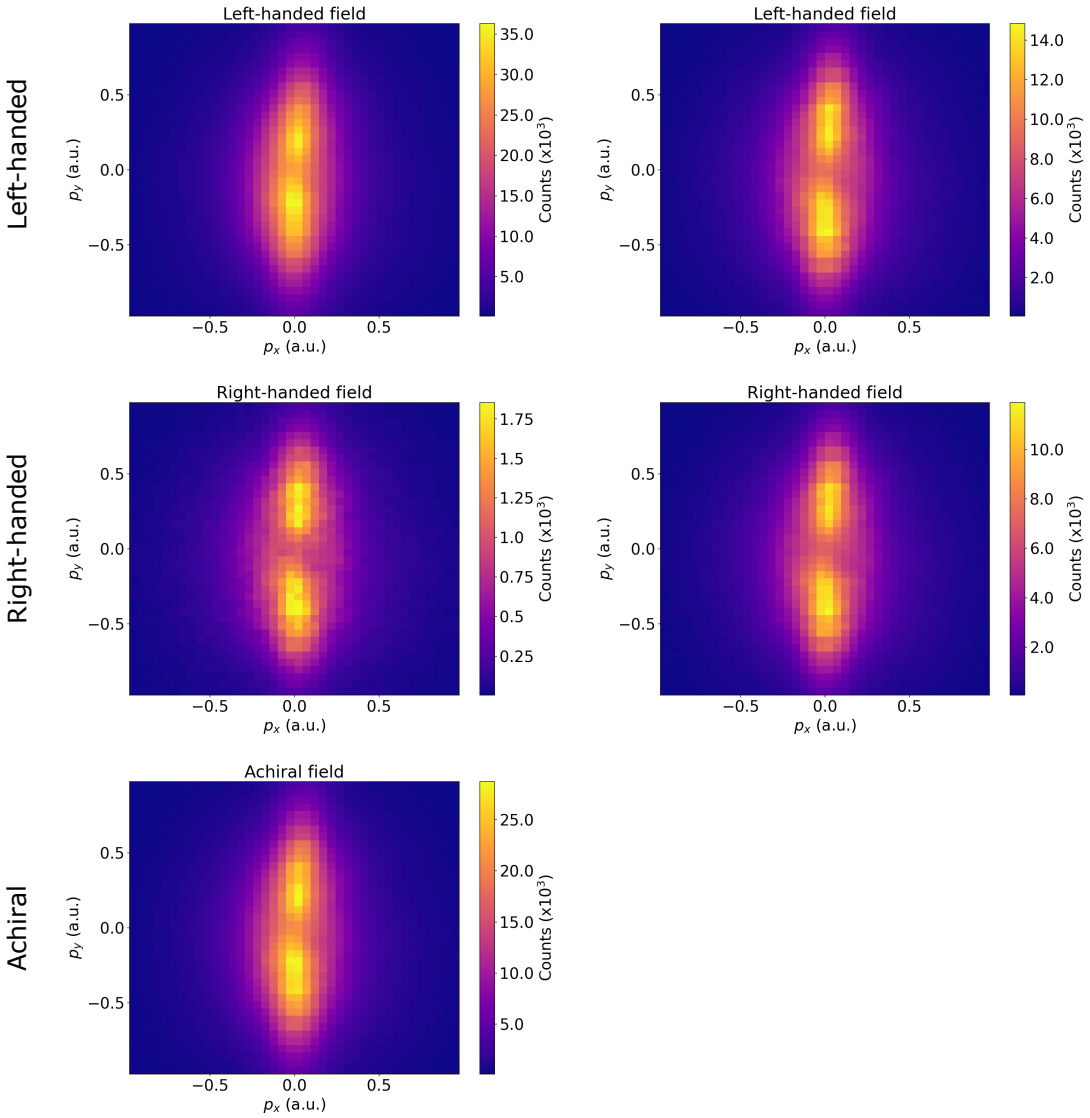

FIGURE 4.4: Raw electron momentum spectra in x and y from ionization of argon. Spectra are unique for globally left-handed, right-handed and achiral fields. The left column was measured with S-propylene oxide in the bubbler, and the right column with R-propylene oxide in the bubbler.

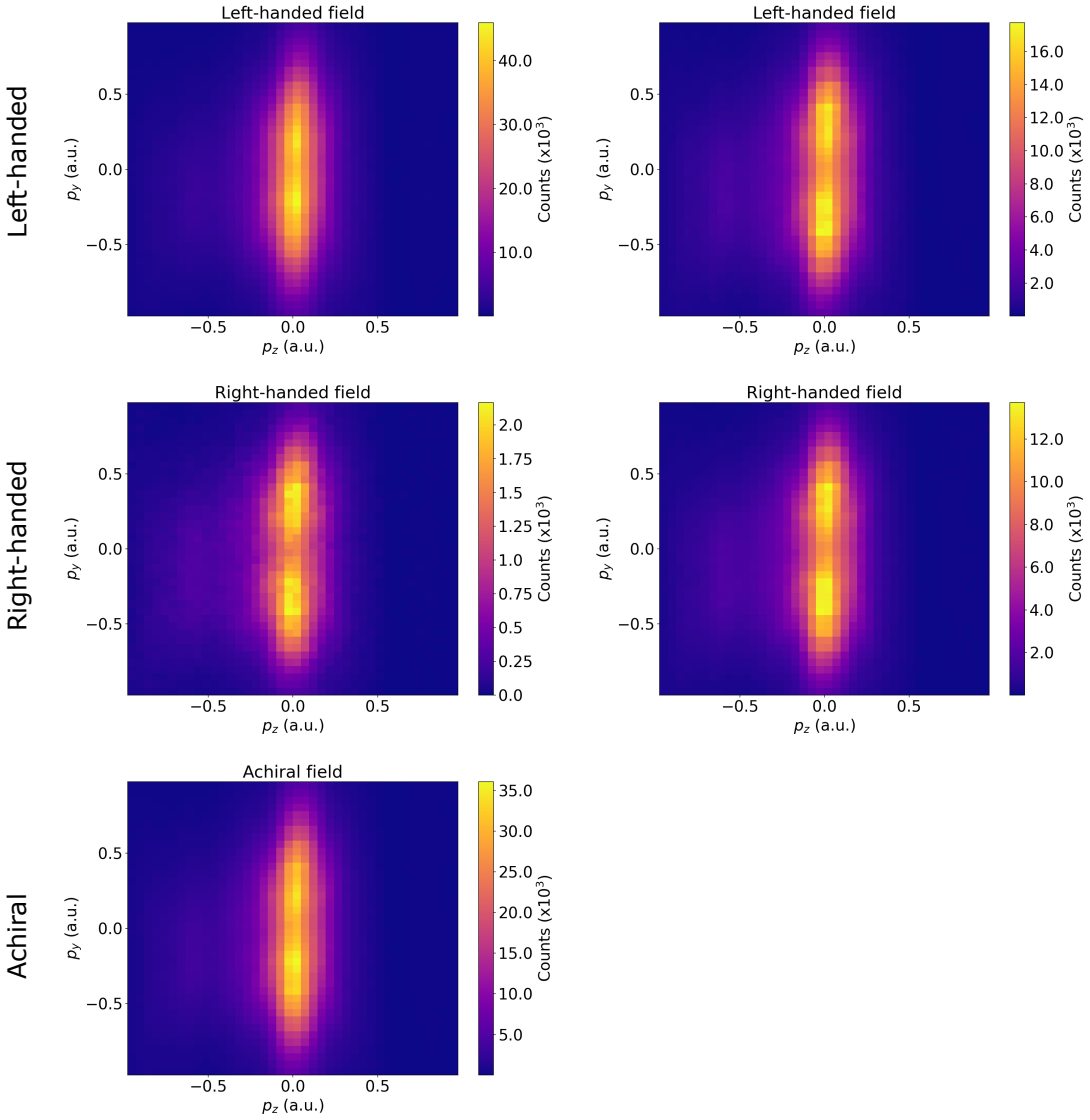

FIGURE 4.5: Raw electron momentum spectra in z and y from ionization of argon. Spectra are unique for globally left-handed, right-handed and achiral fields. The left column was measured with S-propylene oxide in the bubbler, and the right column with R-propylene oxide in the bubbler

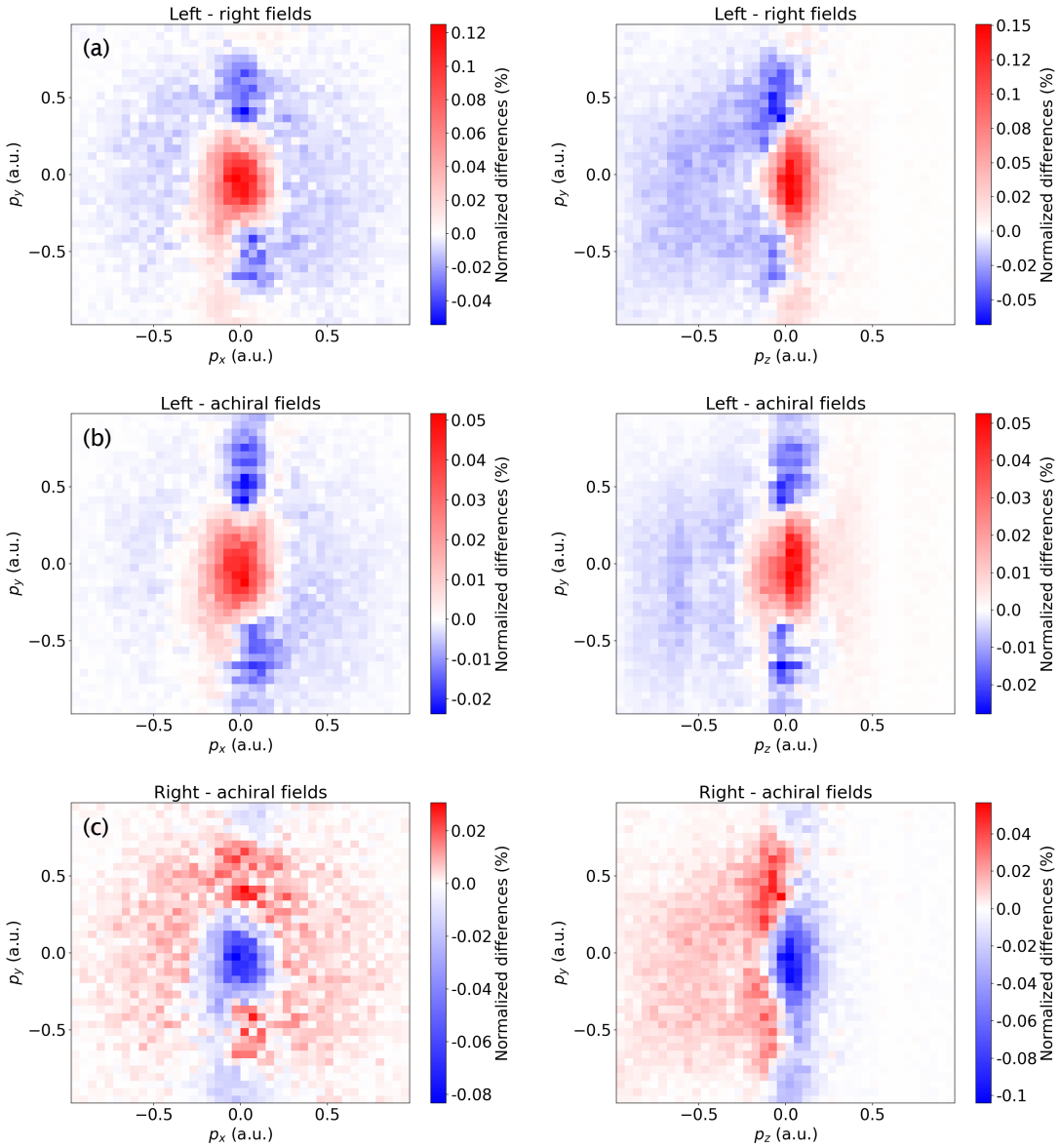

FIGURE 4.6: Normalized differences electron momenta for ionization of argon. The left column corresponds to the xy plane, and the right column the yz plane. Rows (a), (b) and (c) correspond to the normalized differences of left/right, left/achiral, and right/achiral fields respectively.

(200%) difference at particular harmonic orders, each of which can be detected separately from the others. In our experiment, we measure the entire electron distribution. As shown in our calculations in Figure 4.3, the inherent "strength" of chirality in this setup is generally low at most points across the focus, so there is no surprise that the chiral signal due to the field is considerably lower than 100%.

4.2.2 Enantiomer Based Effects

The next result we we will look at is the ionization of propylene oxide. The raw photoelectron spectra are very similar to that of argon, so they will not be shown again. Presented in Figure 4.7 are the normalized differences of the ionization of S-propylene oxide under globally left/right, left/achiral and right/achiral fields.

In this figure, we see the same qualitative patterns that we detected from the ionization of argon. In the ω plane, the left handed field still produces more low energy electrons, and the right handed field tends to generate those with higher momentum in p_y. In the p_z/p_y plane we see that the electrons favour a positive direction along z for the left-handed field, and a negative direction for a right-handed field. The pattern in signal strength remains similar; the left-right field differences yield the highest magnitude PECD, while the left-achiral and right-achiral give comparable strength but opposite sign signals. Note that while the left-achiral and right-achiral plots do not show the same magnitude in these plots, we will show that they have almost exactly the same chiral contribution in 4.3.

Next, we compare the ionization of S- and R-propylene oxide with normalized differences of globally left- and right-handed fields. It is in this data that we hope to observe effects based on the interaction of handed light with the differing enantiomers due to their chirality. We perform the same analysis on argon to act as a reference, as there should be no difference between the ionization of argon carrying S- and R-propylene oxide. The results are shown in Figure 4.8.

We observe that both the distribution of argon carrying R-propylene oxide and R-propylene itself display a similar pattern to their opposite enantiomer counterpart, including the sign of the pattern, unlike the results seen in Figure 4.7. As the R-carrying argon distribution is also qualitatively very similar to that of the R-propylene oxide, we must conclude that we cannot distinguish any enantiomer based effects. While the chiral signature of the field is clearly imprinted in the data, using the experimental photoelectron spectra from strong-field ionization is not a sensitive enough tool to differentiate enantiomers due to their chiral potential, particularly when there is a moderate strength PECD effect due to the field on its own. High harmonic generation and single photon techniques attempting to discriminate between enantiomers have the powerful

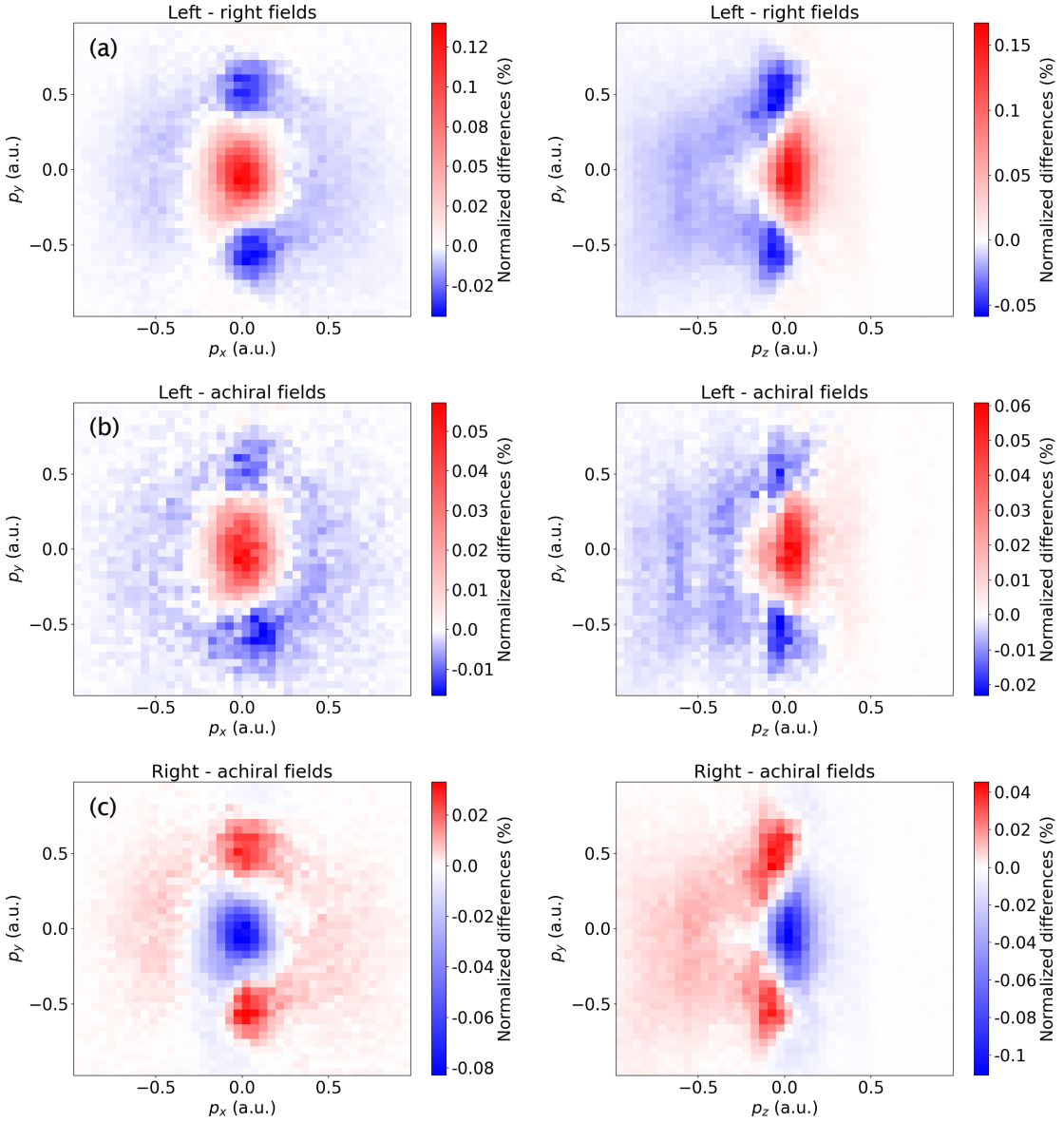

FIGURE 4.7: Normalized differences for ionization of S-propylene oxide. The left column corresponds to the xy plane, and the right column the yz plane. Rows (a), (b) and (c) correspond to the normalized differences of left/right, left/achiral, and right/achiral fields respectively.

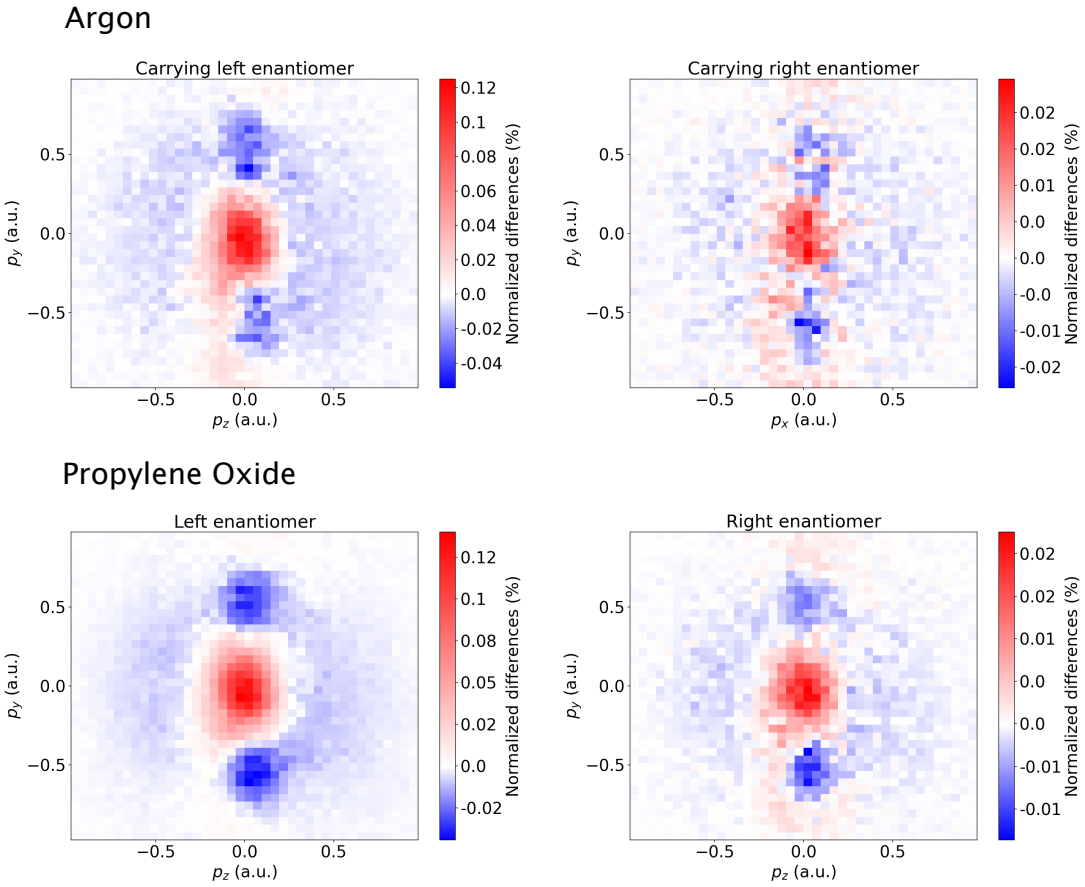

FIGURE 4.8: Normalized differences spectra for ionization under globally left- and right-handed fields. In the top row is ionization of argon carrying S- and R-propylene oxide, and in the bottom row is ionization of S- and R-propylene oxide itself. Only the xy projection is shown.

capability of probing discrete states, such as in [81] or [87]. This advantage is not afforded to strong-field ionization, which typically ionizes from the HOMO, a state which is diffuse in shape.

Considering the three step model of HHG, from our experiments we can distinguish a clear chiral signal from the propagation step due to the field, but none in the ionization step; the strong enantiosensitive signal seen in [87] must then largely be due to the recombination step.

It is worth noting that in our experiments, we are not trying to resolve any particular momentum value, but rather the overall qualitative character of the plots. The uncertainty of the momentum resolution is thus less important than the degree to which our experimentally generated fields conform to the theoretical ideal, determined by the focusing conditions, overlap, and general quality of the laser beam.

A simple improvement that may help with the quality of the chiral field we produce would be to increase the size of the input window of the COLTRIMS. As it stands in the present system, we were forced to use a 3:1 telescope to shrink the beam size to couple into our chamber without clipping the beam profile. Not only does such a telescope introduce difficult to control inhomogeneities in the far field, but shrinking the beam size also increases the size of the focal volume. If the focusing were tighter, the setup would admittedly be more difficult to align, but the resulting overlap signal would be considerably more clear when found, with a stronger chiral signal.

4.2.3 Fragmentation of propylene oxide

Thus far, we have performed our analysis solely on propylene oxide which is singly ionized and remains a single molecule. However, there are also many channels in which the propylene oxide can break apart which are common. In our data, there are four distinct fragmentation channels which are highly visible: CH_3^+, $C_2H_2O^+$, $C_2H_2^+$, and COH^+. A time of flight spectrum which highlights these channels is shown in Figure 4.9. We also briefly note that there are two distinct double ionization channels we could analyze, but the photoelectron distributions from these would not be particularly useful for our purposes.

We note that the ions in the $C_2H_2^+$ and COH^+ channel are very close in mass, and while each peak is visible, their broad distributions blend into each other in the time of flight spectrum. There has been work in the past which has used a specialty high-resolution spectrometer to resolve each peak individually [62], but unfortunately we are not able to separate them for our data. The ions from the CH_3^+ and $C_2H_2O^+$ channel, however, are clearly resolved, and we have performed the same normalized differences computation for the fragments as we have for the united molecule, which are inset in Figure 4.9. The same overall pattern may be observed as discussed in Section 4.2.1.

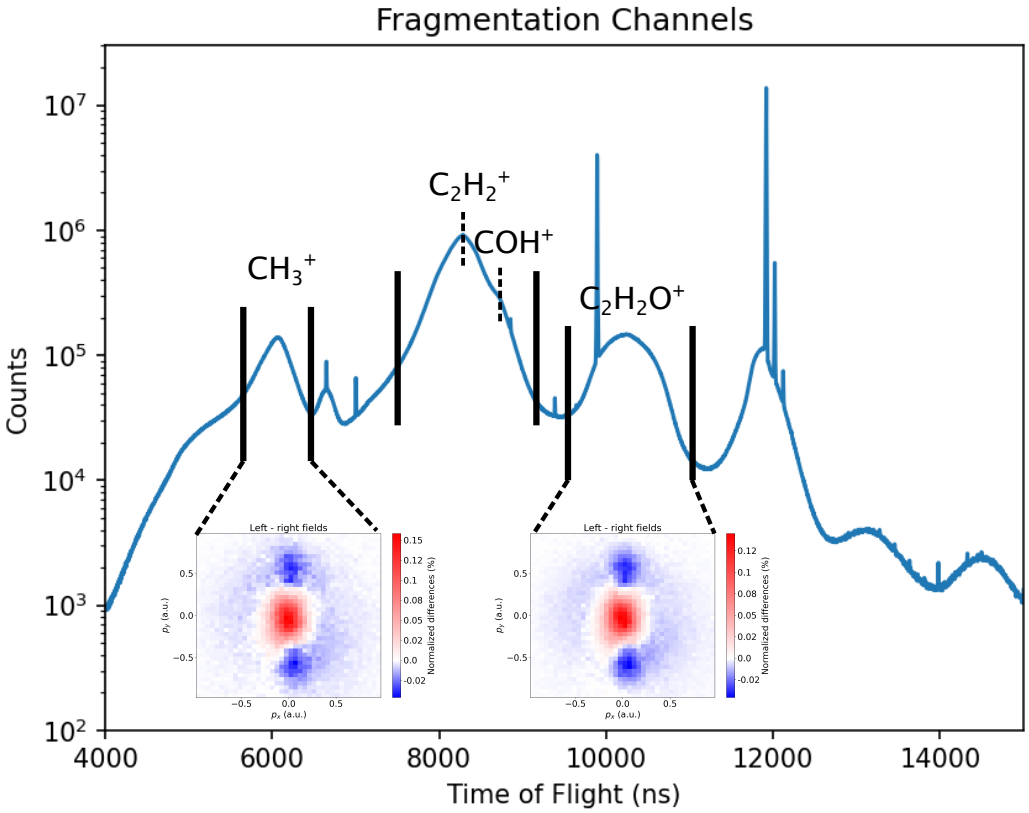

FIGURE 4.9: A time of flight spectrum, taken from the ionization of S-propylene oxide, where the fragmentation channels are labelled. Inset are the normalized differences between ionization under left- and right-handed light for both CH_3^+ and $C_2H_2O^+$.

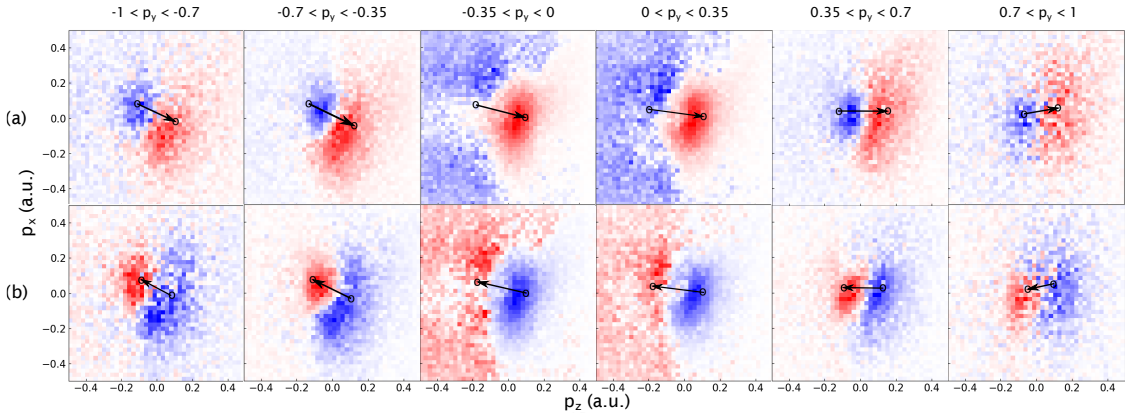

FIGURE 4.10: Electron momentum distributions in p_x and p_z projected onto slices of p_y. Row (a) corresponds to normalized differences of left-right fields, and row (b) corresponds to normalized differences of right-achiral fields. Values of p_y vary from -1 to 1 a.u, listed in columns. A black arrow is drawn pointing from the negative to positive centre of mass to aid the eye.

4.2.4 A three-dimensional chiral observable

Aside from looking for differences in the integrated 2-dimensional momentum distributions for different chiralities, it is interesting to ask if the 3-dimensional electron momentum distributions contain a directly observable chiral structure due to the chiral shape of the light field. In order to investigate this, we looked at the full 3-D structure of the electron momentum spectrum from ionization of S-propylene oxide. Since this is difficult to visualize directly, we projected the data along the main ω field axis onto the two minor field axes over six, non-overlapping intervals, i.e., intervals in p_y. We then take the normalized difference of the six p_x vs p_z distributions for two different chiral fields. The result is shown in Figure 4.10.

Looking at the normalized difference projections, we see that the biggest variation between the two experiments is a peak located just off the p_y axis at p_x and $p_z = 0$. A circle is drawn at the centre of mass of the negative and positive differences for each plot, and an arrow pointing from negative to positive helps aid the visualization of the rotation. We see that the peaks rotate about p_y as the value of p_y increases. This twisting of the electron distribution about the axis is a chiral observable of its own, almost reminiscent of the twisting of circularly polarized light as it propagates. Comparing row (a) with row (b), we see that while the pattern retains the same handedness, the negative and positive centres of mass are on opposite sides of the p_y axis.

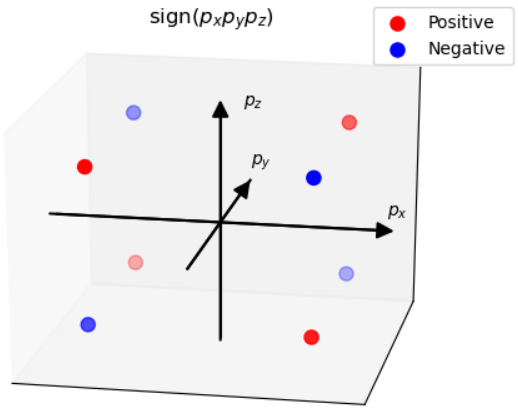

FIGURE 4.11: A demonstration of the sign of each quadrant when computing the chirality measure χ.

4.3 Chiral Coefficient

While analyzing the results of this experiment, it became apparent that we needed a tool that can characterize the "degree of chirality" of a photoelectron distribution. We have developed a chiral measure which can be calculated from a given spectrum [93].

We define a chiral coefficient χ as

$$\chi = \iiint P(p_x, p_y, p_z)\text{sign}(p_x p_y p_z) dp_x dp_y dp_z \,, \tag{4.5}$$

where $P(p_x, p_y, p_z)$ is the probability of a given electron momentum, and $\text{sign}(p_x p_y p_z)$ assigns each quadrant a positive or negative value, which is demonstrated in Figure 4.11. Note that a cyclic permutation of x, y, z will yield identical results.

A similar formulation can be given as

$$\chi = \iiint P(p_x, p_y, p_z) p_x p_y p_z dp_x dp_y dp_z \,, \tag{4.6}$$

where here the contribution of higher momenta electrons is more heavily weighted given the inclusion of $p_x p_y p_z$, which obviously has the same sign as $\text{sign}(p_x p_y p_z)$. Since the overall PECD is small in our case, we choose not to use this formulation, as random fluctuations with large momentum in the experimental data get magnified, but for higher chiral signal, this may well be a more appropriate choice.

Before getting to any results, it is worth discussing the visual style we will use to display them first. Rather than plot the data in all dimensions, we collapse this down

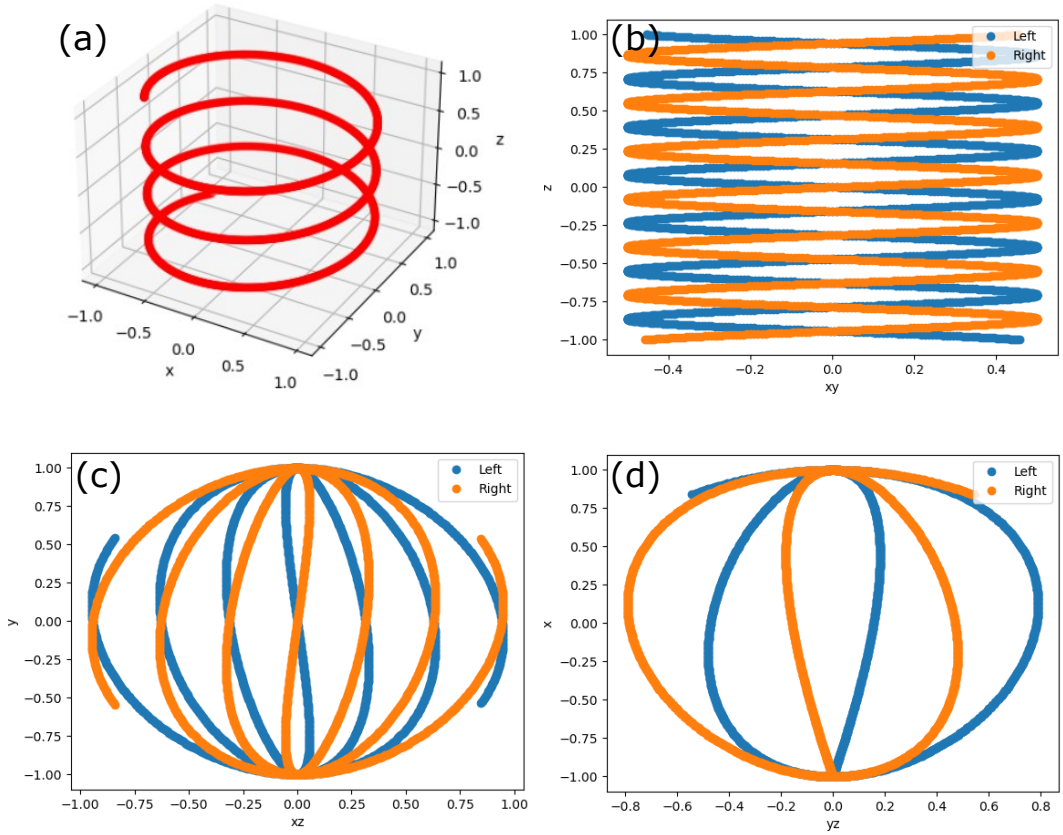

FIGURE 4.12: The propagation of a particle in a simple chiral trajectory, a spiral, shown in (a). In (b), (c), and (d), the position is plotted in two dimensions by collapsing one axis to a product: z vs xy, y vs xz and x vs yz respectively. Each plot shows the results from both a left- and right-handed spiral.

to a more visually accessible two by presenting the product of two dimensions on one axis, such as p_y vs $p_x p_z$. An example of this style is demonstrated in Figure 4.12, where the propagation a particle in a spiral (a simple chiral system) is shown.

In this simple example we see that a left- and right-handed spiral can be distinguished in each plot, regardless of which axes are the product. Of course, electron momentum data will not be as simple, but we will see that this style of plot is quite suitable. Computing χ using this approach is straight forward: the counts in the first and third quadrant are summed, and those from the second and fourth quadrant are subtracted.

To verify the validity of the proposed coefficient χ, we use the results of a three-dimensional semi-classical simulation, along with the experimental results. The simulation will be discussed first.

The photoelectron spectrum was calculated for Ar under six differing electric fields with varying phase conditions. Cases 1 and 4 correspond to globally left-handed light, 2 and 5 to right-handed light, and 3 and 6 to achiral light. The differences between cases

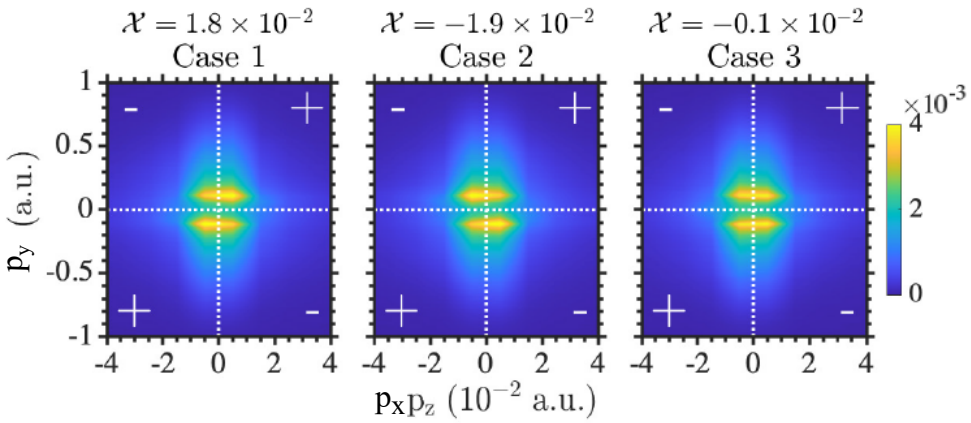

FIGURE 4.13: Results of three-dimensional semi-classical simulations on Ar, shown as probability distributions for an electron to ionize with momentum p_y and product $p_x p_z$. Cases 1, 2 and 3 correspond to left, right and achiral ionizing fields respectively. The chiral measure χ is listed for each case.

1, 2, 3 and cases 4, 5, 6 are the relative phase of ω and 2ω in each arm, choosing a vector potential shaped like a figure eight and a potato chip respectively, as seen in Table 3.1. Since the simulations are performed on an achiral medium, the resulting χ is due to the field only.

If the measure χ is robust, it should yield opposite signs for ionization under opposing handedness of light. Similarly, the spectrum from an achiral field should give little to no signal. The results of the simulation for cases 1-3 are shown in Figure 4.13. Note that the plots are in the form p_y vs $p_x p_z$ as discussed previously.

We see that the obtained values of χ are 1.8×10^{-2}, -1.9×10^{-2} and -0.1×10^{-2} for left-handed, right-handed, and achiral fields respectively. Upon close inspection, it can be seen that this is largely due to two lobes which are shifted towards positive p_y and $p_x p_z$ values and negative p_y and $p_x p_z$ values in the left-handed case. These are seen reflected in the p_y axis for the right-handed case. The presence of these lobes is not seen in the achiral case, explaining why $\chi \approx 0$.

Additionally, we can look at a similar measure for the normalized differences between cases, χ_d, which can help highlight areas of interest. The results are displayed in Figure 4.14. This value is a sanity check on the robustness of χ; we expect that the differences in the left and right hand cases be largest in magnitude, and that the differences between left/achiral and right/achiral be roughly equal in magnitude with opposite sign.

The value of χ_d is 3.7×10^{-2}, 1.9×10^{-2}, and -1.8×10^{-2} for panels a_1, a_2, and a_3 respectively, meeting the expected trend once again. It can be seen for the left-right case that each quadrant has a large contribution to the overall signal, whereas for the left-achiral and right-achiral distributions, the signal mostly comes from negative p_y and

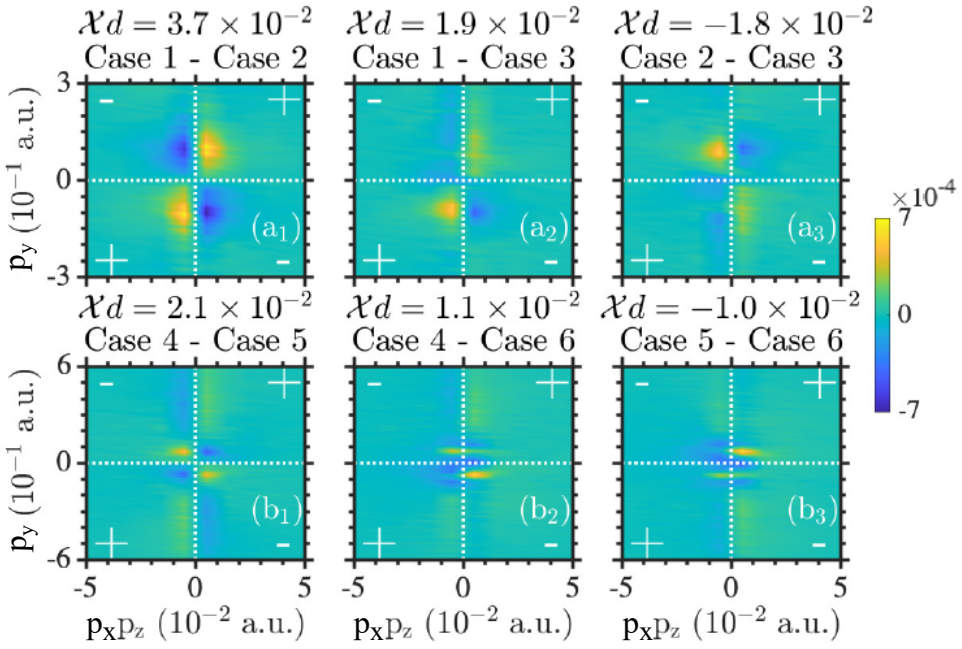

FIGURE 4.14: Normalized differences of the simulation results for left-right, left-achiral, and right-achiral fields, labelled a_1, a_2, a_3 and b_1, b_2, b_3 respectively. Panels (a_i) and (b_i) have the same handedness, but different vector potential, yielding a different probability distribution. The chiral measure χ_d is displayed in each case.

positive p_y respectively. Panels b_1, b_2, and b_3 have χ_d vales of 2.1×10^{-2}, 1.1×10^{-2}, and -1.0×10^{-2}. While the overall values are smaller for this vector potential, they follow the same trend as the previous.

Next, we look at the experimental data. The distribution of electron momenta p_z vs $p_x p_y$ for left, right and achiral fields, as well as the normalized differences are presented in Figure 4.15,

As before, we see that looking at the raw distribution of momentum does not show any obvious differences as field handedness varies, and the computation of χ gives ≈ -0.025 for each case. The next logical step is to try looking at the normalized differences instead. The χ_d values for the experimental normalized differences still do not demonstrate the same trend as the simulation. This may be rationalized by considering the experimental values of p_x. The momentum spread is broad in the y-direction, but very narrowly distributed around 0 in the x-direction. This causes the bulk of the distribution in these plots to collapse to 0 on the $p_x p_y$ axis. We attempt to circumvent this issue by performing a simple rotation of the photoelectron spectrum about the z-axis (which as we know, cannot change the chirality inherent in a system). The effect of this rotation of the three-dimensional momentum distribution in steps of 15° is shown on a p_z vs $p_x p_y$ distribution in Figure 4.16.

As we can see from panels (a)-(g), this causes the distribution to lift off the $p_x p_y = 0$

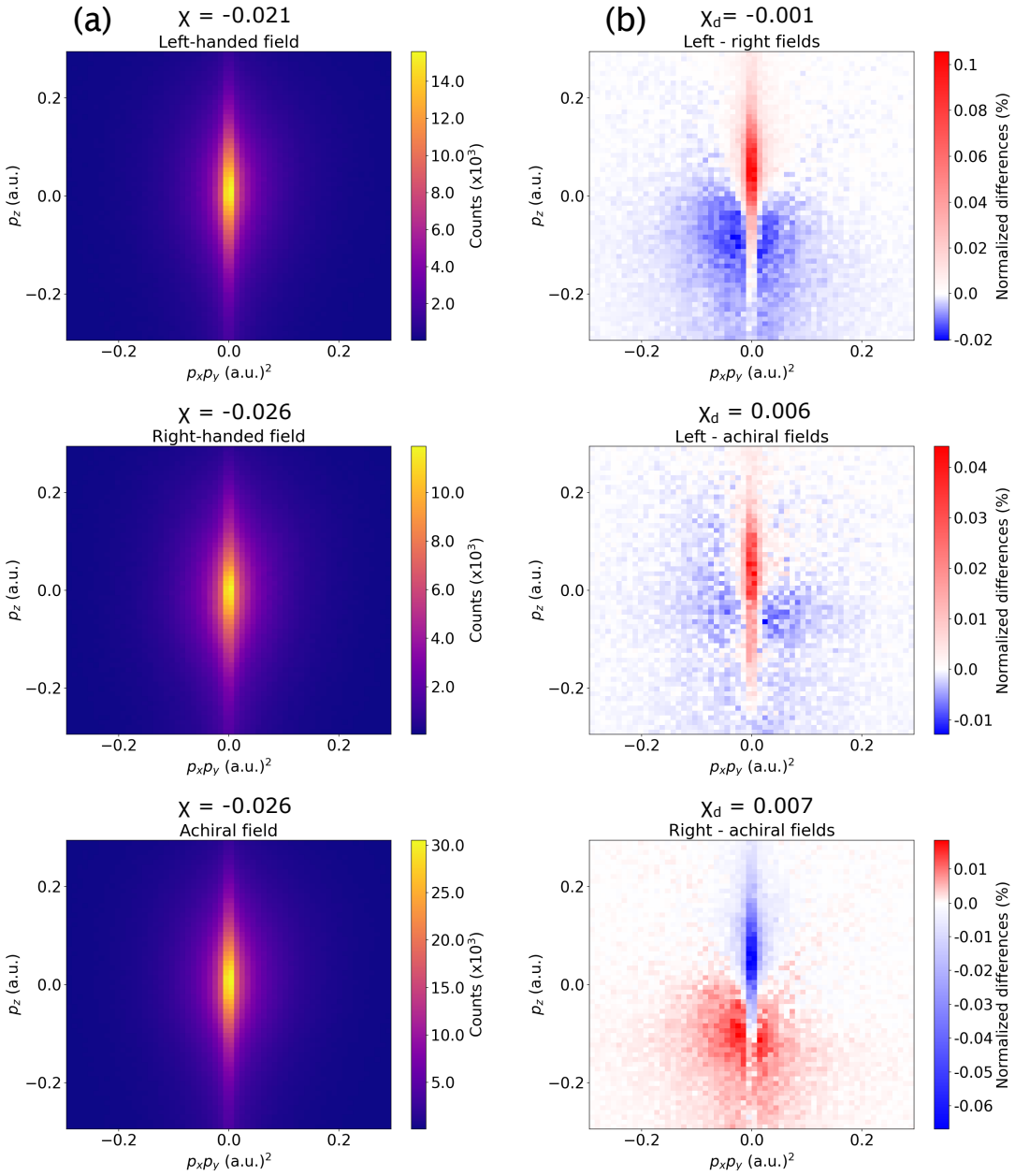

FIGURE 4.15: Experimental electron momenta distribution for p_z vs $p_x p_y$. Left, right and achiral light cases are labelled in column (a), with the measure χ shown for each. Normalized differences for each of these plots are labelled in column (b), with the value of χ_d shown for each plot

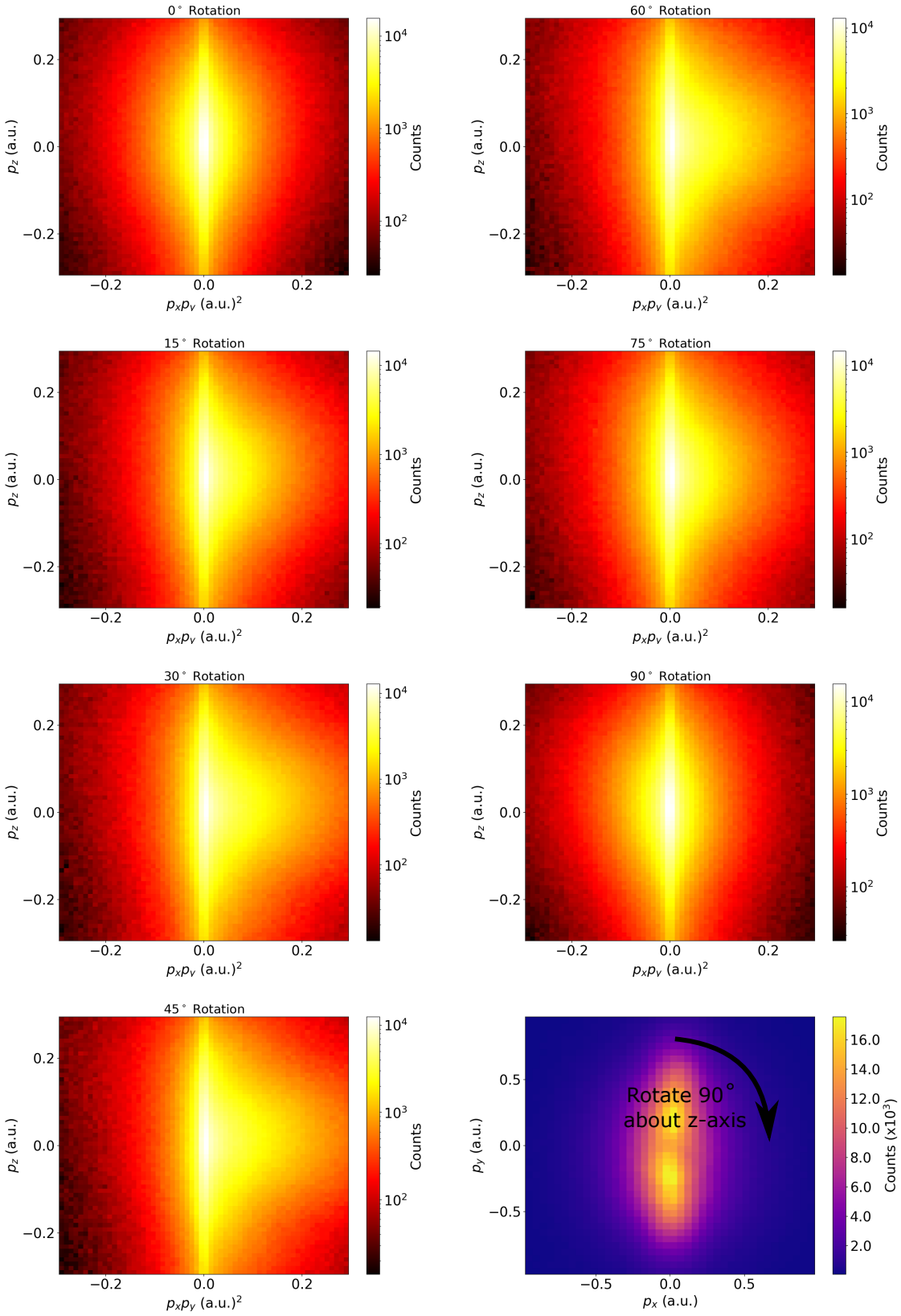

FIGURE 4.16: Panels (a)-(g) show the electron momenta distribution p_z vs $p_x p_y$ when rotated by the indicated angle about the z-axis. Panel (h) demonstrates such a rotation in the xy plane.

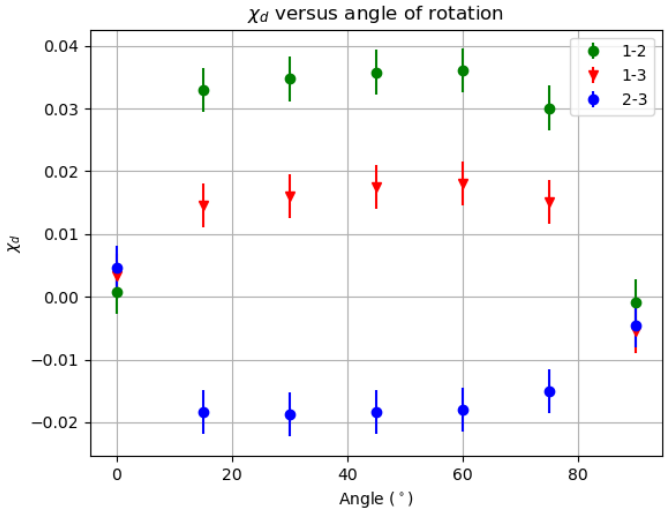

FIGURE 4.17: The value of χ_d plotted against the angle of rotation about the z-axis. Left-right data is shown in green, left-achiral in red, and right-achiral in blue.

line, with the effect maximized at 45°. If we recompute χ_d for each of these steps, we get the results displayed in Figure 4.17.

We see that for any rotation value where the distribution is not entirely centred on $p_x p_y = 0$, we see the expected trend for χ_d. The magnitude of the left-right fields gives the highest value, and the left-achiral and right-achiral fields yield values with similar magnitude yet opposite sign, indicating an equal contribution to the chiral signal. This further supports the evidence that χ is a robust measure, and indeed that the experimental results are valid.

4.4 Enantioselective Yield

One particular result that has yet to be shown using optical chiral techniques is the ability to influence the yield of one enantiomer compared to another. For example, if during our COLTRIMS experiments, we demonstrate that S-propylene oxide is preferentially ionized by a given pulse, we would be able to take a racemic mixture and adjust its composition towards the R- enantiomer.

Measuring the ionization yield of a particular enantiomer under given conditions is actually a surprisingly complicated task, even when using COLTRIMS. It is, of course, not possible to simply measure the ionization statistics from a racemic mixture, since we cannot distinguish the two enantiomers. Thus, the only tactic is to measure ionization from an enantiopure solution and compare. We do this for the usual three pulse conditions: globally left-handed, right-handed and achiral light.

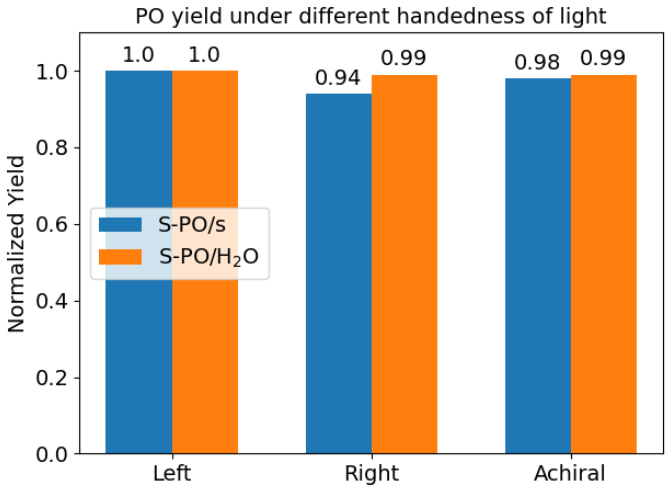

FIGURE 4.18: S-Propylene oxide yield for three quick experiments, designed to have near identical conditions. Data is presented normalized to left-handed light, and for each of propylene oxide per second and propylene oxide per background H_2O.

The biggest complication in such a measurement is the endeavour to keep conditions as identical as possible over time and across experiments. As such, we attempted two different experimental paradigms looking for ion yield, independent from the previously shown data. First, we performed three quick, successive measurements with different handedness of the light field. Each run lasted approximately 20 minutes, aggregating on the order of 200,000 electrons ionized from propylene oxide for each field handedness. The second attempt involved switching between each handedness of light field every 10 seconds, and running for a significantly longer period of time. In this fashion, we were able to collect on the order of 10,000,000 counts for each handedness. However, the laser intensity and gas density were not completely stable over the course of the experiment. In this approach, these long term experimental fluctuations are affecting each measurement equally.

The results of each measurement are presented in Figures 4.18 and 4.19 respectively. The short experiment was performed on S-propylene oxide only, as changing enantiomers takes the better part of a day, and we would not get identical conditions for the R-propylene oxide measurement. The longer, rotating version was performed on both enantiomers. As a sanity check, the data is presented in two fashions: propylene oxide counts per second, and propylene oxide counts per measured background H_2O. The first depends on fluctuations in both gas density and laser intensity, while the second depends almost exclusively on gas density. In the scenario where we measure an enantioselective yield, I believe that both should agree in trend. All values are normalized for easy viewing so that ionization under the left-handed light for either situation

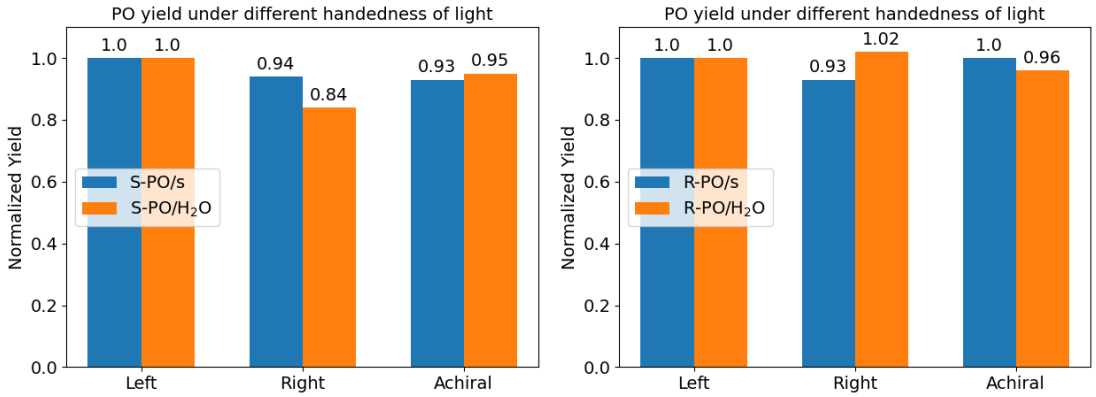

FIGURE 4.19: Propylene oxide yield for a single experiment with switching handedness, designed to collect high statistics under over long term experimental fluctuations. Data is presented normalized to left-handed light, and for each of propylene oxide per second and propylene oxide per background H_2O. The left hand panel shows S-propylene oxide, and the right R-propylene oxide.

is unity.

The first analysis on the first experiment performed gave the blue bars in Figure 4.18, which shows the exact trend we would hope to see. Similarly handed light enhances ionization, opposite suppresses, and achiral is somewhere in the middle: even a 6% difference would be huge. A sober second thought demanded further analysis: the data per background is practically constant. Further evidence was needed, so a second experiment was attempted.

Similarly to previous, the orange bars for S-propylene oxide in Figure 4.19 gives the desired trend in the longer experiment, but an even stronger yield difference of 16%. However, in this experiment, counts per second were not in agreement. Indeed, the R-propylene oxide data was likewise unhelpful and worse: no successful trends could be seen. We conclude that we cannot show evidence of consistent enantioselective yield in ionic propylene oxide.

4.4.1 Fragment yield

As we have discussed in 4.2.3, single ionization of propylene oxide with no subsequent breakup is not the only interesting channel of ionization; we also have statistics on the four fragmentation channels, in particular, that of CH_3^+ and $C_2H_2O^+$. In order to report on the yield of these channels in a self consistent fashion, we will only include statistics in which both a CH_3^+ and $C_2H_2O^+$ have been detected in coincidence, in other words, a double ionization. In this way, we can exclude any channel in which CH_3^+ is produced in a 3(+) fragment breakup. The first step to analyzing fragmentation in COLTRIMS is to look at an ion time of flight coincidence plot, as seen in Figure 4.20.

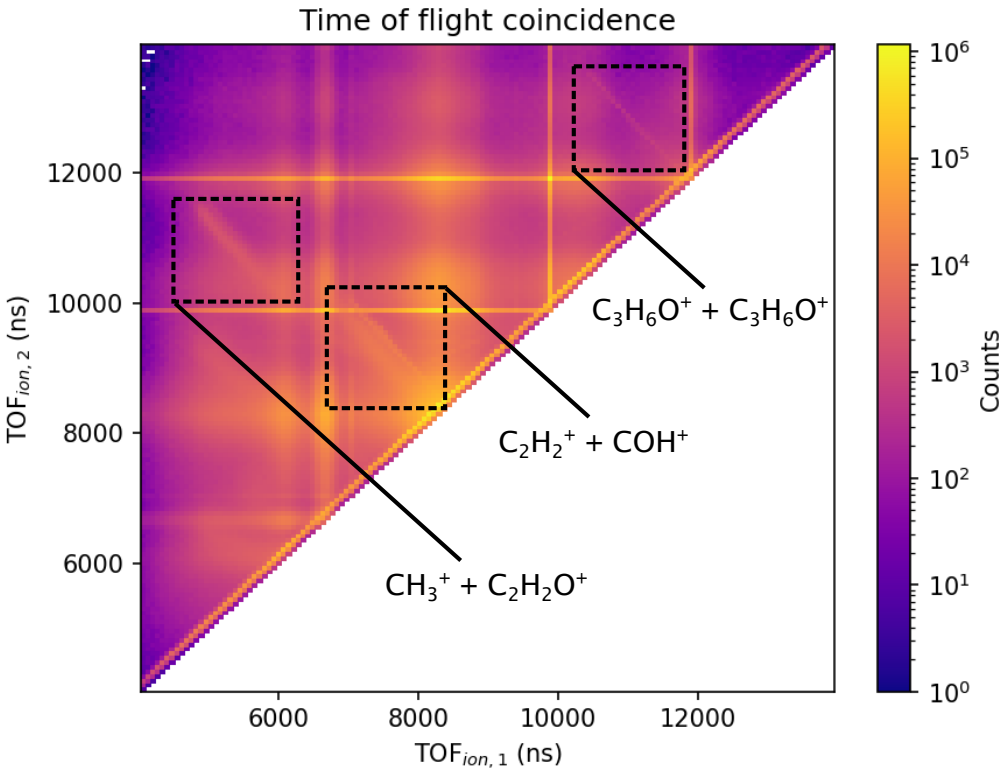

FIGURE 4.20: A photoion-photoion coincidence plot. The time of flight of the first detected ion is displayed on the x-axis, and the time of flight of the second detcted ion is displayed on the y-axis. Relevant channels with Coulomb explosion due to double ionization of fragments are shown in black boxes.

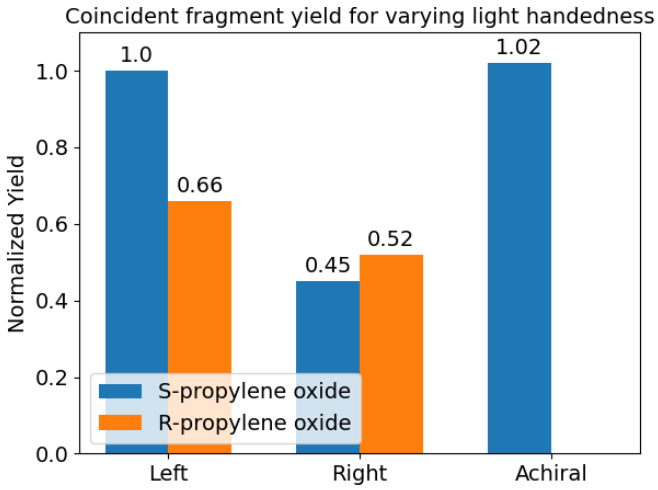

FIGURE 4.21: Number of coincident CH_3^+ and $C_2H_2O^+$ fragments per second during ionization of S- and R-propylene oxide under globally left-handed, right-handed, and achiral light. Data is normalized to fragment counts per second of ionization of S-propylene oxide under left-handed light.

The x-axis corresponds to the time of flight of the first ion detected in a coincidence, and the y-axis the second; the plot has no data under the $y = x$ line because the ions are defined strictly by timing. Any horizontal or vertical patterns in this plot do not provide useful information, as they correspond to incidental coincidences with background ions. We look specifically for the curved lines indicated in the black boxes. These patterns correspond to Coulomb explosions leading to fragmentation, the exact makeup of which we can determine by the time of flight. In this particular experiment, we see 3 different coincidences: the one we are interested in analyzing, CH_3^+ and $C_2H_2O^+$, a blurred double pattern due to the nearly equal mass of $C_2H_2^+$ and COH^+, and a faint line due propylene oxide dimers. We may further refine the data to look solely at events pertaining to CH_3^+ and $C_2H_2O^+$ in coincidence by restricting momentum conditions in the analysis, looking for events with a high relative momentum due to the Coulomb explosion, but low centre of mass momentum.

The statistics generated for fragments detected in coincidence are significantly lower than either the single ionization of propylene oxide or an ionized fragment on its own. As such, we analyze the largest data set for fragment yield information, which is the data shown in 4.2. We present the number of fragments produced per second for S- and R-propylene oxide under globally left-handed, right-handed, and achiral fields in Figure 4.21. The data is normalized to the fragment counts per second of ionization of S-propylene oxide under left-handed light for convenience.

For S-propylene oxide, we see a substantial difference between the number of fragments for ionization by left- and right-handed fields, although the achiral field generates

approximately the same number as the left-handed field. A decrease is also shown for R-propylene oxide going from left- to right-handed light. While the differences in some cases are quite dramatic, it is difficult to draw a consistent conclusion from this data. Despite this, for both the fragmentation data and the single ion data shown in Section 4.4, we retain a positive outlook that this avenue might bear fruit given further study.

We suggest two potential future avenues for study to improve the yield measurements, attempting to ameliorate fluctuations in laser power and gas density. Firstly, were a 100 kHz laser system to be installed, we could collect statistics in COLTRIMS ten times faster than we currently do with our 10 kHz system. Reducing experimental time from the current 24 hours to just over 2 hours would significantly reduce the long scale laser fluctuations in power, and shorter runs such as the 20 minute experiment designed to keep fluctuations low would collect vastly increased statistics. To improve gas density consistency, we could switch to a larger nozzle, which would reduce the effects of clogging. A second refinement would be to use a more sophisticated, commercial bubbler, which can heat the liquid more effectively and have a larger reservoir than what we used.

Chapter 5

Conclusion

"Don't adventures ever have an end? I suppose not. Someone else always has to carry on the story."

Bilbo Baggins

Chirality is an incredibly important concept in the realm of biology and pharmacology. Despite having identical chemical compositions and practically the same physical properties, enantiomers can display wildly differing effects *in vivo*. Over the past twenty years, physicists have been playing an ever more active role in furthering the study and characterization of chiral molecules and effects, due to the increasing utility of optical techniques. As an ultrafast optical scientist, it has been my privilege to continue this endeavour; it is no exaggeration to state that the study of chirality is both in our DNA and in our hands.

In summary, this thesis has told the story of a synthetically chiral ultrafast optical experiment. The theory behind ultrafast physics has been introduced, followed by an overview of past chiroptical techniques. Of particular importance in this revision was the development of many recent theoretical advancements designed to drastically improve overall chiral signal, including the one used experimentally in this body of work. Next, a detailed explanation of the experimental method used to create and sculpt the necessary laser pulses was given, as well as how to measure the resulting observables. Finally, the results of the experiment were shown and discussed.

We have seen that a synthetically chiral pulse scheme can induce field-based photoelectron circular dichroism in strong-field ionization, although we could not present evidence of an enantiomer-specific response in this regime. We have identified a three-dimensional chiral signature in the overall photoelectron distribution, and developed a new chiral measure that can characterize the degree of chirality of such a distribution. Finally, we have discussed the ionization yield of both propylene oxide and its fragmentation channels.

Improvements to our method may be adapted in future experiments with this setup, potentially increasing the chiral response in photoelectron spectroscopy or enantioselective yield. A larger input window to COLTRIMS would allow for tighter focusing and an increased chiral signal. For yield measurements, a higher repetition rate laser would vastly decrease the error due to laser power fluctuations, and a more sophisticated bubbler could help deal with gas density fluctuations.

Previous to this work, there had been no experimental evidence to support the groundbreaking theory published in recent years. While the overall chiral signal measured in this experiment was modest, comparable in magnitude to many of the previous results discussed in this thesis, it represents a proof of principle that synthetically chiral techniques are valid, and may be achieved in the lab.

The outlook for further research regarding such novel chiral techniques is better than ever. There are current efforts underway to perform the identical experiment as proposed in Ayuso *et al*'s original synthetic paper [87], which will naturally produce a higher chiral signal by virtue of measuring the high harmonic spectrum rather than photoelectrons. More recently published theoretical methods such as [89] or [88] are more simple in principle, and are ripe for experimental plucking by other ambitious scientists.

Appendix A

Spatiotemporal imaging of valence electron motion

A.1 Introduction

When a system is excited or ionized into a state with multiple nearly degenerate energy levels, a quantum beating will occur with a frequency proportional to the energy separation of those levels. The wavepacket oscillates in character between the two orbitals, rapidly changing distribution on a fs timescale. This has been termed a spin orbit wave packet.

A spin orbit wavepacket was first demonstrated experimentally in a transient absorption measurement by Goulielmakis *et al* in 2010 [96]: first, Krypton was ionized by an ultrashort attosecond pulse. Then, the absorption of a secondary infrared pulse is measured as a function of their delay. The result is a striking resonance in cross section at 6.3 fs, corresponding to a beating between the energy levels of the $^4P_{1/2}$ and $^4P_{3/2}$ states.

There have since been several attempts to use molecular imaging techniques such as COLTRIMS measurements to actually show the changing character of an ion's HOMO. These have largely been unsuccessful, until 2019 when Kubel *et al* [97] persevered. The main issue with previous attempts was that on the time scale of measurement (recall that the oscillation is on a fs timescale), it is extremely difficult to distinguish electrons that have been ionized from the neutral and those ionized from the cation! We demonstrated a surprisingly simple technique to differentiate the two, allowing clear momentum imaging of the oscillation in orbital character.

A.2 Experimental Setup

As seen in Figure A.1, the experiment is composed of 3 pulses. First, a few cycle 800 nm z-polarized pump pulse arrives to ionize argon, causing the generation of a spin orbit wavepacket between the $^2P_{1/2}$ and $^2P_{3/2}$ states. This wavepacket oscillates with a

period of 23.3 fs, and changes character from $m = 0$ (peanut shaped) to $m = |1|$ (donut shaped). A second identical few cycle 800 nm probe pulse arrives some variable time later to further ionize the cation. The key to our method is to use a third, mid-IR 40 fs, x-polarized deflection pulse overlapped with the probe to streak the momentum of this second election.

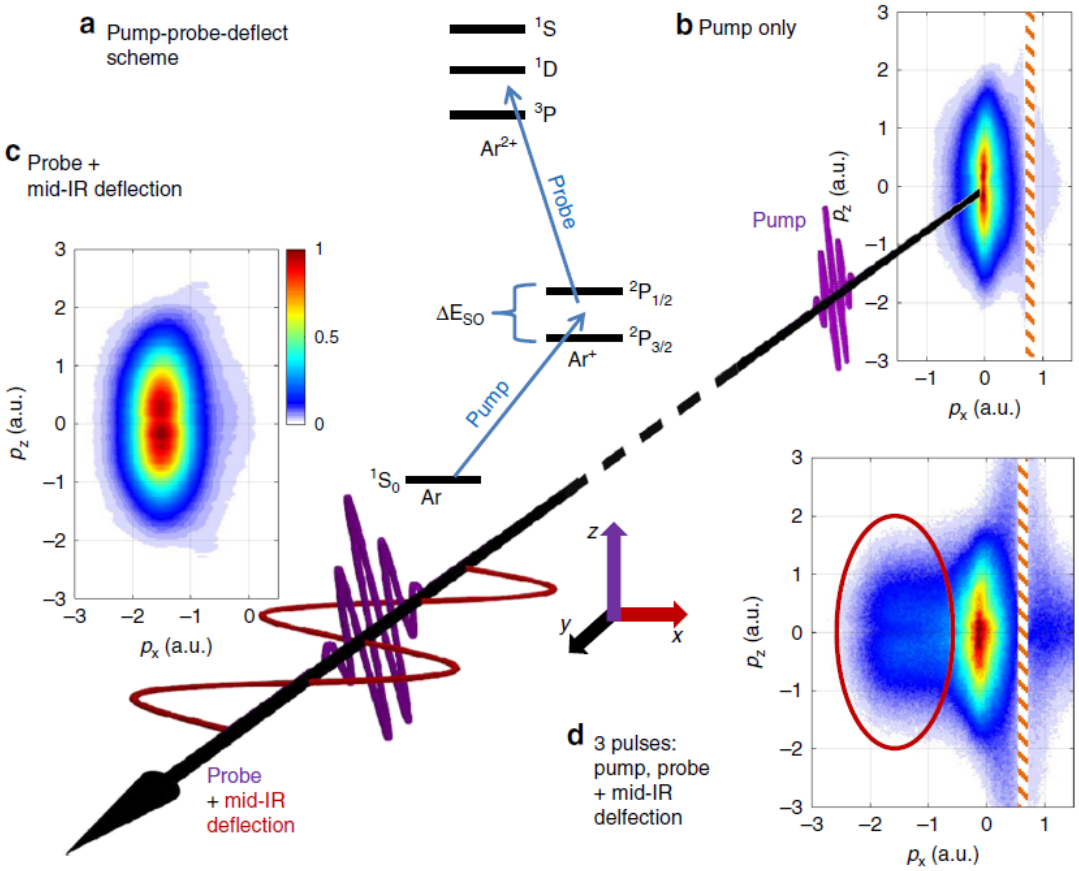

FIGURE A.1: A schematic of the pulses used to measure a spin orbit wavepacket in argon. The excitation scheme is inset, where a pump pulse ionizes neutral Ar into the $^2P_{1/2}$ and $^2P_{3/2}$ states, causing a beating. A probe pulse further ionizes the cation. A third deflection pulse gives momentum to the second electron only. Panels (b),(c) and (d) show the momentum spectra of ionization from the pump, probe and deflection, and all three pulses respectively.

The spectra shown in A.1 (b),(c), and (d) explain the concept. In (b), the electron spectrum from ionization with just the pump pulse is displayed. As there is no extra external influence, the distribution is centred along $p_x = 0$. Panel (c) gives the electron momentum spectrum from ionization with the combination of probe and overlapped deflection pulses. The longer duration mid-IR pulse causes little ionization, but gives electrons momentum in the x-direction. Since the probe pulse is short, the ionization occurs largely at the peak of this pulse, and the streaking momentum is mostly constant.

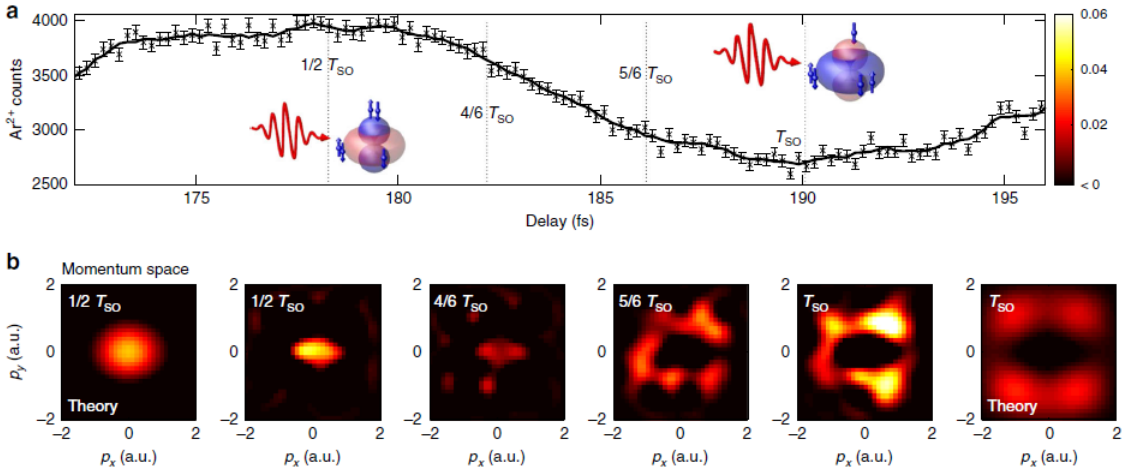

FIGURE A.2: Shown in (a) is the Ar^{2+} yield as pump/probe delay varies. The yield maxima correspond to ionization mostly from the $m = 0$ orbital, while at the minima, ionization is largely from the $m = |1|$ state. Panel (b) displays electron density plots in momentum space for times $1/2\ T_{SO}$ to T_{SO}. The left and rightmost plots are theoretically calculated distributions at $1/2\ T_{SO}$ and T_{SO}.

For this particular timing of probe and deflection pulses, the distribution is centred on $p_x = -1.5$ a.u. The overall distribution from ionization of all 3 pulses is shown in (d), which includes electrons ionized from both neutral Ar and the Ar^+ cation. We may select electrons largely ionized due to the probe pulse from the cation by including only those in the indicated red ellipse, which have been streaked by the deflection pulse.

A.3 Results

The experimental results are shown in Figure A.2. Panel (a) shows a strong modulation of count rate as the delay time between pump and probe pulses is varied. Ionization is favoured when the $m = 0$ state is populated, when the light is polarized parallel to the peanut distribution. At the yield minima, ionization from $m = |1|$ is more significant. Displayed in (b) is a series of measured electron density plots for times $1/2\ T_{SO}$ to T_{SO}, with theoretically calculated spectra for $1/2\ T_{SO}$ and T_{SO} on the left and rightmost sides respectively (where T_{SO} is the period of the spin orbit oscillation). The experimental results are in excellent agreement with the theory, and the oscillating character of the orbital can be seen clearly.

Indeed, this measurement can be extended to three dimensions. Shown in Figure A.3 are the normalized differences of each projected two-dimensional momentum distribution measured at maximum and minimum Ar^{2+} yield. Panel (a) shows the experimental results, and (b) calculated distributions based on an a simple imaging model.

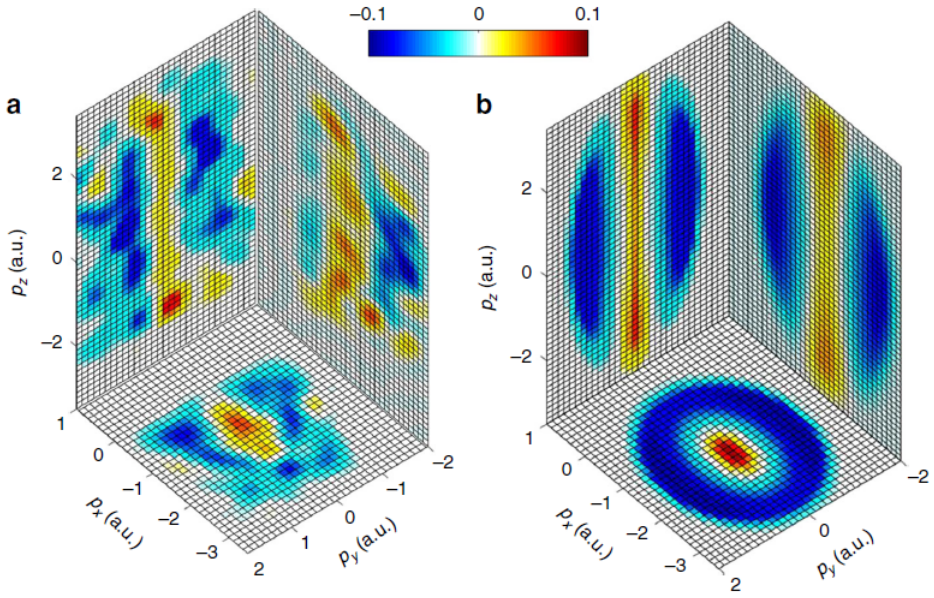

FIGURE A.3: Three-dimensional normalized differences between the momentum spectra recorded at the maximum and minimum Ar^{2+} yields. The data in each plane is integrated over the third dimension. Panel (a) shows the experimental data, while (b) shows modelled distributions.

While a very simple technique in principle, these results offer exciting prospects for future time-resolved molecular imaging experiments. Examples of potential post-ionization dynamical measurements that have been unlocked include charge migration and correlated electron-nuclear dynamics.

Appendix B

Probing multiphoton light-induced molecular potentials

B.1 Introduction

In the discussion of the dissociation dynamics of H_2^+ thus far, we have treated its potential energy surface as one-dimensional, as shown in Figure 2.11. As we have seen in the Floquet picture, light can distort a potential surface depending on its frequency and intensity, which we can call a light-induced potential (LIP). The angle between the polarization of this light and the molecular axis adds a second degree of freedom to the energy structure, and directly affects dissociation dynamics. The consequences of this angle dependence have largely been unexplored; the structure of H_2^+ is an ideal first candidate to do so, as it can be considered a two-level system, composed of the lowest electronic states σ_g and σ_u. In this work [41], we use both theory and experiment to show that LIPs can result in strong angular modulation of the ion yield.

B.2 Results

Examples of two different LIP energy surfaces on H_2^+ can be seen in Figure B.1, calculated by solving the 2D time-dependent Schrödinger equation (2D TDSE). The first case, shown in (a), uses 685 nm light at an intensity of 3×10^{13} W/cm^2. A single photon crossing is seen, with a lineout along the internuclear distance R at this polarization angle θ in (b) highlighting the crossing at the dashed line. In the second example, (d), 2300 nm light at the same intensity is used; here, multiphoton transitions are more relevant. The landscape is significantly more complex, showing 1,3, and 5 photon crossings. A lineout along the internuclear distance, displayed in (c), shows 1,3,5, and 7 photon crossings, indicated by the dashed lines.

In order to experimentally investigate the surfaces seen in Figure B.1, we used the pump-probe setup depicted in Figure B.2. An intense, few-cycle pulse centred at 730 nm

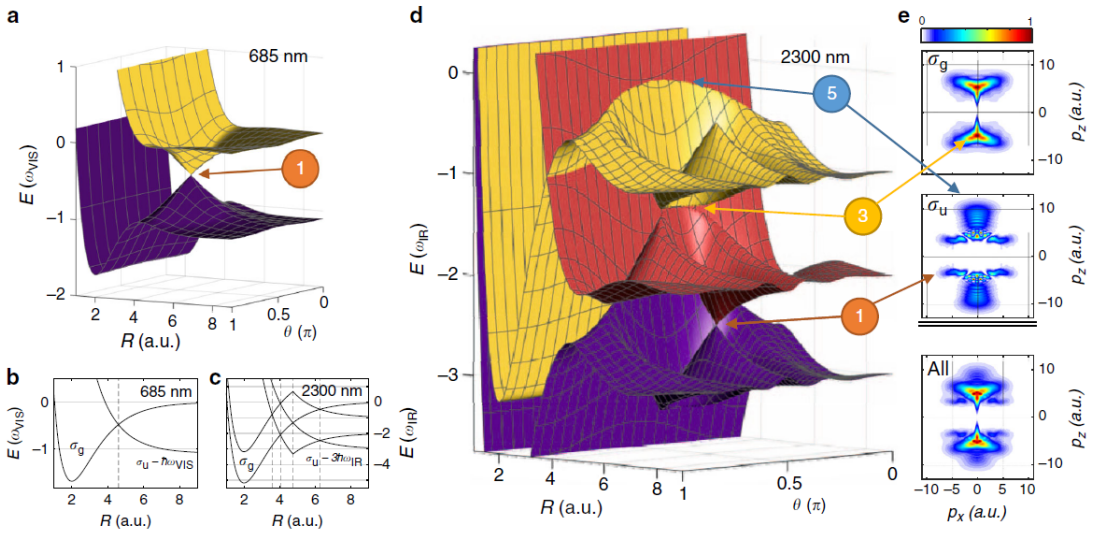

FIGURE B.1: Calculated light-induced potential surfaces of H_2^+. Panel (a) shows the landscape for absorption of 685 nm light, displaying a single photon intersection, whereas (d) shows the landscape for 2300 nm light, including intersections involving the absorption of 1, 3, and 5 photons. Seen in (b) and (c) are lineouts from each respective case, where the dashed lines show a single photon crossing for 685 nm, and 1,3,5, and 7 photon crossings for 2300 nm. The proton momentum distribution from the 1,3, and 5 photon absorption pathways, as well as all combined are shown in (e).

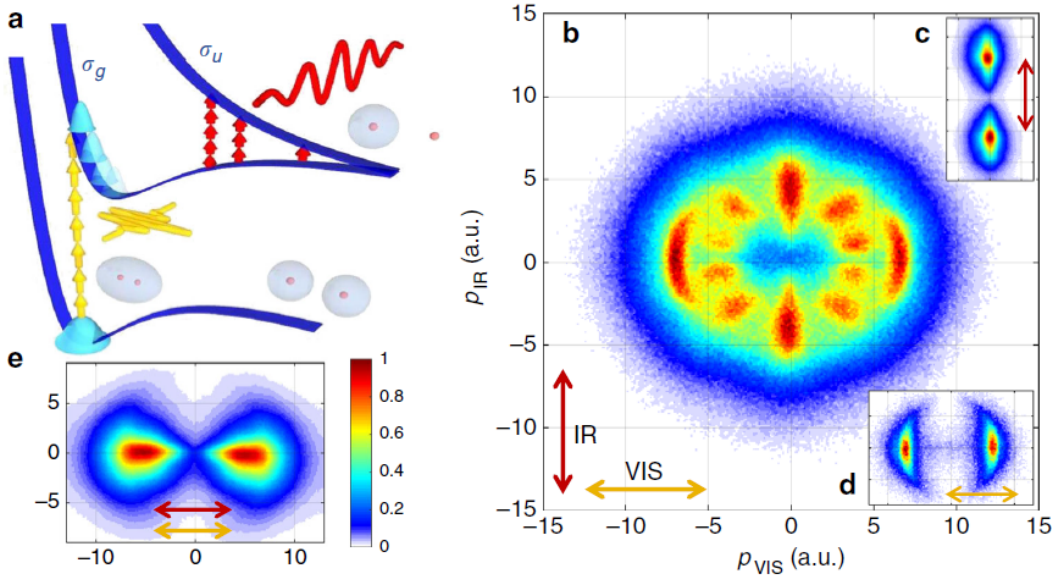

FIGURE B.2: Panel (a) shows the experimental setup; an intense visible pulse ionizes H_2, and a perpendicularly polarized mid-IR pulse prompts the molecule into a dissociative pathway. Shown in (b) is the overall proton momentum spectrum, whereas (c) and (d) show ionization from only the pump and probe pulses respectively. The proton momentum distribution is shown in (e) for parallel polarization of pump and probe.

was used to ionize H_2, producing a bound wavepacket in H_2^+ with a nearly isotropic distribution with respect to the laser polarization. Next, a moderately intense, perpendicularly polarized 2000 nm pulse created the LIP surfaces on which the dissociation of H_2^+ occurs. This dissociation occurs along their initial alignment direction unless rotational dynamics arise. The resulting three-dimensional momentum spectrum of protons and electrons are measured in coincidence in a COLTRIMS system. The proton momentum along the visible and infrared axes is shown in (b), and displays a striking difference between that of the momenta spectrum of ionization from just the infrared pulse, (c), and just the visible pulse, (d). Panel (e) shows the proton momentum distribution if both pulses are oriented in parallel, which resembles the results from the infrared pulse only. This indicates that the complex angular structure seen in (b) must be polarization dependent.

To determine the cause of this angular structure, the 2D TDSE was solved with both pulses taken into account. To determine whether rotational dynamics are the specific cause, two such calculations were performed, one where rotation was artificially switched off, and one where rotation is fully taken into account. The results can be seen in Figure B.3 (a) and (b). We see that even with no rotation, there are still pronounced angular modulations in distribution. Allowing the rotational dynamics shows that they do influence the momentum spectrum, where large differences are highlighted by the

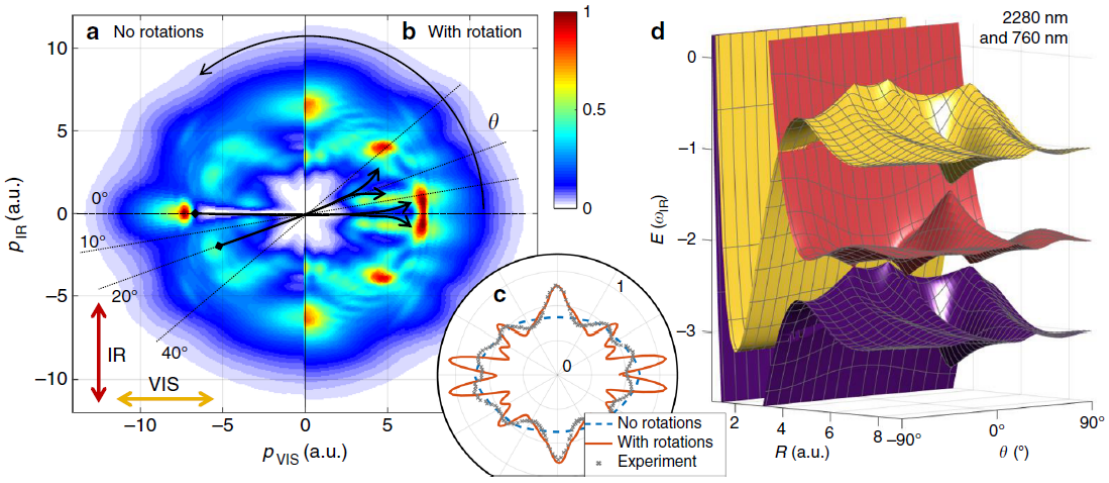

FIGURE B.3: Results of 2D TDSE simulations are shown in (a) with rotational dynamics artificially switched off and (b) with full dynamics. Black arrows point out major differences between the two. An angular lineout displays the results compared to experiment in (c). Panel (d) shows an example two-colour light-induced potential landscape for H_2^+.

black arrows. This means that rotational dynamics play a significant but secondary role in defining the final momentum! A direct comparison between simulated and measured results is shown in (c); only the rotation enabled results give the strong modulations seen in experiment.

To further investigate the picture, two-colour Floquet theory was used to compute LIPs. The laser field is given as $F(t) = \sqrt{I_{vis}}\cos(\omega_{vis}t + \phi_{vis})\hat{x} + \sqrt{I_{IR}}\cos(\omega_{IR}t + \phi_{IR})\hat{z}$. The resulting energy surface landscape is dependent on the relative phase between the two pulses $\Delta\phi = \phi_{vis} - \phi_{IR}$; shown in Figure B.3 (d) is an example for $\Delta\phi = 0$, but in general, both experimental and numerical results are integrated over $\Delta\phi$.

This analysis was able to determine the reasoning behind the emergence of angular structure in proton momentum distribution, even in the absence of rotational dynamics. In short, as the alignment angle of the molecular axis θ increases, so do the field components relative to the molecular axis, as $F_{vis} \propto \cos(\theta)$ and $F_{IR} \propto \sin(\theta)$. This causes Floquet state crossings to open and close as θ is varied, leading to the pronounced angular dependence. As a specific example, at $\theta = 0°$, the effect of the mid-IR field is negligible, and dissociation occurs as in the single colour case. But, as θ increases, a new channel is opened due to single photon coupling by the mid-IR field, which competes with the previous channel, moving population to the peak seen at $\theta = 10°$. We name this process angle-dependent channel switching.

In general, this work has shown how complex LIP landscapes determine the direction of molecular dissociation, using H_2^+ as an example. Our approach, both numerically and experimentally, can be used to begin studying reaction dynamics in other

more complex molecules.

Appendix C

COLTRIMS Software Guide

In this appendix, I will present a brief tutorial of software and files that are relevant for controlling data acquisition using the COLTRIMS computer. This section will largely be aimed at a user who is new to using the system, and should by no means be considered a complete discussion. It is organized into two sections, one which covers files needed by the Cobold software, and a second which looks at the bane of sanity, the delay stage.

C.1 Cobold

Shown in Figure C.1 is the user interface of the Cobold software. Data acquisition can be started by executing the appropriate Cobold Command File (ccf) using the button in the yellow box. You may cycle between plots by pressing plus or minus on the number pad, or by typing v # in the command line. By default, there are a number of spectra enabled which are extremely helpful for calibrating the experiment, such as time of flight, time of flight vs x and y, x vs y, and delay stage position. The buttons highlighted in the red box will re-scale or update the spectrum, and the one in the blue box empties the spectrum of all previous counts.

In general, Cobold is capable of performing a number of valuable live analysis operations via its command line which I will not cover here. A perusal of the manual, found under the help menu, is recommend for further ideas (or as Andre would say, RTFM).

The histograms which are displayed in Cobold may be edited by adjusting the histograms_minimum.ccf file, which can be seen in Figure C.2. To add your own, add a line with the following information: for 1D, "try define1 minimum, maximum, bin size, axis name, none, condition name (always if no condition), name of plot" and for 2D, "try define2 minimum1, maximum1, bin size1, axis name1, minimum2, maximum2, bin size2, axis name2, ...".

In particular, a useful control factor for these histograms are the conditions, which are defined in histograms_conditions.ccf. This file is displayed in Figure C.3. A condition defines a range of values which will be displayed in a plot, and may be combined

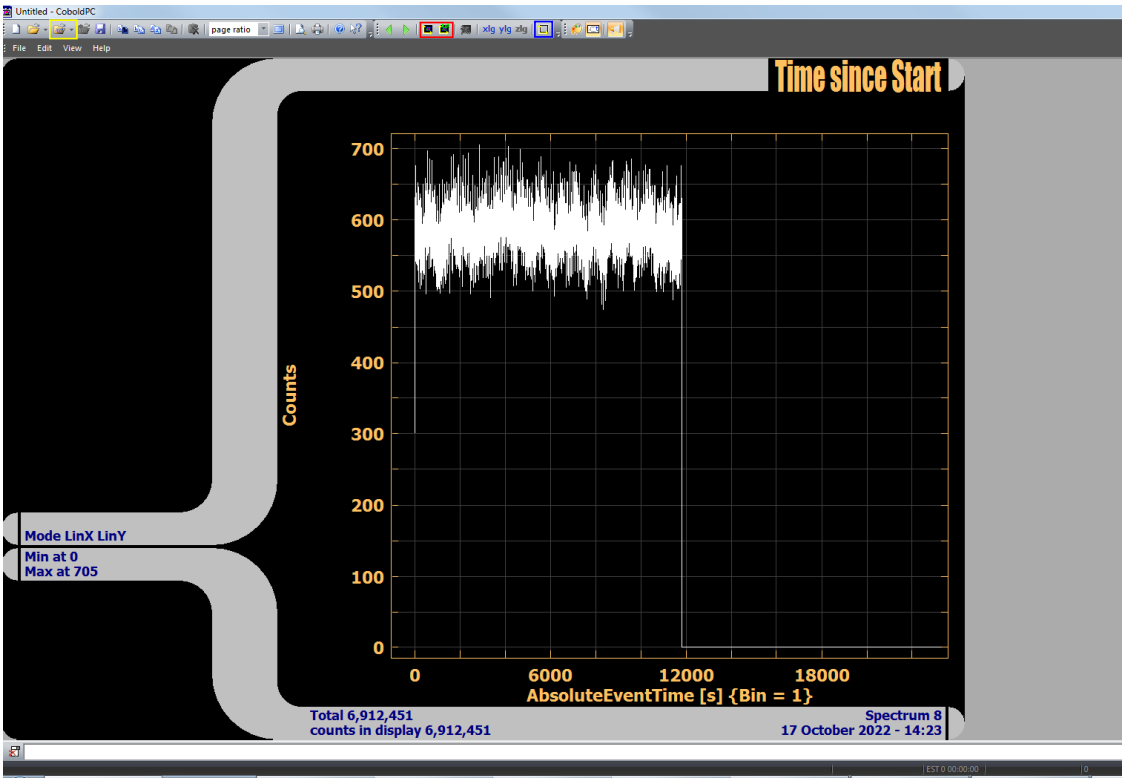

FIGURE C.1: The Cobold software user interface. Various control elements are displayed in yellow, blue and red boxes. The command line at the bottom can be used to execute analytical operations.

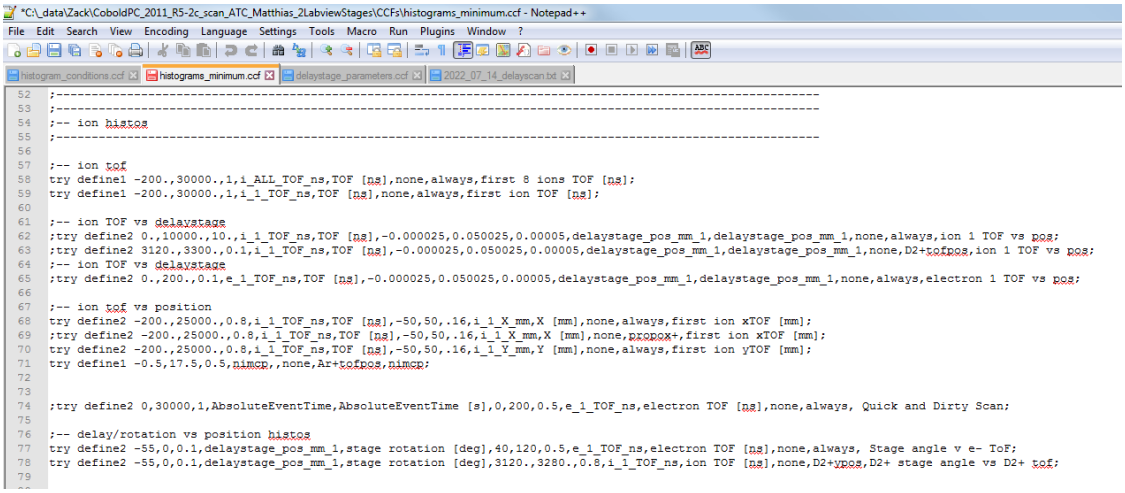

FIGURE C.2: The file histograms_minimum.ccf. In this file, the histograms displayed in Cobold are defined and given parameters.

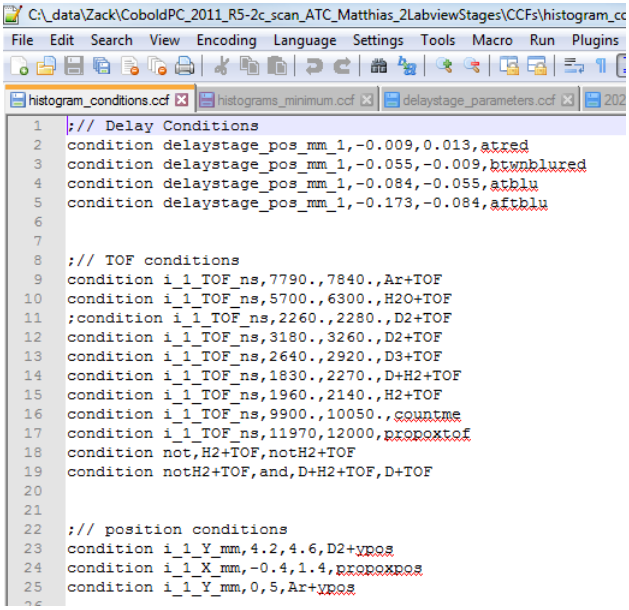

FIGURE C.3: The file histograms_conditions.ccf. Contained within are the definitions of conditions which can restrict the data shown in histograms in Cobold. Conditions may be combined with logical operators.

with logical operators such as in lines 18 and 19. The syntax in general is "condition variable, min value, max value, condition name". Defining a plot with a condition can be extremely helpful to make sure you are looking at only the statistics you are interested in, for example from a particular ion and dissociation channel.

C.2 Delay Stage

The first file that needs to be edited to work with a delay stage is delaystage_parameters.ccf, which can be seen in Figure C.4. For delay stages that plug into the Newport ESP300, which is most commonly used in our setup, the top parameters are used. Of particular importance are parameters 400-402, which define the number of delay stages to record data from, the COM port the delay stage is physically plugged in to, and the program ID that the delay stage will follow. Parameters 403-406 and 411 needn't be changed in general. If a delay stage is not part of the setup, or you wish to test without running the delay stage program, parameter 400 should be set to 0.

If Micronix stages are to be used, parameters 420 and 421 must be filled in as well. The current method to control Micronix stages is to use a Labview program, meaning the stage is connected to a commanding laptop, which is then in turn connected to the COLTRIMS computer. This can be difficult to set up: communication will not be possible unless the correct COM settings have been chosen. Screenshots of these settings are

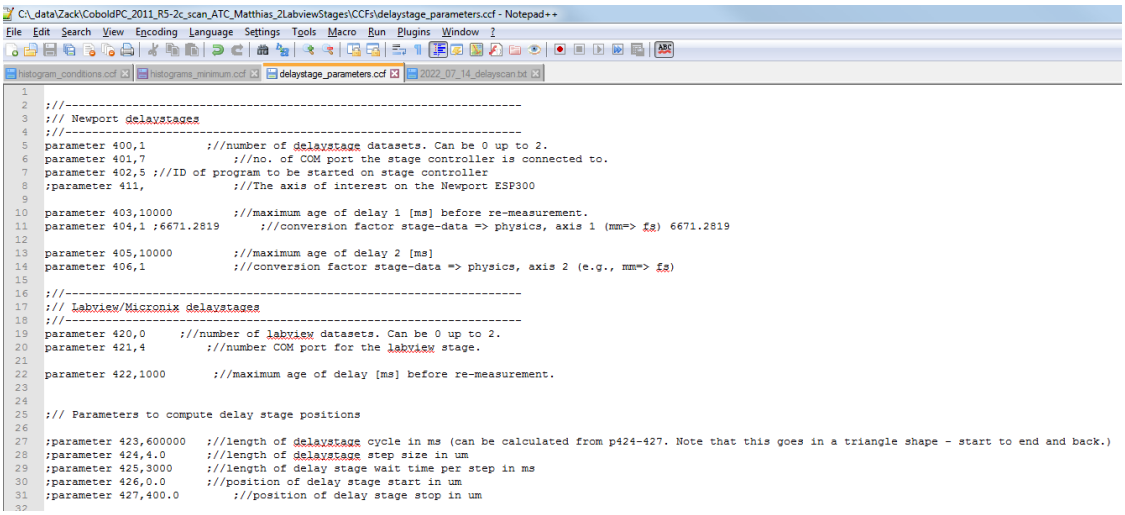

FIGURE C.4: Parameters pertaining to controlling a delay stage, found in delaystage_parameters.ccf. The top half controls a stage connected to a Newport ESP300, whereas the bottom half a Micronix stage connected to Labview.

saved on the COLTRIMS computer desktop for both Newport and Labview/Micronix stages.

For Newport stages, control is achieved through writing a program in the ESP300 language. An example is given in Figure C.5.

Written in plain English, this code reads:

- 5EP: Enter program with ID # 5
- 3WS: Wait for all activity on stage axis 3 to stop
- 3DL: Begin a loop with label 3
- 3VA10.0: Set the absolute velocity of stage axis 3 to 10.0 mm/s
- 3PA-0.7025: Set the absolute position of stage axis 3 to -0.7025 mm
- 3WS: Wait for all activity on stage axis 3 to stop
- 3VA0.05: Set the absolute velocity of stage axis 3 to 0.05 mm/s
- 2DL: Begin a loop with label 2 (this loop is nested due to the previous one)
- 3PR0.002: Move the stage on axis 3 0.002 mm forward relative to previous position
- 3WS: Wait for all activity on stage axis 3 to stop
- 3WT3000: Wait for 3000 ms to accumulate data
- 2JL35: Jump to command 2DL, repeating 35 times before progressing out of loop

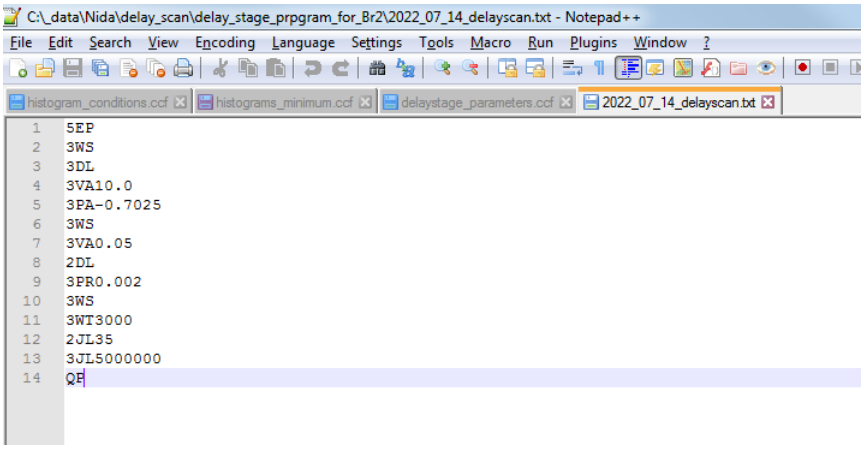

FIGURE C.5: An example delay stage code, written in the language of a Newport ESP300. This code aims to scan a small region to measure the temporal overlap between two pulses.

- 3JL5000000: Jump to command 3DL, repeating 5000000 times before progressing out of loop
- QP: End program

This particular example aims to scan a small region to measure the temporal overlap between two pulses. It starts at position -0.7025 mm, and moves forward in steps of 2 μm every 3 seconds. In total, it will travel 70 μm after 35 steps, before travelling back to -0.7025 mm to repeat the process.

The language to control the stage with the ESP300 is considerably more rich than demonstrated in this example. A manual which details all possible commands, use of the ESP300 in general, and other helpful advice can be found on the COLTRIMS computer in pdf form, entitled ESP300.pdf.

To communicate between the COLTRIMS computer and either the ESP300 or Labview, we use a program called Termie, which is shown in Figure C.6. Programs which have been written and saved in text files may be sent via the send file button, which saves them in the ESP300 memory. Individual commands may also be sent through this interface for any testing needed without the use of a program. Two generally useful commands for managing the programs in memory are # LP, which lists the program with ID #, and # XX, which deletes the program with ID #. Labview software controls the Micronix stage directly, but having Termie open is useful for testing the connection. It is important that the correct settings have been chosen in the Termie menu, otherwise communication between devices will not be possible

A special note about the memory of the ESP300: when you delete a program, it does not actually clear the memory that was used. Every few years, the total storage of the system will fill up, particularly if you are entering many delay codes often. When this

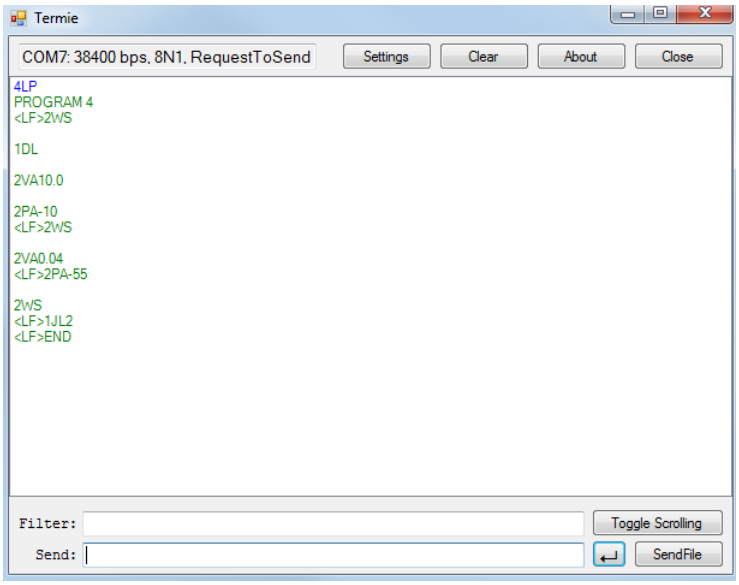

FIGURE C.6: Software to communicate directly with the Newport ESP300 or Labview called Termie. Commands to and from the stage are displayed in green text in the centre box. The SendFile button can be used to send program files.

happens, the controller will stop listening to commands altogether, seemingly for no reason. To fix this, simply input 0XX through Termie to clear all memory.

The C++ code which runs data acquisition also has a delay stage control in it, shown in Figure C.7. Line 52, sprintf(pollingcommand[ind]), "%dTP", 3); defines which axis of the ESP300 is getting read into the data acquisition, in this case set to axis # 3. It is vital to make sure that this number is changed to the appropriate axis, otherwise you will not read in the correct data, and it will be difficult to figure out why.

I conclude this appendix with a comment about the C++ code in general. It is absolutely worth familiarizing yourself with the overall flow of the program, however, as a beginner, it will be exceedingly difficult to make any meaningful changes to it yourself. Thankfully, it is not often necessary to do so, but it will happen on occasion, particularly with regard to the delay stage. If you are not experienced enough to solve the issue, Andre usually is, but even then, some problems still need to be escalated. The software was written by Achim Czasch, who works with Roentdek and can be contacted as a last resort.

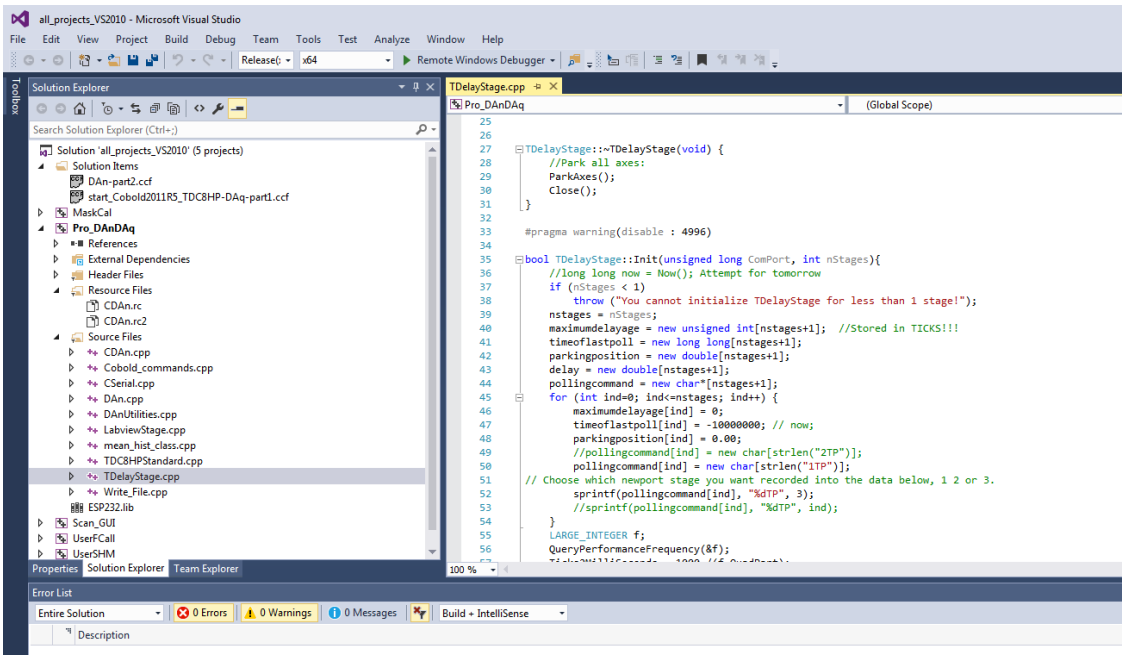

FIGURE C.7: C++ code that pertains to the delay stage. Line 52 chooses which axis is read out to the data acquisition, currently set to # 3.

Bibliography

[1]T Maiman, "Stimulated optical radiation in ruby", Nature **187**, 493–494 (1960).

[2]A. L. Schawlow and C. H. Townes, "Infrared and optical masers", Physical Review **112**, 1940–1949 (1958).

[3]J Meijer, K Du, A Gillner, D Hoffmann, V. S. Kovalenko, T Masuzawa, A Ostendorf, R Poprawe, and W Schulz, "Laser machining by short and ultrashort pulses, state of the art and new opportunities in the age of the photons", CIRP Annals **51**, 531–550 (2002).

[4]J Zweiback, R. A. Smith, T. E. Cowan, G Hays, K. B. Wharton, V. P. Yanovsky, and T Ditmire, "Nuclear fusion driven by coulomb explosions of large deuterium clusters", Physical Review Letters **84**, 2634–2637 (2000).

[5]N. Globus and R. D. Blandford, "The chiral puzzle of life", The Astrophysical Journal **895**, L11 (2020).

[6]E. Tokunaga, T. Yamamoto, E. Ito, and N. Shibata, "Understanding the thalidomide chirality in biological processes by the self-disproportionation of enantiomers", Scientific Reports **8**, 10.1038/s41598-018-35457-6 (2018).

[7]*Https://en.wikipedia.org/wiki/thalidomide*, 2022.

[8]E. J. Ariens and E. W. Wuis, "Chiral cognisance: a road to safer and more effective medicinal products", Journal of the Royal College of Physicians of London **28**, 395–398 (1994).

[9]P Agostini, F Fabre, G Mainfray, G Petite, and N. K. Rahman, "Free-free transitions following six-photon ionization of xenon atoms", Physical Review Letters **42**, 1127–1130 (1977).

[10]D. B. Milošević, G. G. Paulus, D. Bauer, and W. Becker, "Above-threshold ionization by few-cycle pulses", Journal of Physics B: Atomic, Molecular and Optical Physics **39**, 10.1088/0953-4075/39/14/R01 (2006).

[11]L. V. Keldysh, "Ionization in the field of a strong electromagnetic wave", J. Exptl. Theoret. Phys. **20**, 1945–1957 (1965).

[12]M. Y. Ivanov, M. Spanner, and O. Smirnova, "Anatomy of strong field ionization", Journal of Modern Optics **52**, 165–184 (2005).

[13]M. V. Ammosov, N. B. Delone, and V. P. Krainov, "Tunnel ionization of complex atoms and of atomic ions in an alternating electromagnetic field", Soviet Phys JETP **64**, 1191–1194 (1986).

[14]N. B. Delone and V. P. Krainov, "Tunneling and barrier-suppression ionization of atoms and ions in a laser radiation field", Physics - Uspekhi **41**, 469–485 (1998).

[15]X. M. Tong, Z. X. Zhao, and C. D. Lin, "Theory of molecular tunneling ionization", Physical Review A **66**, 11 (2002).

[16]Z. X. Zhao, X. M. Tong, and C. D. Lin, "Alignment-dependent ionization probability of molecules in a double-pulse laser field", Physical Review A - Atomic, Molecular, and Optical Physics **67**, 5 (2003).

[17]D. Pavičić, K. F. Lee, D. M. Rayner, P. B. Corkum, and D. M. Villeneuve, "Direct measurement of the angular dependence of ionization for n 2, o2, and co2 in intense laser fields", Physical Review Letters **98**, 10.1103/PhysRevLett.98.243001 (2007).

[18]T. Brabec, M. Côté, P. Boulanger, and L. Ramunno, "Theory of tunnel ionization in complex systems", Physical Review Letters **95**, 10.1103/PhysRevLett.95.073001 (2005).

[19]A. Emmanouilidou, "Recoil collisions as a portal to field-assisted ionization at near-uv frequencies in the strong-field double ionization of helium", Physical Review A - Atomic, Molecular, and Optical Physics **78**, 10.1103/PhysRevA.78.023411 (2008).

[20]M Meckel, D Comtois, D Zeidler, A Staudte, D Pavičić, H. C. Bandulet, H Pépin, J. C. Kieffer, R Dörner, D. M. Villeneuve, and P. B. Corkum, "Laser-induced electron tunneling and diffraction", Science **320**, 1478–1482 (2008).

[21]M. Meckel, A. Staudte, S. Patchkovskii, D. M. Villeneuve, P. B. Corkum, R. Dörner, and M. Spanner, "Signatures of the continuum electron phase in molecular strong-field photoelectron holography", Nature Physics **10**, 594–600 (2014).

[22]Y Huismans, A Rouzée, A Gijsbertsen, J. H. Jungmann, A. S. Smolkowska, P. S. W. M. Logman, F Lépine, C Cauchy, Z. S, T Marchenko, J. M. Bakker, G Berden, B Redlich, A. F. G. van der Meer, H. G. Muller, W Vermin, K. J. Schafer, M Spanner, M. Y. Ivanov, O Smirnova, D Bauer, S. V. Popruzhenko, and M. J. J. Vrakking, "Time-resolved holography with photoelectrons", Science **331**, 61–64 (2011).

[23]A Maxwell and C. F. de Morisson Faria, "Strong-field interference of quantum trajectories with coulomb distortion and electron correlation" (University College London, 2018).

[24]A. C. Bray, C. F. de Morisson Faria, and S. Yurchenko, "Electron rescattering picture in a strong-field laser regime: diverse initial state geometry under coulomb influences" (University College London, 2022).

[25]A L'Huillier, L. A. Lompre, G Mainfray, and C Manus, "Multiply charged ions formed by multiphoton absorption processes in the continuum", Physical Review Letters **48**, 1814–1818 (1982).

[26]S Larochelle, A Talebpour, and S. L. Chin, "Non-sequential multiple ionization of rare gas atoms in a ti:sapphire laser field", J. Phys. B: At. Mol. Opt. Phys **31**, 1201–1214 (1998).

[27]T. Weber, H Glessen, M Weckenbrock, G Urbasch, A Staudte, L Spielberger, O Jagutzld, V Mergel, M Vollmer, and R Dörner, "Correlated electron emission in multiphoton double ionization", Nature **405**, 658–661 (2000).

[28]M Kübel and M Kling, "Single-cycle non-sequential double ionization" (Ludwig Maximilian University of Munich, 2014).

[29]B. Bergues, M. Kubel, N. G. Kling, C. Burger, and M. F. Kling, "Single-cycle nonsequential double ionization", IEEE Journal on Selected Topics in Quantum Electronics **21**, 10.1109/JSTQE.2015.2443976 (2015).

[30]Z. Chang, *Fundamentals of attosecond optics* (CRC Press, 2016).

[31]M. Sabbar, S. Heuser, R. Boge, M. Lucchini, L. Gallmann, C. Cirelli, and U. Keller, "Combining attosecond xuv pulses with coincidence spectroscopy", Review of Scientific Instruments **85**, 10.1063/1.4898017 (2014).

[32]S. J. Weber, B. Manschwetus, M. Billon, M. Böttcher, M. Bougeard, P. Breger, M. Géléoc, V. Gruson, A. Huetz, N. Lin, Y. J. Picard, T. Ruchon, P. Salières, and B. Carré, "Flexible attosecond beamline for high harmonic spectroscopy and xuv/near-ir pump probe experiments requiring long acquisition times", Review of Scientific Instruments **86**, 10.1063/1.4914464 (2015).

[33]L. Cattaneo, J. Vos, R. Y. Bello, A. Palacios, S. Heuser, L. Pedrelli, M. Lucchini, C. Cirelli, F. Martín, and U. Keller, "Attosecond coupled electron and nuclear dynamics in dissociative ionization of h 2", Nature Physics **14**, 733–739 (2018).

[34]J Krause, K Schafer, and K Kulander, "High-order harmonic generation from atoms and ions in the high intensity regime", Physical Review Letters **68**, 24–28 (1992).

[35]P. B. Corkum, "Plasma perspective on strong-field multiphoton ionization", Physical Review Letters **71** (1993).

[36]N. Dudovich, O. Smirnova, J. Levesque, Y. Mairesse, M. Y. Ivanov, D. M. Villeneuve, and P. B. Corkum, "Measuring and controlling the birth of attosecond xuv pulses", Nature Physics **2**, 781–786 (2006).

[37]Y. J. Chen, L. B. Fu, and J. Liu, "Asymmetric molecular imaging through decoding odd-even high-order harmonics", Physical Review Letters **111**, 10.1103/PhysRevLett.111.073902 (2013).

[38]G. Vampa, T. J. Hammond, N. Thiré, B. E. Schmidt, F. Légaré, C. R. McDonald, T. Brabec, and P. B. Corkum, "Linking high harmonics from gases and solids", Nature **522**, 462–464 (2015).

[39]J Itatani, J Levesque, D Zeidler, H. Niikura, H. P. Pin, J. C. Kieffer, P. B. Corkum, and. D. M. Villeneuve, "Tomographic imaging of molecular orbitals", Nature **432**, 867–871 (2004).

[40]P. Peng, C. Marceau, and D. M. Villeneuve, "Attosecond imaging of molecules using high harmonic spectroscopy", Nature Reviews Physics **1**, 144–155 (2019).

[41]M. Kübel, M. Spanner, Z. Dube, A. Y. Naumov, S. Chelkowski, A. D. Bandrauk, M. J. Vrakking, P. B. Corkum, D. M. Villeneuve, and A. Staudte, "Probing multiphoton light-induced molecular potentials", Nature Communications **11**, 10.1038/s41467-020-16422-2 (2020).

[42]Y. Mi, P. Peng, N. Camus, X. Sun, P. Fross, D. Martinez, Z. Dube, P. B. Corkum, D. M. Villeneuve, A. Staudte, R. Moshammer, and T. Pfeifer, "Clocking enhanced ionization of hydrogen molecules with rotational wave packets", Physical Review Letters **125**, 10.1103/PhysRevLett.125.173201 (2020).

[43]H. Ibrahim, C. Lefebvre, A. D. Bandrauk, A. Staudte, and F. Légaré, "H2: the benchmark molecule for ultrafast science and technologies", Journal of Physics B **51**, 10.1088/1361-6455/aaa192 (2018).

[44]A. S. Alnaser, X. M. Tong, T. Osipov, S. Voss, C. M. Maharjan, B. Shan, Z. Chang, and C. L. Cocke, "Laser-peak-intensity calibration using recoil-ion momentum imaging", Physical Review A **70**, 10.1103/PhysRevA.70.023413 (2004).

[45]A Zariyev, P. H. Bucksbaum, H. G. Muller, and D. W. Schumacher, "Ionization and dissociation of h2 in intense laser fields at 1.064 um, 532 nm, and 355 nm", Physical Review A **42**, 5500–5514 (1990).

[46]S. I. Chu and D. A. Telnov, *Beyond the floquet theorem: generalized floquet formalisms and quasienergy methods for atomic and molecular multiphoton processes in intense laser fields* (2004), pp. 1–131.

[47]N. Moiseyev, *Quantum theory of resonances: calculating energies, widths and cross-sections by complex scaling* (1998), pp. 211–293.

[48]A Giusti-Suzor and F. H. Mies, "Vibrational trapping and suppression of dissociation in intense laser fields", Physical Review Letters **68**, 26 (1992).

[49]A Giusti-Suzor, X He, and F. H. Mies, "Above-threshold dissociation of h2+ in intense laser fields", Physical Review Letters **64**, 515–518 (1990).

[50]P. H. Bucksbaum, A Zavriyev, H. G. Muller, and D. W. Schumacher, "Softening of the h2+ molecular bond in intense laser fields", Physical Review Letters **64**, 1883–1886 (1990).

[51]P. Lu, J. Wang, H. Li, K. Lin, X. Gong, Q. Song, Q. Ji, W. Zhang, J. Ma, H. Li, H. Zeng, F. He, and J. Wu, "High-order above-threshold dissociation of molecules", Proceedings of the National Academy of Sciences of the United States of America **115**, 2049–2053 (2018).

[52]T. Seideman, M. Y. Ivanov, and P. B. Corkum, "Role of electron localization in intense-field molecular ionization", Physical Review Letters **75**, 2819–2822 (1995).

[53]T Zuo and A. D. Bandrauk, "Charge-resonance-enhanced ionization of diatomic molecular ions by intense lasers", Physical Review A **52** (1995).

[54]S Chelkowski, P. B. Corkum, and A. D. Bandrauk, "Femtosecond coulomb explosion imaging of vibrational wave functions", Physical Review Letters **82**, 3416–3419 (1999).

[55]F. Légaré, K. F. Lee, I. V. Litvinyuk, P. W. Dooley, A. D. Bandrauk, D. M. Villeneuve, and P. B. Corkum, "Imaging the time-dependent structure of a molecule as it undergoes dynamics", Physical Review A **72**, 10.1103/PhysRevA.72.052717 (2005).

[56]H. D. Flack and G. Bernardinelli, "The use of x-ray crystallography to determine absolute configuration", Chirality **20**, 681–690 (2008).

[57]M. Pitzer, M. Kunitski, A. S. Johnson, T. Jahnke, H. Sann, F. Sturm, L. H. P. Schmidt, H. Schmidt-Böcking, R. Dörner, J. Stohner, J. Kiedrowski, M. Reggelin, S. Marquardt, A. Schießer, R. Berger, and M. S. Schöffler, "Direct determination of absolute molecular stereochemistry in gas phase by coulomb explosion imaging", Science **341**, 1096–1100 (2013).

[58]B. Ritchie, "Theory of the angular distribution of photoelectrons ejected from optically active molecules and molecular negative ions*", Physical Review A **13**, 1411–1415 (1976).

[59]I. Powis, "Photoelectron circular dichroism of the randomly oriented chiral molecules glyceraldehyde and lactic acid", Journal of Chemical Physics **112**, 301–310 (2000).

[60]N. Böwering, T. Lischke, B. Schmidtke, N. Müller, T. Khalil, and U. Heinzmann, "Asymmetry in photoelectron emission from chiral molecules induced by circularly polarized light", Physical Review Letters **86**, 1187–1190 (2001).

[61]K. Fehre, N. M. Novikovskiy, S. Grundmann, G. Kastirke, S. Eckart, F. Trinter, J. Rist, A. Hartung, D. Trabert, C. Janke, G. Nalin, M. Pitzer, S. Zeller, F. Wiegandt, M. Weller, M. Kircher, M. Hofmann, L. P. H. Schmidt, A. Knie, A. Hans, L. B. Ltaief, A. Ehresmann, R. Berger, H. Fukuzawa, K. Ueda, H. Schmidt-Böcking, J. B. Williams, T. Jahnke, R.

Dörner, M. S. Schöffler, and P. V. Demekhin, "Fourfold differential photoelectron circular dichroism", Physical Review Letters **127**, 10.1103/PhysRevLett.127.103201 (2021).

[62]M. Tia, M. Pitzer, G. Kastirke, J. Gatzke, H.-K. Kim, F. Trinter, J. Rist, A. Hartung, D. Trabert, J. Siebert, K. Henrichs, J. Becht, S. Zeller, H. Gassert, F. Wiegandt, R. Wallauer, A. Kuhlins, C. Schober, T. Bauer, N. Wechselberger, P. Burzynski, J. Neff, M. Weller, D. Metz, M. Kircher, M. Waitz, J. B. Williams, L. Schmidt, A. D. Mueller, A. Knie, A. Hans, L. B. Ltaief, A. Ehresmann, R. Berger, H. Fukuzawa, K. Ueda, H. Schmidt-Boecking, R. Doerner, T. Jahnke, P. V. Demekhin, and M. Schoeffler, "Observation of enhanced chiral asymmetries in the inner-shell photoionization of uniaxially oriented methyloxirane enantiomers", J Chem Phys Lett **8**, 2780–2786 (2017).

[63]S. Turchini, N. Zema, G. Contini, G. Alberti, M. Alagia, S. Stranges, G. Fronzoni, M. Stener, P. Decleva, and T. Prosperi, "Circular dichroism in photoelectron spectroscopy of free chiral molecules: experiment and theory on methyl-oxirane", Physical Review A - Atomic, Molecular, and Optical Physics **70**, 10.1103/PhysRevA.70.014502 (2004).

[64]S. Stranges, S. Turchini, M. Alagia, G. Alberti, G. Contini, P. Decleva, G. Fronzoni, M. Stener, N. Zema, and T. Prosperi, "Valence photoionization dynamics in circular dichroism of chiral free molecules: the methyl-oxirane", Journal of Chemical Physics **122**, 10.1063/1.1940632 (2005).

[65]S. Turchini, D. Catone, G. Contini, N. Zema, S. Irrera, M. Stener, D. D. Tommaso, P. Decleva, and T. Prosperi, "Conformational effects in photoelectron circular dichroism of alaninol", ChemPhysChem **10**, 1839–1846 (2009).

[66]L. Nahon, G. A. Garcia, and I. Powis, "Valence shell one-photon photoelectron circular dichroism in chiral systems", Journal of Electron Spectroscopy and Related Phenomena **204**, 322–334 (2015).

[67]J. R. Rouxel, M. Kowalewski, and S. Mukamel, "Photoinduced molecular chirality probed by ultrafast resonant x-ray spectroscopy", Structural Dynamics **4**, 10.1063/1.4974260 (2017).

[68]Y. Zhang, J. R. Rouxel, J. Autschbach, N. Govind, and S. Mukamel, "X-ray circular dichroism signals: a unique probe of local molecular chirality", Chemical Science **8**, 5969–5978 (2017).

[69]J. R. Rouxel, Y. Zhang, and S. Mukamel, "X-ray raman optical activity of chiral molecules", Chemical Science **10**, 898–908 (2019).

[70]C. S. Lehmann, N. B. Ram, I. Powis, and M. H. Janssen, "Imaging photoelectron circular dichroism of chiral molecules by femtosecond multiphoton coincidence detection", Journal of Chemical Physics **139**, 10.1063/1.4844295 (2013).

[71]S. Rozen, A. Comby, E. Bloch, S. Beauvarlet, D. Descamps, B. Fabre, S. Petit, V. Blanchet, B. Pons, N. Dudovich, and Y. Mairesse, "Controlling subcycle optical chirality in the photoionization of chiral molecules", Physical Review X **9**, 10.1103/PhysRevX.9.031004 (2019).

[72]M. H. Janssen and I. Powis, "Detecting chirality in molecules by imaging photoelectron circular dichroism", Physical Chemistry Chemical Physics **16**, 856–871 (2014).

[73]M. M. Fanood, N. B. Ram, C. S. Lehmann, I. Powis, and M. H. Janssen, "Enantiomer-specific analysis of multi-component mixtures by correlated electron imaging-ion mass spectrometry", Nature Communications **6**, 10.1038/ncomms8511 (2015).

[74]C. Lux, M. Wollenhaupt, C. Sarpe, and T. Baumert, "Photoelectron circular dichroism of bicyclic ketones from multiphoton ionization with femtosecond laser pulses", ChemPhysChem **16**, 115–137 (2015).

[75]S. Beaulieu, A. Comby, B. Fabre, D. Descamps, A. Ferré, G. Garcia, R. Géneaux, F. Légaré, L. Nahon, S. Petit, T. Ruchon, B. Pons, V. Blanchet, and Y. Mairesse, "Probing ultrafast dynamics of chiral molecules using time-resolved photoelectron circular dichroism", in , Vol. 194 (2016), pp. 325–348.

[76]A. Comby, S. Beaulieu, M. Boggio-Pasqua, D. Descamps, F. Légaré, L. Nahon, S. Petit, B. Pons, B. Fabre, Y. Mairesse, and V. Blanchet, "Relaxation dynamics in photoexcited chiral molecules studied by time-resolved photoelectron circular dichroism: toward chiral femtochemistry", Journal of Physical Chemistry Letters **7**, 4514–4519 (2016).

[77]A. Kastner, C. Lux, T. Ring, S. Züllighoven, C. Sarpe, A. Senftleben, and T. Baumert, "Enantiomeric excess sensitivity to below one percent by using femtosecond photoelectron circular dichroism", ChemPhysChem **17**, 1119–1122 (2016).

[78]J. Miles, D. Fernandes, A. Young, C. M. Bond, S. W. Crane, O. Ghafur, D. Townsend, J. Sá, and J. B. Greenwood, "A new technique for probing chirality via photoelectron circular dichroism", Analytica Chimica Acta **984**, 134–139 (2017).

[79]S. Beaulieu, A. Comby, D. Descamps, B. Fabre, G. A. Garcia, R. Géneaux, A. G. Harvey, F. Légaré, Z. Mašín, L. Nahon, A. F. Ordonez, S. Petit, B. Pons, Y. Mairesse, O. Smirnova, and V. Blanchet, "Photoexcitation circular dichroism in chiral molecules", Nature Physics **14**, 484–489 (2018).

[80]J. R. Rouxel, A. Rajabi, and S. Mukamel, "Chiral four-wave-mixing signals with circularly-polarized x-ray pulses", (2020).

[81]R. Cireasa, A. E. Boguslavskiy, B. Pons, M. C. Wong, D. Descamps, S. Petit, H. Ruf, N. Thiré, A. Ferré, J. Suarez, J. Higuet, B. E. Schmidt, A. F. Alharbi, F. Légaré, V. Blanchet, B. Fabre, S. Patchkovskii, O. Smirnova, Y. Mairesse, and V. R. Bhardwaj, "Probing molecular chirality on a sub-femtosecond timescale", Nature Physics **11**, 654–658 (2015).

[82]Y. Harada, E. Haraguchi, K. Kaneshima, and T. Sekikawa, "Circular dichroism in high-order harmonic generation from chiral molecules", Physical Review A **98**, 10.1103/PhysRevA.98.021401 (2018).

[83]A. Fleischer, O. Kfir, T. Diskin, P. Sidorenko, and O. Cohen, "Spin angular momentum and tunable polarization in high-harmonic generation", Nature Photonics **8**, 543–549 (2014).

[84]A. Ferré, C. Handschin, M. Dumergue, F. Burgy, A. Comby, D. Descamps, B. Fabre, G. A. Garcia, R. Géneaux, L. Merceron, E. Mével, L. Nahon, S. Petit, B. Pons, D. Staedter, S. Weber, T. Ruchon, V. Blanchet, and Y. Mairesse, "A table-top ultrashort light source in the extreme ultraviolet for circular dichroism experiments", Nature Photonics **9**, 93–98 (2015).

[85]D. Baykusheva and H. J. Wörner, "Chiral discrimination through bielliptical high-harmonic spectroscopy", Physical Review X **8**, 10.1103/PhysRevX.8.031060 (2018).

[86]D. Baykusheva, D. Zindel, V. Svoboda, E. Bommeli, M. Ochsner, A. Tehlar, and H. J. Wörner, "Real-time probing of chirality during a chemical reaction", Proceedings of the National Academy of Sciences of the United States of America **116**, 23923–23929 (2019).

[87]D. Ayuso, O. Neufeld, A. F. Ordonez, P. Decleva, G. Lerner, O. Cohen, M. Ivanov, and O. Smirnova, "Synthetic chiral light for efficient control of chiral light–matter interaction", Nature Photonics **13**, 866–871 (2019).

[88]D. Ayuso, A. Ordonez, M. Ivanov, and O. Smirnova, "Ultrafast optical rotation in chiral molecules with ultrashort and tightly focused beams", Optica **8**, 1243–1246 (2021).

[89]D. Ayuso, A. F. Ordonez, P. Decleva, M. Ivanov, and O. Smirnova, "Enantio-sensitive unidirectional light bending", Nature Communications **12**, 10.1038/s41467-021-24118-4 (2021).

[90]M. Kübel, Z. Dube, A. Y. Naumov, M. Spanner, G. G. Paulus, M. F. Kling, D. M. Villeneuve, P. B. Corkum, and A. Staudte, "Streak camera for strong-field ionization", Physical Review Letters **119**, 10.1103/PhysRevLett.119.183201 (2017).

[91]G Tejeda, J. M. Fernández-Sánchez, and S Montero, "Temperature and density mapping of supersonic jet expansions using linear raman spectroscopy", Physical Review Letters **76**, 34–37 (1996).

[92]J. Itatani, F. Quéré, G. L. Yudin, M. Y. Ivanov, F. Krausz, and P. B. Corkum, "Attosecond streak camera", Physical Review Letters **88**, 4 (2002).

[93]G. P. Katsoulis, Z. Dube, P. Corkum, A. Staudte, and A. Emmanouilidou, "Momentum scalar triple product as a measure of chirality in electron ionization dynamics of strongly-driven atoms", arXiv (2021).

[94]C. T. Smeenk, L. Arissian, B. Zhou, A. Mysyrowicz, D. M. Villeneuve, A. Staudte, and P. B. Corkum, "Partitioning of the linear photon momentum in multiphoton ionization", Physical Review Letters **106**, 10.1103/PhysRevLett.106.193002 (2011).

[95]F Mousavi, *Measuring ultrashort laser pulses using transient grating frequency-resolved optical gating* (2022).

[96]E. Goulielmakis, Z. H. Loh, A. Wirth, R. Santra, N. Rohringer, V. S. Yakovlev, S. Zherebtsov, T. Pfeifer, A. M. Azzeer, M. F. Kling, S. R. Leone, and F. Krausz, "Real-time observation of valence electron motion", Nature **466**, 739–743 (2010).

[97]M. Kübel, Z. Dube, A. Y. Naumov, D. M. Villeneuve, P. B. Corkum, and A. Staudte, "Spatiotemporal imaging of valence electron motion", Nature Communications **10**, 10.1038/s41467-019-09036-w (2019).